

Ionospheric Disturbances:
Midlatitude Pi2 Magnetospheric ULF Pulsations
and Medium Scale Traveling Ionospheric Disturbances

Nathaniel Anthony Frissell

Dissertation submitted to the Faculty of the
Virginia Polytechnic Institute and State University
in partial fulfillment of the requirements for the degree of

Doctor of Philosophy
in
Electrical Engineering

J. Michael Ruohoniemi, Co-Chair
Joseph B. H. Baker, Co-Chair
Gregory D. Earle
C. Robert Clauer
Timothy Pratt
Werner E. Kohler
David G. Sibeck

April 25, 2016
Blacksburg, Virginia

Keywords: Pi2 ULF Pulsations, Atmospheric Gravity Waves, MSTIDs, Ionosphere,
Magnetosphere

Copyright 2016, Nathaniel Anthony Frissell

Ionospheric Disturbances: Midlatitude Pi2 Magnetospheric ULF Pulsations and Medium Scale Traveling Ionospheric Disturbances

Nathaniel Anthony Frissell

Abstract

The ionosphere is an electrically charged atmospheric region which is coupled to the sun, the magnetosphere, and the neutral atmosphere. The ionospheric state can significantly impact technological systems, especially those which utilize radio frequency energy. By studying ionospheric disturbances, it is possible to gain a deeper understanding of not only the ionosphere itself, but also the natural and technological systems it is coupled to. This dissertation research utilizes high frequency (HF) radio remote sensing techniques to study three distinct types of ionospheric disturbances. First, ground magnetometers and a new mid latitude SuperDARN HF radar at Blackstone, Virginia are used to observe magnetospheric Pi2 ultra low frequency (ULF) pulsations in the vicinity of the plasmopause. Prior to these pulsations, two Earthward moving fast plasma flows were detected by spacecraft in the magnetotail. Signatures of inner magnetospheric compression observed by the Blackstone radar provide conclusive evidence that the plasma flow bursts directly generated the ground Pi2 signature via a compressional wave. This mechanism had previously been hypothesized, but never confirmed. Next, ten SuperDARN radars in the North American Sector are used to investigate the sources and characteristics of atmospheric gravity waves (AGW) associated medium scale traveling ionospheric disturbances (MSTIDs) at both midlatitudes and high latitudes. Consistent with prior studies, the climatological MSTID population in both latitudinal regions was found to peak in the fall and winter and have a dominant equatorward propagation direction. Prior studies suggested these MSTIDs were caused by mechanisms associated with auroral and space weather activity; however, it is shown here that the AE and Sym-H indices are poorly correlated with MSTID observations. A new, multi-week timescale of MSTID activity is reported. This leads to the finding that MSTID occurrence is highly correlated with an index representative of polar vortex activity, possibly controlled by a filtering mechanism that is a function of stratospheric neutral wind direction. Finally, a case study of a radio blackout of transionospheric HF communications caused by an X2.9 class solar flare is presented. This study demonstrates the potential of a novel technique employing signals of opportunity and automated receiving networks voluntarily created by an international community of amateur radio operators.

Ionospheric Disturbances: Midlatitude Pi2 Magnetospheric ULF Pulsations and Medium Scale Traveling Ionospheric Disturbances

Nathaniel Anthony Frissell

General Audience Abstract

The ionosphere is an electrically charged part of the atmosphere that is coupled to the Sun, the Earth's magnetosphere, and the neutral atmosphere. This dissertation research utilizes high frequency (HF) radio remote sensing techniques to study three distinct types of ionospheric disturbances. First, ground magnetometers and a high frequency SuperDARN radar at Blackstone, Virginia are used to observe pulsations in the ionosphere associated with a brightening of the aurora. Prior to the ground observations of these pulsations, spacecraft observed two fast plasma flows in the magnetotail moving toward Earth. Observations by the Blackstone radar provided evidence that the plasma flow bursts generated the ionospheric pulsations by compressing the inner magnetosphere. Next, SuperDARN radars spread across North America are used to investigate the sources and characteristics of wave-like ionospheric disturbances known as medium scale traveling ionospheric disturbances (MSTIDs). Consistent with prior studies, MSTID activity was found to peak in the fall and winter and have a dominant pole-to-equator direction of travel. Prior studies suggested these MSTIDs were caused by mechanisms associated with auroral and space weather activity; however, it is found that polar vortex dynamics are instead responsible for most observed MSTID activity. Finally, a case study of a radio blackout of HF communications caused by an X-class solar flare is presented. This study is intended to demonstrate the potential of using observations of amateur radio signals for the purpose of remote sensing the ionosphere.

Dedication

To my mother, Ann Marie, my father, Richard, and my sister, Elaina.

Acknowledgments

To Mike and Jo, my advisors, who have supported me and given valuable advice even when the work was challenging. You have provided me with amazing opportunities during my time in graduate school, while giving me the freedom to pursue my interests.

To Bob C., who introduced me to Space Science. You have always been supportive. To Ray, whose passion for research is inspiring. To my committee members, especially Greg, who always has been willing to listen and provide good ideas for moving forward.

To Kjellmar and my friends from Svalbard, who let me see the aurora with my own eyes and experience the adventure of a lifetime. To Bill, Jef, Kevin, Ethan, and Simon, with whom I have spent many happy weeks on cold, wet, windy, remote, and forsaken islands.

To all of my fellow students and post-docs, including Kevin, AJ, Sebastien, Bharat, Evan, Lasse, Kshitija, Hyomin, Pratik, Garima, Muhammad, Xueling, Dong, Shibaji, Srimoyee, Magda, and Carson. I have shared the process of learning and discovery with each of you. To my friends in the GEM and CEDAR communities, especially Steve, Jenni, Christine, Rick, Jone, Betsey, and Robert. You have always helped make meetings joyful occasions.

To my teachers and scouting friends, who always worked to point me in the right direction. To all of my friends from the many clubs and organizations I have been a part of, including the Virginia Tech Amateur Radio Association, the Newman Catholic Community and Musicians, the Outdoor Club, and the Triathlon Club. Especially Andrew K., Joe C., Rob, Dan, John D., Andy, Shyam, Sheghou, Kay and Carter, Ben and Cathy, Bob and Patrice, Bob M., Sergio, and Erika. Each of you have given me a larger perspective on the world and life.

To Mary Lou, who introduced me to research and has been a constant supporter. To my friends from home, especially Joe P., Gus, Mel, and Jessica. To Andy, Kevin, Dhvanit, Cheryl, Michelle, Lou, Jacob, Tom, and those at the New Jersey Institute of Technology. You have not only provided a friendly work environment during my time at home, but also key ideas for my graduate work and the opportunity to continue pursuing my career.

To my mother, Ann Marie, and my sister, Elaina. Your unending encouragement and love have allowed me to bring this dissertation to completion. To my father, Richard, who never knew that I would study at VT. You have always showed an incredible love and taught me lessons that I will carry with me for the rest of my life. To God, who has given me the opportunity to do this work and try to make the world a better place.

Contents

1	Introduction	1
1.1	Introduction	1
1.2	The Solar-Terrestrial Environment	2
1.2.1	Solar Wind and Interplanetary Magnetic Field	3
1.2.2	The Magnetosphere	3
1.2.3	The Ionosphere	5
1.2.4	The Neutral Atmosphere	6
1.3	Ionospheric Remote Sensing Techniques	7
1.3.1	SuperDARN	7
1.3.2	Amateur Radio Networks	11
1.4	Ionospheric Perturbations	12
1.4.1	Magnetospheric Pi2 ULF Pulsations	12
1.4.2	Medium Scale Traveling Ionospheric Disturbances	17
1.4.3	Ionospheric Impacts of Solar Flares	23
1.5	Research Questions and Objectives	24
2	First Radar Observations in the Vicinity of the Plasmapause of Pulsed Ionospheric Flows Generated by Bursty Bulk Flows	45
2.1	Introduction	47
2.2	Observations	48

2.3	Discussion	51
2.4	Conclusions	53
2.5	Acknowledgments	54
3	Climatology of Medium Scale Traveling Ionospheric Disturbances Observed by the Midlatitude Blackstone SuperDARN Radar	58
3.1	Introduction	60
3.2	Instrumentation	62
3.2.1	SuperDARN	62
3.3	Observations	64
3.3.1	Event Study: 19 November 2010, 1200-2000 UT	64
3.3.2	Statistical Study	71
3.4	Summary and Conclusions	81
3.5	Acknowledgments	82
4	Sources and Characteristics of Medium Scale Traveling Ionospheric Disturbances Observed by High Frequency Radars in the North American Sector	100
4.1	Introduction	102
4.2	Datasets and Methodology	104
4.2.1	SuperDARN	104
4.2.2	MSTID Index	107
4.2.3	Space Weather Indices	107
4.2.4	Neutral Atmospheric Data	108
4.3	Results	109
4.3.1	MSTID Climatology	110
4.3.2	Time Series of MSTIDs and Candidate Drivers	111
4.3.3	Probability and Correlation Analysis	114
4.3.4	Comparison with the Lower and Middle Atmosphere	115
4.4	Discussion	117

4.5	Summary and Conclusions	120
4.6	Acknowledgments	120
5	Ionospheric Sounding Using Real-Time Amateur Radio Reporting Networks	139
5.1	Introduction	141
5.2	Amateur Radio Reporting Network Architecture	142
5.3	Case Study: Ionospheric Impacts of the 13 May 2013 Solar Flare	144
5.4	Discussion	145
5.5	Summary	147
5.6	Acknowledgments	147
6	Summary and Future Work	153
6.1	Summary	153
6.2	Future Work	158
	Bibliography	161

List of Figures

1.1	Artistic cartoon depicting the solar wind and the Earth’s magnetosphere. Image credit: NASA.	27
1.2	Spectral radiance of the surface of the Sun as a function of wavelength. From <i>Priest</i> [1995], used with permission.	28
1.3	A depiction of the magnetosphere illustrating key magnetospheric processes and features. See Sections 1.2.2 for details.	29
1.4	Daytime international quiet solar year (IQSY) ionospheric and atmospheric composition measurements based on mass spectrometer data. From <i>Luhmann</i> [1995] after <i>Johnson</i> [1969], used with permission.	30
1.5	Example neutral atmospheric temperature profile generated using the MSIS model for 21 Jan 2013 1200 UT, 40°N, 80°W. Atmospheric regions are defined by the inflection points of the temperature profile.	31
1.6	SuperDARN Network in March 2016.	32
1.7	SuperDARN radar at McMurdo Station, Antarctica. The main linear phased array (16 antennas) is on the left, and the receive-only interferometer array (4 antennas) is on the right. A corner reflector attached to the back of each array directs radar energy in the desired direction. Photo: N. A. Frissell . . .	33
1.8	Illustration of coherent (Bragg) scattering of radar signals from ionospheric field aligned irregularities.	34
1.9	Raytrace of Blackstone SuperDARN radar at 10 MHz (bottom) and 15 MHz (top) using a procedure developed by <i>de Larquier et al.</i> [2013]. The gray curves represent radars rays, the background colors indicate IRI model electron densities [<i>Bilitza et al.</i> , 2011], the dashed purple lines show magnetic field inclination, and the thick black curve shows where the radar rays are orthogonal to the magnetic field within 1°.	35

1.10	Scan plot of SNR/Power measurements made by the Blackstone, Virginia SuperDARN radar on 16 November 2015, 1600–1601 UT at 14.5 MHz. Beam 15 is shaded in gray. Wavefronts indicative of MSTIDs are visible in the ground scatter band.	36
1.11	Range-Time-Intensity (RTI) plot of Doppler velocity and SNR measurements collected by the Blackstone, Virginia SuperDARN radar on 16 November 2015. Gray shading indicates measurements identified as ground scatter.	37
1.12	Example high frequency (HF) amateur radio station. Photo: N. A. Frissell .	38
1.13	High frequency amateur radio communications links observed by the Reverse Beacon Network from 1505–1520 UT on 13 May 2013. From <i>Frissell et al.</i> [2014a], used with permission.	39
1.14	Illustration of the substorm current wedge formed from a diversion of the cross-tail current. From <i>McPherron et al.</i> [1973], used with permission. . . .	40
1.15	The magnetosphere at the onset of substorm expansion. Processes related to substorm current wedge formation (cross-tail current reduction) and the braking of bursty bulk flows against the nightside dipolar region are candidate energy sources for mid and low latitude Pi2 pulsations.	41
1.16	Four 1-minute scans of Blackstone SuperDARN power observations beginning at 1600 UT on 16 November 2015. Maps have successive 5 minute spacing. Beam 15 is shaded in gray. Wavefronts indicative of MSTIDs are visible in the ground scatter band and can be seen to move in range with time.	42
1.17	Raytrace of a SuperDARN radar operating at 14.5 MHz through the IRI perturbed with a model MSTID. The MSTID is modeled as a sinusoid with period $T = 40$ min and horizontal wavelength $\lambda_h = 450$ km. The top and bottom panels are separated by 20 minutes.	43
1.18	Schematic of nominal polar vortex configuration. Meridional temperature gradients and Coriolis effects create the high-speed flows in the jet. The jet can modulate atmospheric gravity waves propagating upward from below. From <i>Gerrard et al.</i> [2002], used with permission.	44
2.1	AACGM map for the substorm on 22 February 2008 at 0436 UT. The map includes LOS BKS velocity data at 0444-0446 UT (green-red-blue colors), POES auroral precipitation flux at 0430-0530 UT (blue colors), locations of GBOs (brown asterisks), footprints of two THEMIS probes (letters D and E), estimates of the auroral oval (gray circles), westward electrojet (pink color), SCW FACs (encircled dots), and plasmopause (between blue dashed lines). .	55

2.2	Time series data for a substorm on 22 February 2008. (a) BKS radar LOS velocity data from beam 8 with 2 min resolution. (b) BKS beam 7 shows Pi2s that cannot be observed in beam 8. (c) LOS velocity data from BKS beam 7, range gate 21. (d) RMUS GMAG component rotated into the LOS direction of the radar, baseline removed. (e) 3-component RMUS data, baseline removed. (f) Ion velocity data from THM-D and E.	56
2.3	(a) 3 range gate averages of BKS beam 7 LOS velocity data. (b) Same as (a), but average subtracted. During intervals marked as coherences, the velocity traces from all latitudes move together as energy from BBF braking pushes on the field lines. During intervals marked as dispersions, field lines move back toward their original state.	57
3.1	Ground scatter power data and FOVs from the BKS and GBR radars showing MSTIDs during a one minute scan starting on 19 November 2010 at 1440 UT: (a) standard slant range mapping; (b) ground scatter mapping as defined by Equation 3.1.	84
3.2	(a) HF ray-tracing from <i>Samson et al.</i> [1990] showing radar rays modulated by an MSTID passing through the F-Region ionosphere. Concavities in the ionospheric density focus rays on the ground, while convex regions defocus the rays. (b) Geometry used to derive the ground scatter mapping formula (Equation 3.1).	85
3.3	Range-time-intensity (RTI) plot of ground scatter power showing MSTIDs observed by both GBR Beam 6 (Panel a) and BKS Beam 15 (Panel b) during the daylight hours of 19 November 2010. MSTID signatures are observed as bright red stripes with a negative slope. Black dotted lines and boxes have been drawn over MSTIDs and regions selected for further analysis. See text for details.	86
3.4	Horizontal wavenumber spectrum computed using the MUSIC algorithm for 19 Nov 2010 GBR 1401-1601 UT (top) and BKS 1411-1611 UT (bottom). k_x is the North-South wave number; k_y is the East-West wave number. An image processing watershed algorithm determines the location of the largest local maxima within the array.	87
3.5	Stackplot of magnetograms showing the north-south B_x component of the North American-Greenland magnetometers identified in Figure 3.6. At 0910 UT, this chain was located in the morning sector near 0600 MLT. All magnetometers above 70° MLAT show a disturbance that peaks at 0910 UT (indicated by the red vertical dashed line). The green vertical dashed line at 1230 UT and the blue vertical dashed line at 1400 UT indicate the first observations of the MSTIDs at BKS and GBR, respectively.	88

3.6	Map in magnetic coordinates of the 19 November 2010 MSTID event. GBR and BKS show filtered ground scatter power data from a one-minute scan starting at 1440 UT. The black arrows over the radar data indicate the average MSTID propagation azimuth as measured by the MUSIC algorithm. Blue dots indicate the location of ground magnetometer stations. The blue dashed circle is located at 74° MLAT, the likely magnetic latitude of a source auroral surge.	89
3.7	Normalized ground scatter occurrence for BKS from 1 June 2010 through 31 May 2011 as a function of month and local time (UT - 5 hours). The best ground scatter conditions for MSTID observation is found between range gates 10-35 (demarcated with white dashed lines).	90
3.8	Examples of MSTID, quiet, and discard periods used in the statistical study of Section 3.3.2. Each RTI plot shows only ground scatter data from BKS Beam 7 and is divided into four 2-hour windows. (a) MSTID periods are shown in every 2-hour event period on 19 November 2010 from 1400-2200 UT; (b) Quiet periods are shown in every 2-hour period on 13 September 2010 from 1400-2200 UT; (c) Discard periods are shown in every 2-hour period on 16 May 2010 from 1400-2200 UT.	91
3.9	Distributions of the ground scatter fraction (left column) and total spectrum power (right column) for manually identified MSTID events, quiet events, and discard events. Vertical dashed lines in each plot show the threshold values used to reclassify the events in an automated manner. Events with a ground scatter fraction < 0.25 are moved to the discard category. The remaining events are then reclassified as “MSTID events” if the total spectrum parameter ≥ 2800 and “quiet events” if the total spectrum is less than this threshold. See Section 3.3.2 for details.	92
3.10	Distributions of the ground scatter fraction (left column) and total spectrum (right column) for study events after the automatic classification criteria have been applied. See Section 3.3.2 for details.	93
3.11	Occurrence distributions for BKS radar from 1 June 2010 to 31 May 2011 from 0800 to 1700 MLT (i.e. daylight conditions) for (a) MSTID periods, and (b) Quiet periods (good ground scatter without MSTIDs).	94
3.12	Auroral Electrojet (AE) distributions for BKS radar from 1 June 2010 to 31 May 2011 between 0800 and 1700 MLT (i.e. daylight conditions) for (a) MSTID periods, and (b) Quiet periods (good ground scatter without MSTIDs).	95
3.13	MSTID parameter distributions computed using the MUSIC analysis for BKS radar from 1 June 2010 to 31 May 2011 from 0800 to 1700 MLT (i.e. daylight hours) showing (a) frequency and period, (b) horizontal wavelength, (c) horizontal velocity, and (d) azimuth relative to geographic North.	96

3.14	Magnetic local time (MLT) bins of MSTID geographic azimuth for BKS radar from 1 June 2010 to 31 May 2011 from 0800 to 1600 MLT. The dominant population (centered at $\sim 150^\circ$) decreases with MLT, while the secondary population (centered at $\sim 50^\circ$) appears in the afternoon. The MLT bins shown are: (a) 08-10 MLT, (b) 10-12 MLT, (c) 12-14 MLT, and (d) 14-16 MLT. . .	97
3.15	Results from a run of the Horizontal Wind Model 2007 on 19 November 2010 for undisturbed conditions ($A_p = 0$). This array of maps shows the magnitude and direction of the horizontal winds for altitudes from 200-350 km and times that correspond with the MLT time bins presented in Figure 3.14. The blue star indicates the center of the BKS MSTID observation region. The northwest-heading MSTID population in Figure 3.14 only appears when the winds are not parallel to the MSTID propagation direction.	98
3.16	Results of the HINDGRATS reverse ray-tracing model on geographic maps using the climatology results summarized in Table 3.1 as gravity wave seed values. Waves were traced backward from the location of BKS (black diamond) at 220 km altitude. The red trace is the climatological mean, and the green traces are samples of perturbed wave structures. Model runs using yearly-averaged background atmospheres for 14, 16, 18, and 20 UT are shown. For each time, two separate model runs were conducted: the southeastward (dominant) MSTID population originates above the Great Lakes and Canada, and the northwestward (secondary) MSTID population originates over the Atlantic Ocean east of the Carolinas.	99
4.1	Raytrace simulation illustrating how SuperDARN HF radars observe MSTIDs. (a) Fort Hays East (FHE) radar field-of-view superimposed on a 250 km altitude cut of a perturbed IRI. FHE Beam 7 is outlined in bold. (b) Vertical profile of 14.5 MHz raytrace along FHE Beam 7. Background colors represent perturbed IRI electron densities. The areas where rays reach the ground are potential sources of backscatter. (c) Simulated FHE Beam 7 radar data, color-coded by radar backscatter power strength. Periodic, slanted traces with negative slopes are the signatures of MSTIDs moving toward the radar.	124
4.2	Ground scatter measurements during a MSTID-active period on 21 Dec 2012 obtained by the North American SuperDARN radars selected for this study. Radar field-of-views and data are plotted using a ground scatter mapping transformation.	125
4.3	Range-Time-Intensity (RTI) plots from FHE Beam 7 for (a) a MSTID-active day, and (b) a MSTID-quiet day. Inclined dashed lines draw attention to selected MSTID signatures. Format is the same as that used in Figure 4.1c. .	126

4.4	(a) Spectral curves for the FHE 2012-2013 observational season. Each trace represents the MSTID-band power spectral density (PSD) within a 2 hr sampling window. Bold traces marked a2-a4 and b2-b4 correspond with the sampling windows presented in Figure 4.3. Color represents both SuperDARN MSTID Index and classification as MSTID-active (reds) and MSTID-quiet (blues) periods. The black dashed trace shows the seasonal mean. (b) Time series of the FHE MSTID Index values from panel (a).	127
4.5	The strength of the polar vortex measured by the ECMWF Geopotential data at the 1 and 10 mb levels. The Polar Vortex Index ζ for each map is printed in the upper right hand corner (see text for details). Large positive values indicate a strong polar vortex.	128
4.6	Distributions of daytime MSTID parameters for high latitude radars. Each histogram count represents the strongest wave detected in a MSTID-active sampling window. The following parameters are estimated: (a) frequency/period, (b) horizontal wavelength, (c) horizontal phase velocity, and (d) propagation azimuth relative to geographic North. The dashed line in (a) shows the transfer function of the filter applied to the data during processing. The dashed line in (b) indicates the maximum value of horizontal wavelengths allowed in this study.	129
4.7	MSTID parameter distributions for mid latitude radars (same format as Figure 4.6).	130
4.8	Time series of SuperDARN MSTID, polar vortex, and geomagnetic activity for the 2012–2013 observational season. (a) MSTID Index for each of the high latitude radars, with reds showing MSTID-active periods, and blues showing MSTID-quiet periods. (b) Same as (a) for midlatitude radars. (c) Continental MSTID Index (gray and blue traces) and daily number of good sampling windows (dotted line). Background color indicates daily MSTID score and classification, with MSTID-active days in reds and MSTID-quiet days in blues. (d) Polar Vortex Index. (e) Negative <i>AE</i> Index. (f) Sym-H Index. In Panels (c)–(f), gray traces show raw data, while blue traces show a 4-day rolling mean smoothing.	131
4.9	Estimated probability density functions for MSTID-active days and MSTID-quiet days as a function of (a) the <i>AE</i> index, (b) the Sym-H index, and (c) the Polar Vortex Index.	132
4.10	Lagged correlation analysis of candidate MSTID driving parameters with (a) the Continental MSTID Index and (b) the <i>n</i> Data Points quality parameter. Stars indicate the point of maximum correlation magnitude for each parameter. Dashed lines indicate 95% confidence intervals. Positive lag values indicate the number of days by which the MSTID index lags the candidate driver. . .	133

4.11	Time series of ECMWF TOGA zonal mean temperatures averaged for latitudes poleward of 60° N for each MSTID observational season from 2012–2015. The Continental MSTID Index (bold, black trace) and Polar Vortex Index (dotted trace) are superposed. A vertical, dashed line indicates winter solstice. . . .	134
4.12	Same as Figure 4.11, but showing ECMWF TOGA zonal mean zonal winds. Reds indicate eastward winds; blues indicate westward winds. Black arrows point to select events where the stratospheric winds become less eastward and the Continental MSTID Index decreases.	135
4.13	Time series of SuperDARN MSTID, polar vortex, and geomagnetic activity for the 2013–2014 observational season. (a) MSTID Index for each of the high latitude radars, with reds showing MSTID-active periods, and blues showing MSTID-quiet periods. (b) Same as (a) for midlatitude radars. (c) Continental MSTID Index (gray and blue traces) and daily number of good sampling windows (dotted line). Background color indicates daily MSTID score and classification, with MSTID-active days in reds and MSTID-quiet days in blues. (d) Polar Vortex Index. (e) Negative <i>AE</i> Index. (f) Sym-H Index. In Panels (c)–(f), gray traces show raw data, while blue traces show a 4-day rolling mean smoothing.	137
4.14	Time series of SuperDARN MSTID, polar vortex, and geomagnetic activity for the 2014–2015 observational season. (a) MSTID Index for each of the high latitude radars, with reds showing MSTID-active periods, and blues showing MSTID-quiet periods. (b) Same as (a) for midlatitude radars. (c) Continental MSTID Index (gray and blue traces) and daily number of good sampling windows (dotted line). Background color indicates daily MSTID score and classification, with MSTID-active days in reds and MSTID-quiet days in blues. (d) Polar Vortex Index. (e) Negative <i>AE</i> Index. (f) Sym-H Index. In Panels (c)–(f), gray traces show raw data, while blue traces show a 4-day rolling mean smoothing.	138
5.1	Block diagram for a typical automatic amateur reporting network receiving station, including the antenna, receiver, and computer. An ideal station would be able to receive signals omnidirectionally and simultaneously with equal response across all bands of interest (typically 1.8 - 54 MHz). Antennas and SDR receivers that meet the required specifications are available commercially. 150	

5.2	A screenshot of the CW Skimmer program used by the Reverse Beacon Network shown decoding a 3 kHz segment of the 40 m amateur radio band. The left-hand portion of the screenshot shows a waterfall display, which is a short-time Fourier transform that plots spectral power versus time. Visual representations of the Morse code signals can be observed in the waterfall. The right-hand column of the screenshot shows a list of radio call signs detected by the CW Skimmer Morse code decoding algorithm.	151
5.3	(a - d) Reverse Beacon Network (RBN) high frequency propagation path observations from 13 May 2013 beginning at 1505 UT with 15 min integration periods and a 30 min cadence. Paths are color-coded by frequency band. Black dots indicate RBN receiving stations, while blue stars indicate Northern California DX Foundation (NCDXF) beacons. The number of unique transmitting (TX) and receiving (RX) stations within each 15 min period is given in the lower-left corner of each map. Shading indicates the solar terminator. (e) GOES 15 X-ray sensor measurements for the 0.05-0.4 nm (green trace) and the 0.1-0.8 nm (red trace) soft X-ray bands for 13 May 2013 1300-1900 UT. A blue dot at 1605 UT on the red trace indicates the peak of an X2.9 class solar flare and corresponds to a dramatic decrease in RBN activity.	152

List of Tables

1.1	Typical solar wind properties observed near the orbit of the Earth. From <i>Hundhausen</i> [1995], used with permission.	26
3.1	MSTID parameters determined from distribution shown in Figure 3.13 using BKS data from 1 June 2010 through 31 May 2011.	83
4.1	Details of SuperDARN radars used in MSTID study.	122
4.2	Mean μ and standard deviation σ of period, horizontal wavelength, horizontal phase velocity, and propagation azimuth for SuperDARN MSTID observations from 2012 through 2015. This table summarizes Figures 4.6 and 4.7.	123
5.1	Amateur radio bands typically monitored for propagation conditions. Frequency limits listed here are valid in the United States; exact frequency limits will vary based on country.	148
5.2	Selected real-time amateur radio reporting networks.	149

Attribution

Chapters 2 through 5 are manuscripts of studies that have been published in American Geophysical Union journals. I was the lead author and researcher for each of these manuscripts. All co-authors of these studies are identified at the beginning of each respective chapter, along with the citation of the final publication.

Chapter 1

Introduction

1.1 Introduction

Human existence relies on the relationship between the Sun and the Earth, a complex relationship that involves the transfer of mass and energy across vast distances via numerous mechanisms. Space science and space weather are the fields that study the Sun-Earth system. Space science refers to study of the structures and processes of the Sun, the near-Earth space environment, and the upper atmosphere. Space weather monitors the dynamics of these regions and is concerned with their impact on the Earth and society. The sheer size of the Sun-Earth system is one of the biggest challenges in the fields of space science and weather. Access to space is expensive and fraught with technical difficulties, and therefore instrumentation must be strategically deployed in order to successfully study the space environment.

The ionosphere, a weakly ionized portion of the atmosphere located from about 60 to 1000 km altitude above the Earth's surface, is a key region of concern in space science and weather for at least two reasons. First, the ionospheric state significantly impacts human technology

in both advantageous and adverse ways. This makes the ionosphere worth studying in its own right. Second, the ionosphere is the coupling region between the neutral atmosphere and space, and thus allows for the remote sensing of processes in those regions. This property makes the ionosphere useful for overcoming the difficulties imposed by the vastness of the space environment.

This dissertation presents a series of studies that seek to answer questions regarding commonly observed ionospheric disturbances. Each of the studies either presents a novel approach to remote sensing the ionosphere, or it identifies the underlying cause of the observed disturbances in a way that significantly advances the current understanding of ionospheric or magnetospheric physics. This introductory chapter provides background information and motivation for each of these studies. Section 1.2 presents an overview of the solar-terrestrial environment. Section 1.3 describes the ground-based ionospheric measurement systems that obtained the majority of observations used in this work. Section 1.4 introduces and discusses the importance of each type of ionospheric perturbation studied in this dissertation. Finally, Section 1.5 states the dissertation objectives and organization.

1.2 The Solar-Terrestrial Environment

The Solar-Terrestrial Space Environment is a system in which energy and mass are transferred from the Sun to the Earth. Figure 1.1 presents an illustration (not to scale) of this system. The primary regions of the space environment include the Sun and its solar wind (dashed, white lines between the Sun and Earth), the Earth's magnetosphere (blue lines surrounding the Earth), and the Earth's ionosphere and neutral atmosphere (near the Earth's surface).

Each of these regions are defined primarily by the origin and properties of their constituent particle populations. The solar wind, magnetosphere, and ionosphere are made of plasmas,

or electrically charged gases with approximately equal numbers of positively and negatively charged particles that are sensitive to electromagnetic forces. The neutral atmosphere consists of non-electrically charged particles, but is co-located and thus coupled with the ionosphere at certain altitudes. Thus, the physics of plasma interactions plays heavily throughout the entire Solar-Terrestrial Environment. The solar wind, magnetosphere, ionosphere, and neutral atmosphere are discussed in more detail in Sections 1.2.1–1.2.4.

1.2.1 Solar Wind and Interplanetary Magnetic Field

The majority of energy and dynamics in the Solar-Terrestrial Environment originates from the Sun, which emits mass and energy into space through two primary mechanisms. First, energy is emitted as electromagnetic (EM) radiation. Figure 1.2 shows the spectral radiance of this EM radiation as a function of wavelength. Second, mass and energy is carried by a radially moving solar wind (SW) plasma. The solar wind carries with it a magnetic field known as the interplanetary magnetic field (IMF). Typical characteristics of the SW and IMF are summarized in Table 1.1. These characteristics can vary substantially with time, and are the primary drivers of space weather. Long term variations of solar activity follow an approximately 11 year solar cycle.

1.2.2 The Magnetosphere

The blue lines surrounding the Earth in Figure 1.1 depict the Earth's geomagnetic field, or magnetosphere. The magnetosphere is generated by the Earth's internal magnetic field, which is dipolar to first order with a dipole moment $\mu \approx 8 \times 10^{15} \text{ T}\cdot\text{m}^{-3}$. The magnetic field comes out of the geomagnetic south pole and returns into the geomagnetic north pole and is tilted approximately 11° relative to the Earth's rotational axis. Although Figure 1.1 depicts

the magnetosphere as being symmetric across the ecliptic, the tilt of both the dipole axis and Earth's rotational axis results in a magnetosphere that is not symmetric in reality.

The plasmas of the solar wind and magnetosphere are collisionless plasmas with extremely high conductivities. Therefore, the background magnetic field is frozen into the plasma. These types of plasmas do not easily mix, and therefore the magnetosphere is a substantial barrier to solar wind flow. The solar wind constantly buffets the magnetosphere, which causes it to compress on the dayside and stretch into a long tail on the nightside. When the solar wind pressure increases, the dayside magnetosphere becomes more compressed. The majority of solar wind flow is diverted around the magnetosphere.

The solar wind transfers mass and energy to the magnetosphere via both viscous interactions [Axford and Hines, 1961] and magnetic reconnection [Dungey, 1961]. Of these two processes, magnetic reconnection is the most important. Magnetic reconnection can occur when the magnetic fields of two adjoining plasma populations are antiparallel, and is illustrated in Figure 1.3. This occurs on the dayside magnetopause when the north-south component of the interplanetary magnetic field is southward (IMF $B_z < 0$). When this condition is satisfied, the magnetic field lines carried by the solar wind merge with those from the Earth, creating "open" field lines. Plasma particles from both the magnetospheric and solar wind populations can now stream freely and mix along these field lines. The momentum from the solar wind continues to push the open field lines from the dayside to the nightside of the magnetosphere, where they are draped over the magnetotail. Eventually, open magnetotail field lines from the north and south are pushed together, and magnetotail geometry allows another reconnection site to be created. Newly closed field lines are then formed and eventually return to the dayside magnetosphere. This process repeats in a cycle known as the Dungey model of magnetospheric convection.

1.2.3 The Ionosphere

The ionosphere is a region of weakly ionized plasma that forms from the ionization of the neutral atmosphere. It is typically located in a region between 60 to 1000 km above the Earth's surface. Figure 1.4 shows a typical daytime ionospheric and atmospheric composition profile based on mass spectrometer measurements obtained during the international quiet solar year (from *Luhmann* [1995], after *Johnson* [1969]). The ionized species have densities between 10^2 and 10^6 cm^{-3} , while the neutral atmosphere has population densities that are orders of magnitude larger.

The electron density profile (Figure 1.4, thick line marked e^-) defines the regions of the ionosphere. The D region is located from the bottom of the ionosphere up to 90 km altitude, the E region from about 90 to 130 km altitude, and the F region from 130 km altitude to the top of the ionosphere. In addition to the structure shown in Figure 1.4, the F region may split into F_1 (peak ~ 170 km) and F_2 (peak ~ 250 km) layers during the day. The shape of the electron density and ionospheric composition profiles are due to a balance of various production, loss, and transport processes. The dominant production mechanism is the photoionization of neutral particles due to solar ultraviolet and x-ray radiation. In general, higher energy radiation is required to penetrate further into the atmosphere and cause ionization at low altitudes. The dependence of the ionosphere on atmospheric chemistry is the cause of strong coupling from the neutral atmosphere to the ionosphere.

The ionosphere is threaded by the Earth's geomagnetic field, which leads to strong coupling between the magnetosphere and the ionosphere. At high latitudes, magnetic field lines from far out in space vertically enter into or leave from the atmosphere (see Figure 1.1). Charged particles can flow easily along magnetic field lines and precipitate into the high latitude atmosphere, causing aurora and impact ionization. Because charged particles cannot move

easily across field lines, motion in the high latitude geomagnetic field can force ionospheric plasma to move horizontally. Short and medium time-scale variations in the geomagnetic field arise from processes in the magnetosphere, such as magnetospheric convection discussed in Section 1.2.2. As a magnetic field line moves in the magnetosphere, it will force the ionospheric plasma at its footpoint to move as well. This creates organized ionospheric flows that can provide information about processes in space.

1.2.4 The Neutral Atmosphere

As discussed in Section 1.2.3, the neutral atmosphere is the primary source of ionospheric plasma. Figure 1.4 shows typical daytime neutral atmospheric composition profiles for the most significant species above 100 km altitude: He, O, N₂, O₂, and Ar. Gravity plays a large role in ordering these species, which allows the lightest gases to reach significantly higher altitudes than the heaviest gases. Almost all of the neutral species have number densities greater than 10^5 cm^{-3} between 100 and 800 km altitude. This is orders of magnitude greater than the ionized species.

Like the ionosphere, the neutral atmosphere is also divided in regions by altitude. However, inflections in neutral gas temperature, rather than density, are used to define these regions. Figure 1.5 shows an example neutral atmospheric temperature profile generated using the NRL-MSIS empirical model [Picone *et al.*, 2002]. In the troposphere, which typically extends from the ground to approximately 10 km altitude, the atmospheric temperature monotonically decreases. Temperatures warm again with altitude in the stratosphere, which is located between approximately 10 and 50 km altitude. The mesosphere (50 to 85 km altitude) and the thermosphere (85 to 600 km altitude) are similarly defined. The mesosphere and thermosphere are co-located with the ionosphere.

Like the ionosphere, neutral atmospheric processes are primarily driven by both solar radiation and local chemistry. Additionally, geographic topography, bodies of water, and the rotation of the Earth also play significant roles. As a result, winds, waves, and convective activity form in the neutral atmosphere, covering a wide range of spatial and temporal scales. These processes have the potential to significantly impact the ionosphere, due to the dependencies discussed in Section 1.2.3.

1.3 Ionospheric Remote Sensing Techniques

The studies presented in this dissertation rely primarily on measurements made by ionospheric remote sensing networks based on high frequency (HF, 3–30 MHz) radio sounding techniques. Section 1.3.1 describes the Super Dual Auroral Radar Network (SuperDARN), a well-established network of ionospheric radars. Section 1.3.2 introduces the possibility of using new amateur radio receiving networks for conducting space weather and space science research.

1.3.1 SuperDARN

Overview

The Super Dual Auroral Radar Network (SuperDARN) is an international network of high frequency radars designed to remote sense the ionosphere [Greenwald *et al.*, 1995; Chisham *et al.*, 2007]. Figure 1.6 shows the nominal fields-of-view (FOV) of the SuperDARN network as of March 2016. Goose Bay (GBR), the first HF radar of the SuperDARN network, began operation in 1983 and continues to make measurements as of this writing. The FOVs in Figure 1.6 are color-coded according to geophysical region. Blue (high latitude) radars look into the

auroral zone, and constitute the original chain of SuperDARN radars. Recent expansion of SuperDARN has extended the network to the subauroral (mid latitude, orange), and the polar cap (green) regions. Adjacent radars have crossed FOVs, allowing for the two-dimensional resolution of horizontal motion.

Figure 1.7 shows a photo of the SuperDARN radar at McMurdo Station, Antarctica, which is a typical example of the current SuperDARN design. Each radar has a main linear phased array of 16 antennas capable of both transmitting and receiving, and a 4 antenna receive-only interferometer array for elevation angle of arrival measurements. Newer radars, such as the one shown in Figure 1.7, use a twin-terminated folded dipole antenna design in conjunction with a corner reflector. Older style radars use log-periodic antennas. The phased array of antennas allows for electronic steering of the radar. Typically, 16 to 22 beams are scanned over a period of 1 to 2 minutes. Custom radar modes may also be run.

HF Propagation and Scattering Targets

The primary purpose of SuperDARN radars is to measure the velocity of F region ionospheric plasma flows in the mid and high latitude regions. This is accomplished by measuring the Doppler velocity of ionospheric plasma irregularities detected by coherent (Bragg) scattering, as depicted in Figure 1.8. In Bragg scattering, radar reflections from multiple structures combine in phase to produce a strong return signal. While the strong returns of coherent scatter allow relatively low power radars to be used, two conditions must be satisfied: (1) ionospheric irregularities with scale sizes on the order of the radar wavelength must be present, and (2) radar rays must be orthogonal to the irregularities. These irregularities are typically aligned with the background geomagnetic field. Because the magnetic field in the high latitude region is nearly vertically inclined, the orthogonality condition in the F region ionosphere cannot be met using line-of-sight propagation. This precludes SuperDARN from

using frequencies above 30 MHz.

The ionosphere has the ability to bend the propagation path of radio signals in the HF (3–30 MHz) band. By operating in the HF bands, SuperDARN radars can take advantage of this bending to satisfy the orthogonality condition. Figure 1.9 illustrates this by showing the results of raytracing 10 MHz (bottom panel) and 15 MHz (top panel) radar signals through a model ionosphere. The gray curves represent individual radar rays, while the background colors show model electron densities. Indices of refraction may be calculated as a function of radio frequency and electron density, and hence gradients in the ionospheric plasma density cause the rays to bend. Higher frequency rays are bent less than lower frequency rays, as evidenced by comparing the 10 and 15 MHz panels. Rays with high elevation angles escape the ionosphere and are lost to space, while rays with lower elevation angles are bent back toward Earth. Signals that return to Earth may be reflected by the ground, allowing the process to continue for multiple hops.

In Figure 1.9, dashed purple lines indicate the inclination of the background magnetic field. Dark black curves indicate the locations where the radar rays are within 1° of orthogonality to the background field. These are also the locations the radar would detect scatter if the appropriate size¹ ionospheric irregularities are present. Radar returns generated by this process are known as “ionospheric scatter”, and typically map to processes in the magnetosphere. Radar returns may also be produced where rays backscatter off of the Earth’s surface. This is known as “ground scatter”. Although ground scatter is not typically interesting in the field of space and ionospheric physics, Figure 1.9 shows that the rays can pass through the ionosphere before reaching the ground. Modulation imposed onto ground scatter signals by the ionosphere is useful for studying the ionospheric state.

¹decameter scale for HF frequencies

Example SuperDARN Data

The research presented in this dissertation primarily uses two types of SuperDARN measurements: the Doppler velocity and the signal-to-noise ratio (SNR). The SNR is sometimes referred to as the “power” parameter. Figure 1.10 presents an example of SNR measurements collected by the Blackstone, Virginia (BKS) SuperDARN radar on 16 November 2015 during a 1-minute scan across 20 beams starting at 1600 UT. This data is primarily composed of ground scatter measurements, with the high SNR region (bright yellows and reds) showing the effects of ionospheric focusing. This can be compared to the first hop of the ground scatter in the ray tracings of Figure 1.9. Also apparent in this SNR data are wavefronts indicative of medium scale traveling ionospheric disturbances (MSTIDs), a central topic of this dissertation.

Figure 1.11 presents example time series of both the Doppler velocity and SNR parameters in Range-Time-Intensity (RTI) format. This data is from BKS Beam 15 (gray beam on map in Figure 1.10) for the period 0000–2359 UT on 16 November 2015. Local time is approximately UT-5 hours. The three small panels at the top of the figure provide operating information such as sky noise, radar frequency, and operating mode. The top colored panel shows Doppler velocity, while the bottom colored panel shows SNR. Gray shading of the velocity parameter indicates ground scatter that has been identified based on low velocity and narrow spectral width values (see *Blanchard et al.* [2009] and *Ribeiro et al.* [2012] for details). Positive Doppler velocities indicate motion toward the radar, while negative velocities indicate motion away from the radar. Slant range is the distance from the radar to the target calculated using the speed of light and the gated return time of the radar echo.

The diurnal effects caused by the day-night variations of ionospheric density are immediately apparent in both the velocity and SNR parameters presented in Figure 1.11. Local night

(approximately 0000–1200 UT) is dominated by ionospheric scatter with moderate to fast velocities moving away from the radar. At local dawn (1200 UT), the ionospheric scatter is replaced by a ground scatter band. Ionospheric focusing causes strong SNR values to be observed in the middle of the ground scatter band. At dawn, this band starts at farther ranges, then moves inward during the day as the ionosphere becomes stronger, and finally moves outward again at dusk. The range discontinuity at 1300 UT is due to a radar operating frequency change from 11 to 15 MHz. The movement of scatter to farther ranges with an increase in frequency is consistent with the raytracing of Figure 1.9. Range oscillations in the ground scatter band are signatures of MSTIDs, which are discussed in more detail in Section 1.4.2.

1.3.2 Amateur Radio Networks

Amateur radio is an international hobby in which governmentally licensed radio operators, or hams, conduct non-commercial, two-way radio transmissions on designated amateur radio frequencies. Hams routinely communicate long distances on the HF bands. These communications are governed by the same ionospheric and space weather processes that affect SuperDARN radars. In fact, it is the multi-hop propagation shown in the raytracing of Figure 1.9 that allows amateur radio operators to utilize links paths thousands of kilometers long. Figure 1.12 shows an example of a typical residential HF amateur radio station, capable of transmitting 100 W of power using a variety of modes.

Recently, amateur radio operators have been working together to develop automated receiving networks designed to monitor amateur radio communications and report observations back to a central server. These receiving networks are global-scale networks that typically focus on the HF bands. One such network is the Reverse Beacon Network (RBN,

<http://www.reversebeacon.net>), which automatically decodes and Morse Code and radio teletype (RTTY) transmissions. Figure 1.13 presents an example of RBN observations collected from 1505–1520 UT on 13 May 2013. Curves indicate observed communication link paths, color coded by frequency. A black dot on one end of each curve indicates the RBN receiver location, while the unmarked end of each curve represents the transmitter location.

Although networks such as the RBN have been built for the purpose of supporting amateur radio activities such as contesting and DXing², the routine, large-scale monitoring of trans-ionospheric radio links suggests an interesting question. Is it possible to use these observations for the purpose of studying space science and space weather? The answer to this question is explored in Chapter 5 by studying the effects of an Earth-directed solar flare on amateur radio communications observed by the RBN.

1.4 Ionospheric Perturbations

In this section, three different types of ionospheric perturbations are introduced. Each of these is associated with a question that this dissertation will address. Section 1.4.1 discusses ionospheric pulsations that originate in the magnetosphere. Section 1.4.2 discusses ionospheric disturbances that are associated with neutral atmospheric gravity waves. Finally, Section 1.4.3 discusses the impact of solar flares on the ionosphere.

1.4.1 Magnetospheric Pi2 ULF Pulsations

Waves and pulsations with frequencies ranging from 1.5 mHz to 5 Hz (period 0.2 to 600 s) are often observed in various parameters throughout the space environment [*Jacobs et al.*, 1964].

²making radio contact with distant stations

These disturbances are appropriately referred to as Ultra Low Frequency (ULF) waves and pulsations. They are propagated long distances by various modes of magnetohydrodynamic (MHD) waves, which are slowly-varying plasma waves resulting from both magnetic and fluid pressure forces. ULF waves are typically of magnetospheric origin, and may be detected by magnetometers both on spacecraft and on the Earth's surface. Because the geomagnetic field threads the ionosphere, magnetospheric ULF waves can also move ionospheric plasma and hence be sensed by SuperDARN radars.

In a cold plasma, such as that of the plasmasphere, two MHD wave modes can exist. One is the shear Alfvén wave, while the other is the fast-mode or compressional wave [Kivelson, 1995]. The shear Alfvén wave can only propagate parallel to a magnetic field line, and does not affect the plasma density, pressure, or total magnetic field. Instead, it carries with it a field-aligned current and causes the magnetic field to bend transverse to the wavenumber \mathbf{k} . It propagates with phase velocity $v_p = v_A \cos \theta$, where θ is the angle between \mathbf{k} and the magnetic field \mathbf{B} , and v_A is the Alfvén velocity defined as:

$$v_A = \frac{B}{\sqrt{\mu_0 \rho}} \quad (1.1)$$

where B is the magnetic field magnitude, μ_0 is the permeability of free space and ρ is the plasma mass density. The fast-mode compressional wave, on the other hand, does perturb plasma density, pressure, and magnetic field magnitude. It can propagate in an arbitrary direction relative to the background magnetic field with phase velocity $v_p = v_A$.

Pi2 pulsations are one particular class of magnetospheric ULF waves. They are characterized by a period of 40 to 150 s and have an irregular waveform with a duration of about 10 minutes [Jacobs *et al.*, 1964]. Although they have been observed under various geomagnetic conditions, Pi2s are most often associated with a type of large-scale magnetospheric reconfiguration

known as a substorm (discussed below). Well-accepted models exist for substorm Pi2s observed in the high-latitude auroral zone; however, the source and generation mechanism of Pi2s at mid and low latitudes continues to be an open question.

Substorms

Substorms are dramatic reconfigurations of the magnetosphere that lead to a sudden release of energy from the magnetotail toward the Earth (see reviews by *Lui* [1996], *Baker et al.* [1996], and *Kepko et al.* [2014]). The substorm is a special case of the Dungey convection cycle (Section 1.2.2 and Figure 1.3) in which the rate of dayside reconnection exceeds that of nightside reconnection for an extended period of time. Substorms have three main phases: the growth phase, the expansion phase, and the recovery phase.

The substorm growth phase begins with a southward turning of the Interplanetary Magnetic Field (IMF). This causes dayside magnetic reconnection, the erosion of magnetic flux from the dayside, and the loading of flux into the nightside magnetotail. This flux loading causes tail magnetic field lines to stretch and squeeze together, thereby thinning the central current sheet. During the growth phase, nightside flux does not return to the dayside. The growth phase typically lasts 1–2 hours and ends suddenly with the onset of the expansion phase [*Iijima and Nagata*, 1972].

During the substorm expansion phase, the mass and energy stored in the magnetotail is suddenly released toward Earth. Although the physics of expansion onset are still under debate, certain observational details are well established [*Kepko et al.*, 2014]. In particular, the near-Earth transition region from dipolar to stretched field lines experiences a sudden dipolarization [*Baumjohann et al.*, 1999] and injection of energetic particles [*Parks and Winckler*, 1968; *Belian et al.*, 1981]. In this same region, the cross tail current is diverted

along field-aligned currents into the auroral ionosphere to establish the substorm current wedge (SCW), as illustrated in Figure 1.14 by *McPherron et al.* [1973]. A near-Earth neutral line (magnetic reconnection region) is formed between 20–30 Earth radii down the tail [*Baumjohann et al.*, 1999]. Additionally, Earthward-moving fast plasma flows or bursty bulk flows (BBFs) can be observed between the dipolar inner magnetosphere and the near-Earth neutral line [*Angelopoulos et al.*, 1994]. These features are illustrated in Figure 1.15.

As the expansion phase progresses, magnetic flux piles up in the inner magnetosphere and the dipolar-to-stretched field line interface moves farther down the tail. Approximately 45 minutes after onset, this interface reaches the location of the near-Earth neutral line, signaling the beginning of the recovery phase [*Baumjohann et al.*, 1999].

Candidate Pi2 Mechanisms

It is during the onset of substorm expansion that Pi2s are most often observed [*Saito*, 1969; *Saito et al.*, 1976]. In the nightside high latitude region ($L \gtrsim 6$)³ during a substorm, the mechanism of Pi2 generation is widely believed to conform to the transient response model [*Baumjohann and Glassmeier*, 1984]. When the substorm current wedge is first being established, current-carrying shear Alfvén waves are launched along magnetic field lines into the auroral ionosphere. However, an impedance mismatch at the ionosphere causes a partial wave reflection [*Mallinckrodt and Carlson*, 1978]. The waves bounce between conjugate ionospheres until the wave dissipates after a few cycles. Joule heating of the ionosphere, wave conversion to kinetic particle energy, and coupling to fast mode waves are all possible contributors to the Alfvén wave dissipation [*Keiling and Takahashi*, 2011]. These bouncing Alfvén waves are represented by green arrows in Figure 1.15. Each wave reflection generates an ionospheric current pulse, and so the transit time of the reflecting Alfvén waves specifies

³ $L = 1/\cos^2 \lambda$ where λ is magnetic latitude [*McIlwain*, 1961]

the period of the Pi2 pulsations observed on the ground. High latitude magnetometers directly under the ionospheric footprint of these currents observe very strong Pi2s, while subauroral ($4 \lesssim L \lesssim 6$) stations detect weaker pulsations generated by the more distant SCW field aligned currents in space.

Much debate exists regarding the source of Pi2s observed at mid and low latitudes ($L \lesssim 4$). The magnetic field lines at these latitudes map into the plasmasphere (blue region in Figure 1.15). The plasmasphere is an inner magnetospheric region with primarily dipolar field line configuration that is filled with a cold, dense, co-rotating plasma. Compressional energy is thought to drive Pi2s within this region, but even this is uncertain at the plasmopause, or outermost boundary of the plasmasphere, which may still be sensitive to the transient response of the SCW. Possible sources of compressional energy include impulsive disturbances associated with SCW formation [Yumoto *et al.*, 1989; Pekrides *et al.*, 1997] and Earthward-moving BBFs braking against the inner dipolar region [Kepko and Kivelson, 1999; Kepko *et al.*, 2001]. Finally, there is also uncertainty as to the mechanism generating the characteristic Pi2 period. Zhu and Kivelson [1989] and Sutcliffe and Yumoto [1989] postulate that a broadband compressional impulse couples with a cavity mode, in which the plasmasphere itself acts as a resonant oscillator. Kepko and Kivelson [1999] and Kepko *et al.* [2001] show observations suggesting that the BBFs directly drive the Pi2s, with the inter-BBF period specifying the ground Pi2 period.

Pi2 Pulsations Research Questions

Chapter 2 of this dissertation presents a case study of midlatitude substorm Pi2s observed simultaneously with a network of ground magnetometers, two THEMIS spacecraft, and the Blackstone, Virginia SuperDARN radar. Using these observations, this study asks “What is the source of energy and mechanism of generation of the observed Pi2 pulsations?”

1.4.2 Medium Scale Traveling Ionospheric Disturbances

Almost 70 years after G. H. Munro first reported on Medium Scale Traveling Ionospheric Disturbances (MSTIDs) in a 1948 letter to *Nature* [Munro, 1948], MSTIDs continue to constitute an active area of research. MSTIDs are quasiperiodic perturbations of ionospheric density with periods between 15 to 60 minutes, horizontal wavelengths of several hundred kilometers, and horizontal phase velocities of less than approximately 300 m s^{-1} [Ogawa *et al.*, 1987; Samson *et al.*, 1990]. Two primary classes of MSTIDs exist. One is believed to be generated by electrodynamic instabilities [Perkins, 1973; Kelley, 2011; Miller *et al.*, 2014], while the other class is thought to be caused by interactions of the ionosphere with neutral Atmospheric Gravity Waves (AGWs) [Hines, 1960; Hooke, 1970]. This dissertation focuses on the class of MSTIDs associated with AGWs.

The underlying causes of MSTIDs make them scientifically important for understanding ionospheric electrodynamics and neutral atmosphere-ionospheric coupling. Because MSTIDs can impact applications such as radio communications, navigation, and direction finding, MSTIDs also have a practical importance. In spite of years of research, many aspects of MSTIDs, including their underlying cause, are still not well understood.

Example MSTID Observations

SuperDARN radars routinely observe MSTIDs in daytime ground scatter. Figure 1.16 shows an example of MSTID wavefronts observed by the Blackstone (BKS) radar in a series of four 1-minute power scans, each separated by 5 minutes. Each map shows a band of ground scatter resulting from ionospheric ray focusing, as first introduced in Section 1.3.1. In an ideal, smooth ionosphere, such as the one presented in Figure 1.9, the ground scatter band would be smooth and stationary. However, MSTIDs propagating through the radar field-of-view (FOV)

cause the ground scatter band in Figure 1.16 to move in and out in range. The MSTIDs also add fine structure to an otherwise smooth ground scatter band. A time series of the gray shaded beam (BKS Beam 15) in Figure 1.16 is available in Figure 1.11.

Figure 1.17 further illustrates both MSTID structure and SuperDARN MSTID observations by presenting a 14.5 MHz SuperDARN raytrace through the International Reference Ionosphere (IRI) perturbed with a model MSTID. The top and bottom panels show the same region separated by 20 minutes. The yellow enhancements of electron density can be seen to move toward the radar with time, causing the skip focusing region to move as well. This is the basic mechanism causing the power variations observed in Figure 1.16.

Review of MSTID Climatologies

MSTIDs may be observed using a variety of techniques, including HF radars (e.g., SuperDARN), incoherent scatter radars, optical instrumentation, in-situ spacecraft, and total electron content instrumentation (e.g., GPS-TEC). These systems have been used to routinely observe MSTIDs all over the globe, and generally report the same findings regardless of latitudinal region or hemisphere. Specifically, MSTID activity peaks in the Fall and Winter with the majority of MSTIDs propagating equatorward. Selected observational studies at high latitudes (both hemispheres) include *Ogawa et al.* [1987], *Samson et al.* [1989, 1990], *Bristow et al.* [1994, 1996], *Bristow and Greenwald* [1996], *Ishida et al.* [2008], and *Hernández-Pajares et al.* [2012]. Extensive work has also been done at midlatitudes (both hemispheres), including *Hunsucker and Tveten* [1967], *Georges* [1968], *Evans et al.* [1983], *Waldock and Jones* [1986], *Kotake et al.* [2007], *Ishida et al.* [2008], *Hernández-Pajares et al.* [2012], and *Grocott et al.* [2013].

Possible MSTID Source Mechanisms

Although the MSTID climatology is relatively well established for both latitudinal regions, it has not been possible to unambiguously identify the source of the observed MSTIDs. In select cases, the source of particular MSTIDs can be identified. Examples include the 2011 earthquake in Tohoku, Japan [*Tsugawa et al.*, 2011] and the 2013 tornado in Moore, Oklahoma [*Nishioka et al.*, 2013]. However, these were dramatic, relatively isolated “point source” events. Source identification for the background climatological MSTID populations described above is significantly more difficult. MSTIDs are ubiquitous [*Ogawa et al.*, 1987], can propagate long distances [*Ishida et al.*, 2008], and exist in an atmospheric regime that is difficult to measure. This means it is not typically possible to unambiguously track a single MSTID wavefront from its region of origin.

The dominant equatorward propagation reported in the observational studies listed above naturally led to a search for a source at high latitudes. One hypothesis is that mechanisms related to space weather provide the energy to generate the MSTIDs. *Hunsucker and Tveten* [1967] suggested that auroral sources 5000 km away were responsible for MSTID measurements made with an HF radar in Colorado. *Chimonas and Hines* [1970] showed theoretically that auroral currents and particle precipitation could launch AGWs via Lorentz forcing and Joule heating. *Francis* [1974] developed the Earth Reflected Wave model, which showed how AGWs launched by auroral sources could propagate equatorward and couple with the ionosphere to create MSTIDs. *Samson et al.* [1989, 1990] and *Bristow et al.* [1994] used this mechanism to explain their MSTID observations made with high latitude HF SuperDARN radars. Recent papers, such as *Grocott et al.* [2013], have also cited space weather mechanisms as the most likely cause.

The space weather mechanism is quite attractive as it has good theoretical support and

easily explains the dominant equatorward propagation reported in MSTID observational studies. However, all of the studies listed above report either weak or no correlation of MSTID occurrence with typical indices of geomagnetic activity. Studies that identify space weather activity as the source [e.g., *Hunsucker and Tveten, 1967; Samson et al., 1990; Bristow et al., 1994*] typically do so by showing case studies in which the MSTIDs appear to come from areas of high activity such as the auroral cusp or convection reversal boundary. However, they cannot show definitive measurements of MSTIDs being generated at that region and propagating to the final point of observation.

AGWs generated by processes internal to the middle and lower atmosphere are another possible source of the climatological MSTIDs. Many atmospheric processes can generate AGWs, including forcing from thunderstorms and hurricanes [*Vadas and Liu, 2009*], tornadoes [*Nishioka et al., 2013*], variations in wind systems [*Gerrard et al., 2002*], and others. It has been observationally and theoretically demonstrated that these AGWs can couple to the ionosphere and generate MSTIDs [e.g., *Earle et al., 2008; Vadas and Crowley, 2010; Nishioka et al., 2013*]. Given the large number of atmospheric processes that can generate AGWs, a hypothesis of a lower/middle atmospheric source might be a plausible alternative to space weather sources. However, no atmospheric source capable of generating a population of fall and winter equatorward propagating AGWs has ever been definitively linked to the climatological MSTID population described above.

The Polar Vortex

The polar vortex is a large-scale cyclonic wind system that forms in the high latitude stratosphere beginning in the late fall due to strong meridional temperature gradients. It consists of a cold core of slow-moving air bounded by a fast-moving polar vortex jet. The jet is a region that is associated with high levels of atmospheric gravity wave activity [*Wu*

and Waters, 1996; Whiteway *et al.*, 1997; Gerrard *et al.*, 2002]. Figure 1.18 is a schematic from Gerrard *et al.* [2002] that depicts nominal arctic polar vortex structure. In the lower stratosphere, temperatures are coldest in the vortex core with a positive temperature gradient directed equatorward. The cool core temperatures of the lower stratosphere are due to radiative cooling during the polar night. The upper stratosphere has opposite thermal structure than that of the lower stratosphere. These warm temperatures can be attributed to momentum deposition of AGWs at high altitudes [e.g., Kanzawa, 1989; Hitchman *et al.*, 1989]. The horizontal temperature gradients create a pole-centered low pressure system, which in combination with Coriolis effects, creates a high-speed jet (eastward/westerly in the northern hemisphere) located between about 30 km (10 mb) and 50 km (1 mb) altitude.

The high levels of AGW activity associated with the vortex jet are likely due to polar vortex jet modulation of upward propagating waves generated at low altitudes [Whiteway *et al.*, 1997]. A large number of the low-altitude waves are generated by wind flow over rough terrain and have very low horizontal phase speeds. The polar vortex jet can modulate them by both Doppler shifting and critical level filtering. This can be explained using a simplified gravity wave dispersion relation, where the vertical wavelength λ_z is defined as:

$$\lambda_z = (c - U \cos \theta) \tau_b \quad (1.2)$$

Here c is the AGW horizontal phase speed, U is the background wind speed, θ is the angle between the wind and wave propagation direction, and τ_b is the buoyancy period of the atmosphere. In the Doppler shift mechanism, the vertical wavelength λ_z of waves with small phase speeds c become proportional to the background wind speed U . The high speeds of the vortex jet can shift these AGWs to longer vertical wavelengths which can then grow in amplitude and incite instabilities. In critical level filtering, it can be seen that λ_z will vanish and the wave will dissipate when the horizontal phase velocity matches the speed

and direction of the background wind. If there is substantial variability in wind direction and velocity between the ground and the stratosphere, many upward waves will experience critical levels and be dissipated. However, the winds of the vortex jet typically flow in a uniform direction, filtering out a minimum of AGWs. Observations of AGWs by *Whiteway et al.* [1997] and *Gerrard et al.* [2002] are consistent with these mechanisms.

To summarize, the polar vortex is strong in the fall and winter, is located in a high latitude region, and is a known source of upward propagating AGWs. Thus, it is a strong candidate source of F region MSTIDs.

MSTID Research Questions

MSTID research is presented in Chapters 3 and 4. Chapter 3 begins by using data from the single midlatitude radar at Blackstone, Virginia. This study asks how often midlatitude MSTIDs are observed as function of month, local time, and geomagnetic activity level. It also asks what are the observed horizontal wavelengths, periods, propagation velocities, and propagation azimuths. The answers to these questions are then used to postulate on the source of midlatitude MSTIDs.

Chapter 4 builds on the work started in Chapter 3 by utilizing multiple high and mid latitude SuperDARN radars distributed across the North American continent. Like Chapter 3, Chapter 4 asks what are the occurrence statistics and characteristics of the observed MSTIDs and what is their relationship to geomagnetic activity. However, Chapter 4 also asks some very important new questions, including, “How are high and mid latitude MSTIDs related?” and “What is the relationship of MSTIDs to the polar vortex?”

1.4.3 Ionospheric Impacts of Solar Flares

Under normal conditions, the electromagnetic spectrum at the surface of the Sun is similar to that of a 5786 K black body with wavelengths that range from approximately 10^{-7} to 10^{-1} m, as shown in Figure 1.2. Ideally, these quiescent conditions generate dayside F region ionospheric densities that are strong enough to refract HF radio signals back to Earth, but also D region ionospheric densities that are sufficiently weak such that absorption due to collisional damping does not significantly affect the desired radio transmissions. These conditions are ideal for long-distance HF radio communications. However, the Sun does not always produce a stable, quiescent spectrum. Magnetic instabilities can form on the surface of the sun and give rise to solar flares, which are short-lasting energetic events that alter the solar spectrum. Most notably, a sudden increase in ultra-violet (UV) and X-ray irradiance is observed, as indicated in Figure 1.2. Large solar flares can lead to sudden enhancements of the D region ionosphere that can absorb HF radio energy and prevent communications via ionospheric paths. This phenomena is known as a “radio blackout.”

Solar Flare Research Questions

Chapter 5 presents a short study that asks if crowd-sourced observations of “signals of opportunity” produced by amateur radio operators could be used to make systematic ionospheric observations. Because the gross effects of solar flares on the ionosphere and HF radio communications are well known [e.g., *Collins et al.*, 1961; *Davies*, 1990], Chapter 5 uses a solar flare event to address this engineering question, rather than ask a scientific question about the flare itself.

1.5 Research Questions and Objectives

This introduction has provided the background and motivation for research questions pertaining to three different topics in the field of ionospheric and magnetospheric physics. These research questions, along with the dissertation organization and objectives, are summarized here:

Chapter 2: Magnetospheric Pi2 ULF Pulsations

1. What is the source of energy and mechanism of generation of Pi2 pulsations observed in the midlatitude nightside ionosphere?

The objective of Chapter 2 is to identify the magnetospheric source of nightside midlatitude substorm Pi2 ULF pulsations using both ground-based and in-situ measurements.

Chapters 3 and 4: Medium Scale Traveling Ionospheric Disturbances

1. How often do midlatitude daytime AGW-MSTIDs occur as a function of month and local time?
2. What are the distributions of daytime AGW-MSTID characteristics (period, horizontal wavelength, velocity, and direction) in the high latitude and midlatitude regions?
3. How are daytime AGW-MSTIDs in the high latitudes and midlatitudes related?
4. What is the relationship of daytime AGW-MSTIDs in the high latitudes and midlatitudes to geomagnetic activity and polar atmospheric dynamics?
5. What are the sources of the daytime AGW-MSTIDs observed in the high latitude and midlatitude regions?

The objective of Chapter 3 is to develop a climatology of daytime midlatitude medium scale traveling ionospheric disturbances (MSTIDs) associated with atmospheric gravity waves (AGWs) using observations from the Blackstone SuperDARN radar. These observations will then be used in conjunction with geomagnetic data to determine the source of the observed MSTIDs.

Chapter 4 extends the work of Chapter 3 by using multiple radars distributed across North America at both high latitudes and midlatitudes. The objective of Chapter 4 is to develop a climatology of high latitude and midlatitude AGW-MSTIDs and use these observations in conjunction with geomagnetic and polar atmospheric data to determine the source of the observed MSTIDs.

Chapter 5: Ionospheric Sounding with Amateur Radio Networks

1. Can crowd-sourced observations of amateur radio transmissions be used to detect ionospheric disturbances?

The objective of Chapter 5 is to demonstrate that crowd-sourced observations of amateur radio transmissions could potentially be useful to the fields of space weather and space science.

Chapter 6: Summary and Future Work

Finally, this dissertation concludes with Chapter 6 by presenting a summary of the findings and a discussion of directions for future research.

Proton Density	6.6 cm^{-3}
Electron Density	7.1 cm^{-3}
He ²⁺ Density	0.25 cm^{-3}
Flow Speed (nearly radial)	450 km s^{-1}
Proton Temperature	$1.2 \times 10^5 \text{ K}$
Electron Temperature	$1.4 \times 10^5 \text{ K}$
Magnetic Field (Induction)	$7 \times 10^{-9} \text{ T}$

Table 1.1: Typical solar wind properties observed near the orbit of the Earth. From *Hundhausen* [1995], used with permission.

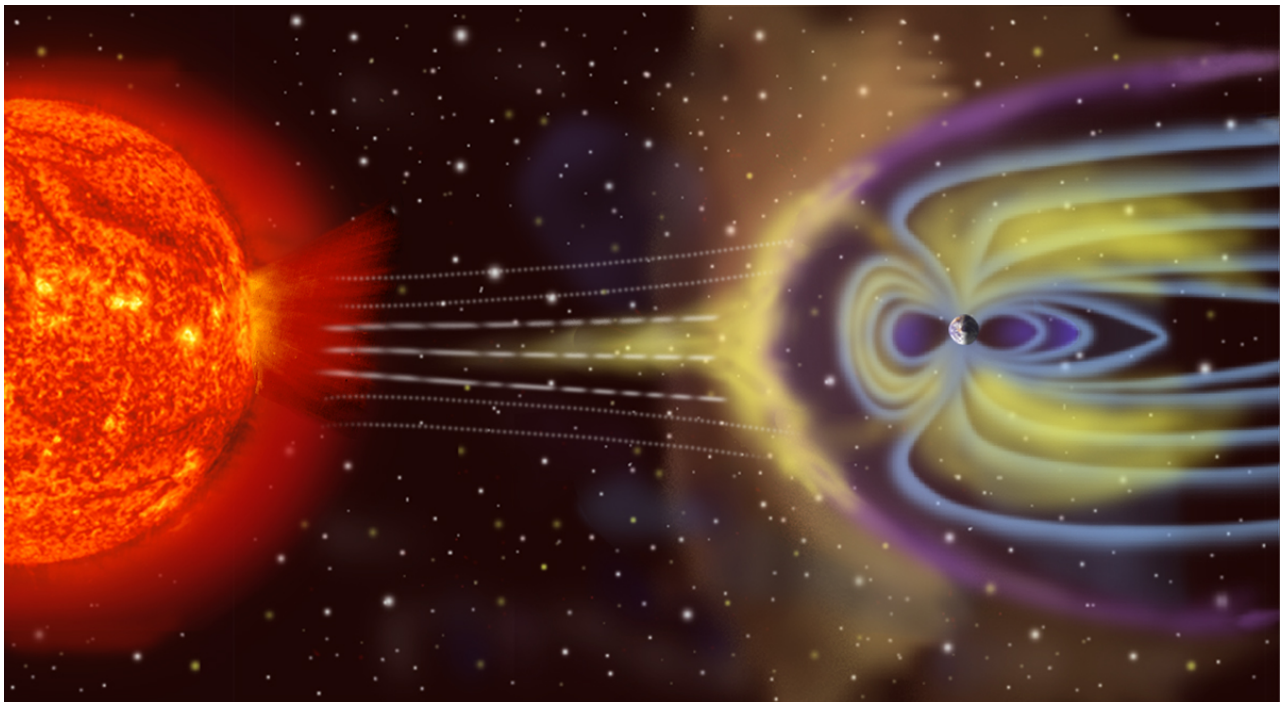


Figure 1.1: Artistic cartoon depicting the solar wind and the Earth's magnetosphere. Image credit: NASA.

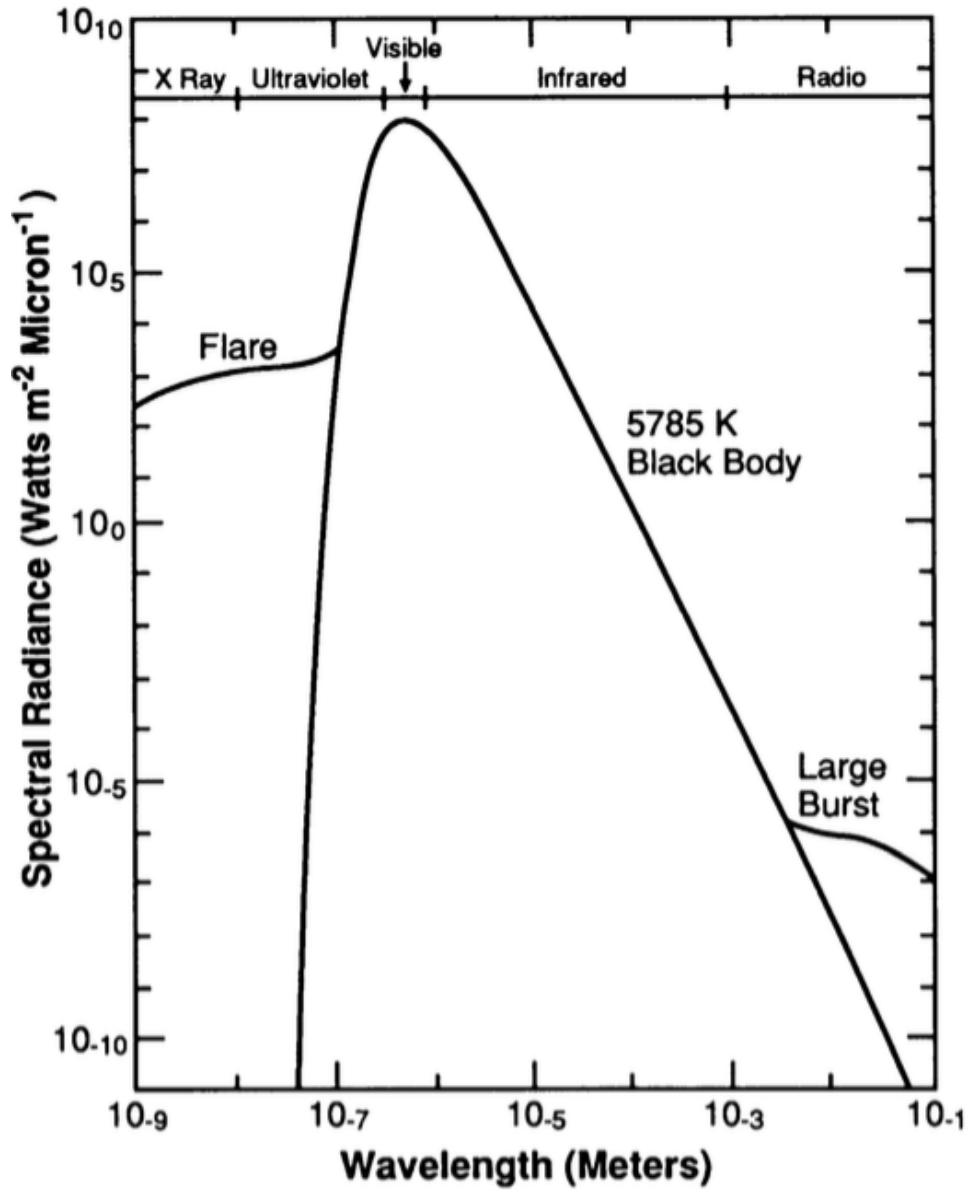


Figure 1.2: Spectral radiance of the surface of the Sun as a function of wavelength. From *Priest* [1995], used with permission.

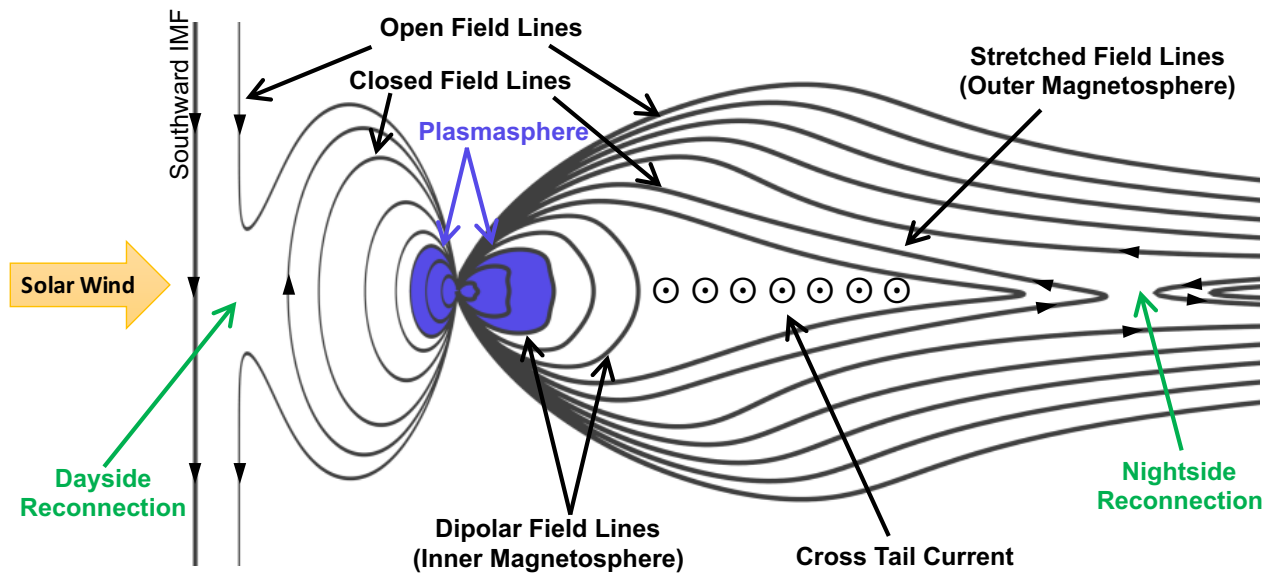


Figure 1.3: A depiction of the magnetosphere illustrating key magnetospheric processes and features. See Sections 1.2.2 for details.

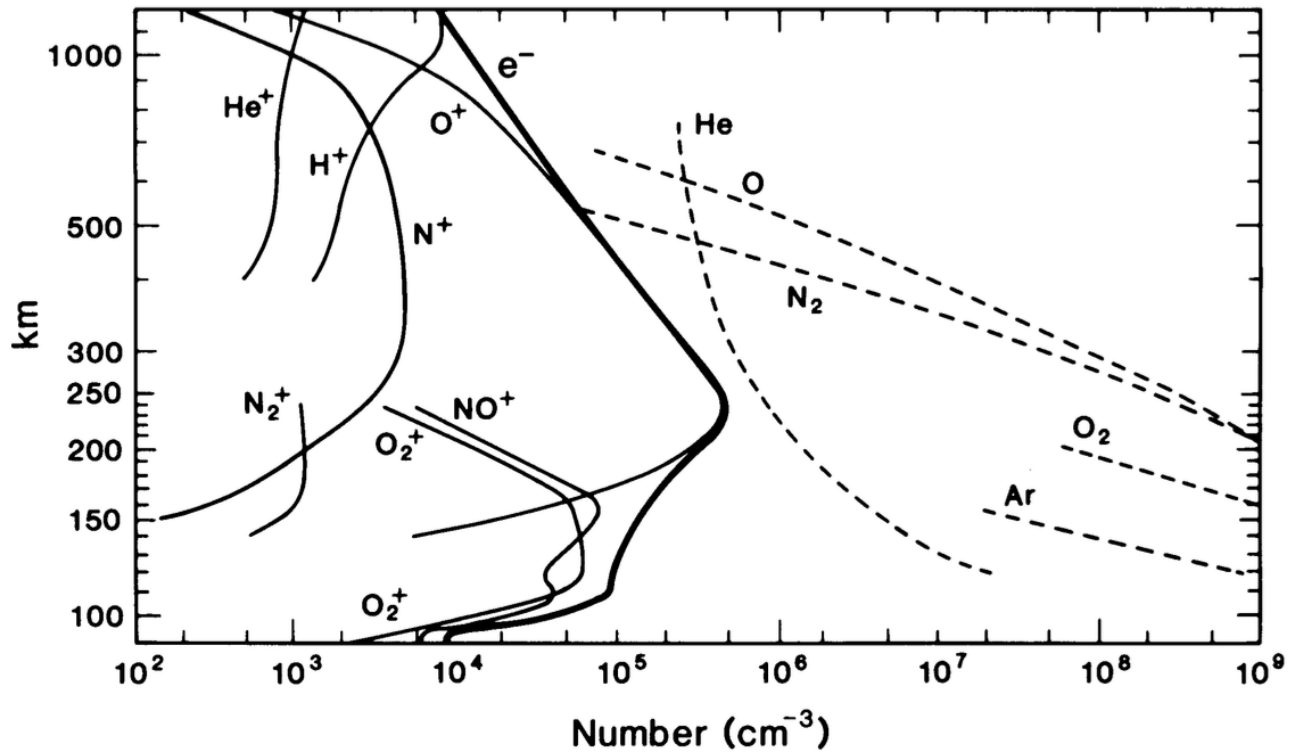


Figure 1.4: Daytime international quiet solar year (IQSY) ionospheric and atmospheric composition measurements based on mass spectrometer data. From *Luhmann* [1995] after *Johnson* [1969], used with permission.

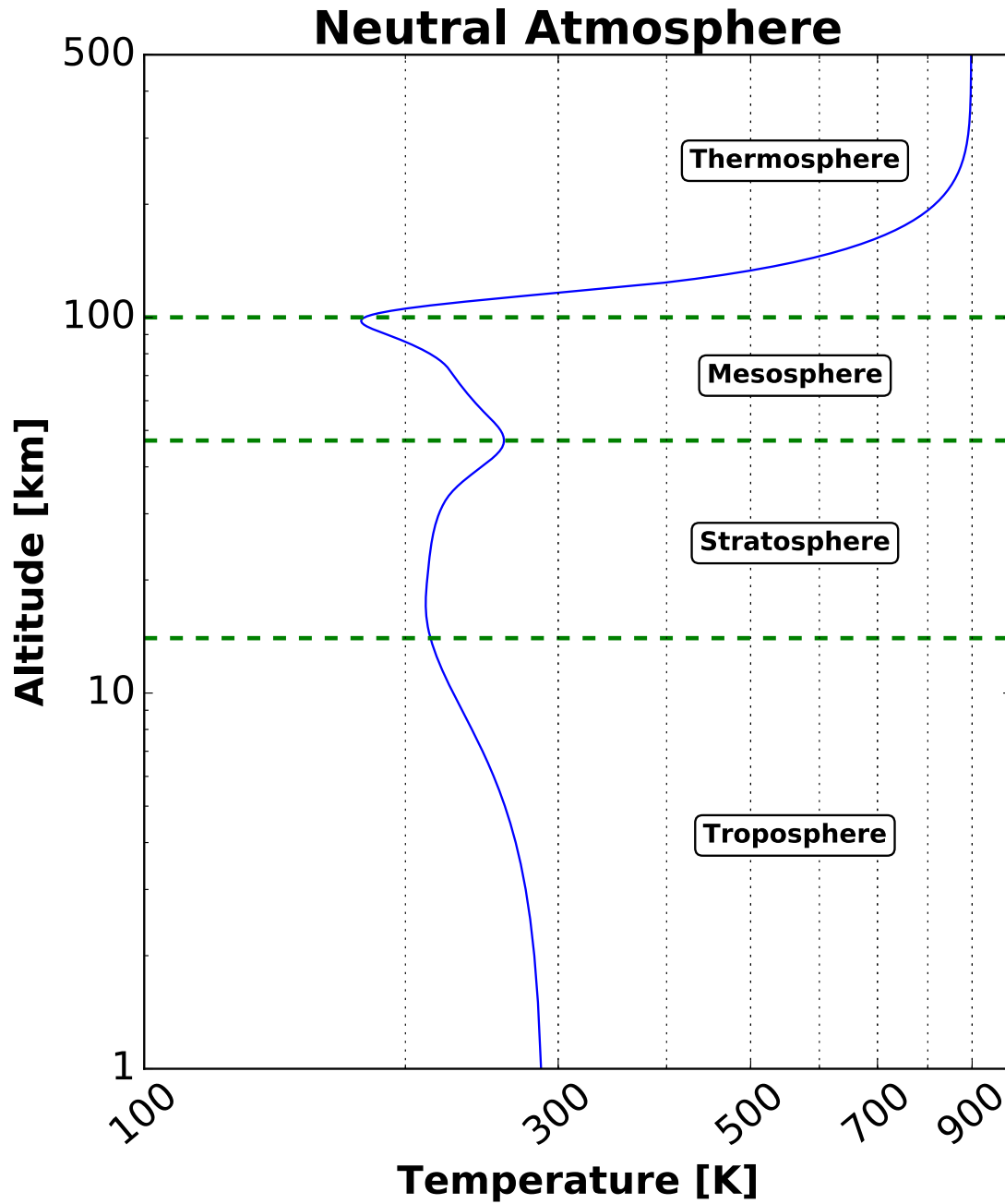


Figure 1.5: Example neutral atmospheric temperature profile generated using the MSIS model for 21 Jan 2013 1200 UT, 40°N, 80°W. Atmospheric regions are defined by the inflection points of the temperature profile.

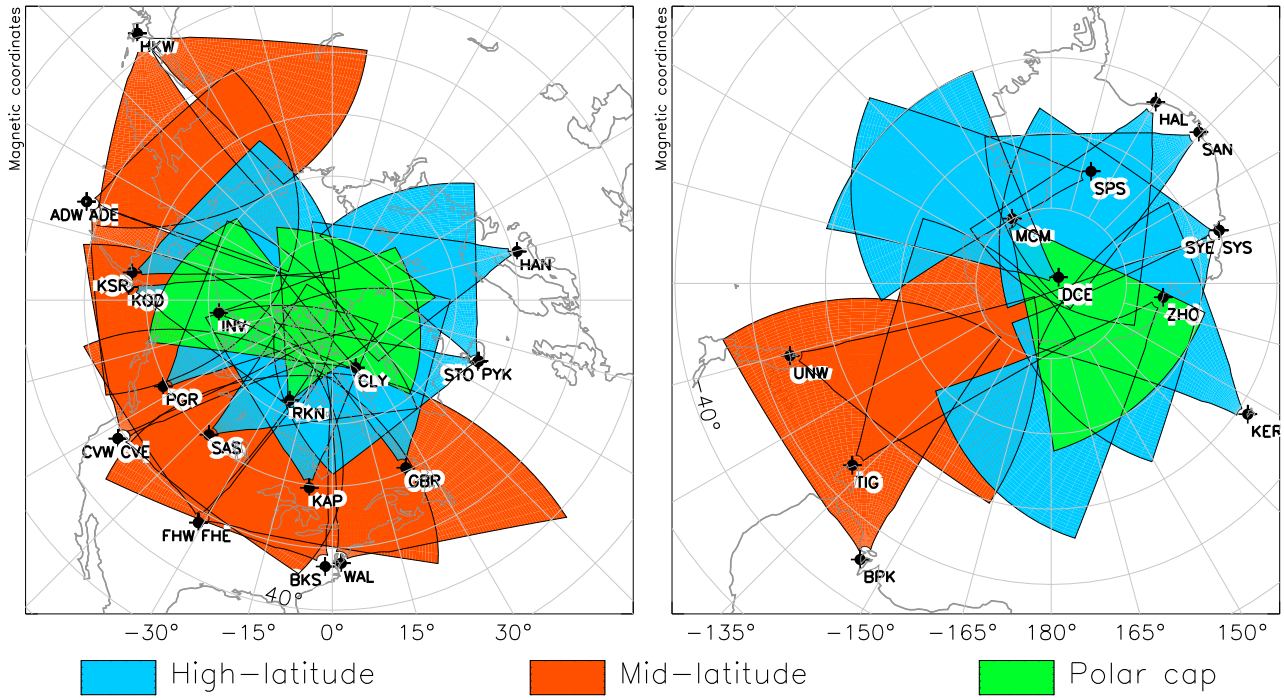


Figure 1.6: SuperDARN Network in March 2016.

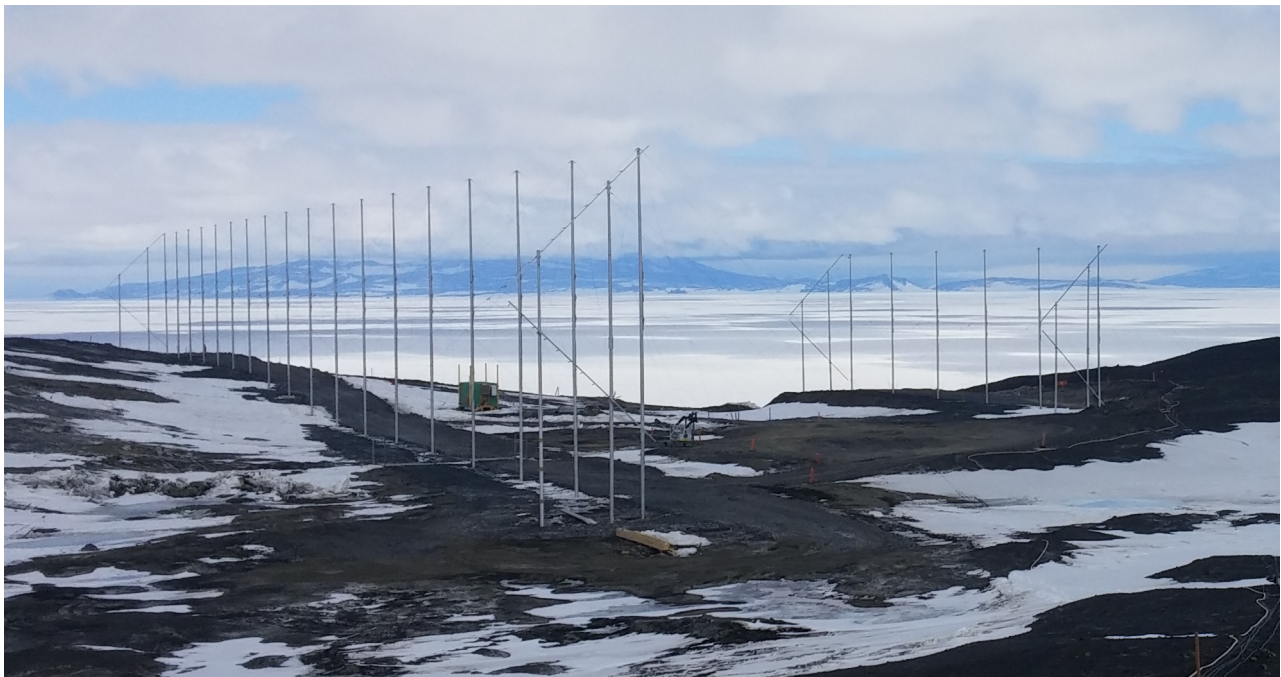


Figure 1.7: SuperDARN radar at McMurdo Station, Antarctica. The main linear phased array (16 antennas) is on the left, and the receive-only interferometer array (4 antennas) is on the right. A corner reflector attached to the back of each array directs radar energy in the desired direction. Photo: N. A. Frissell

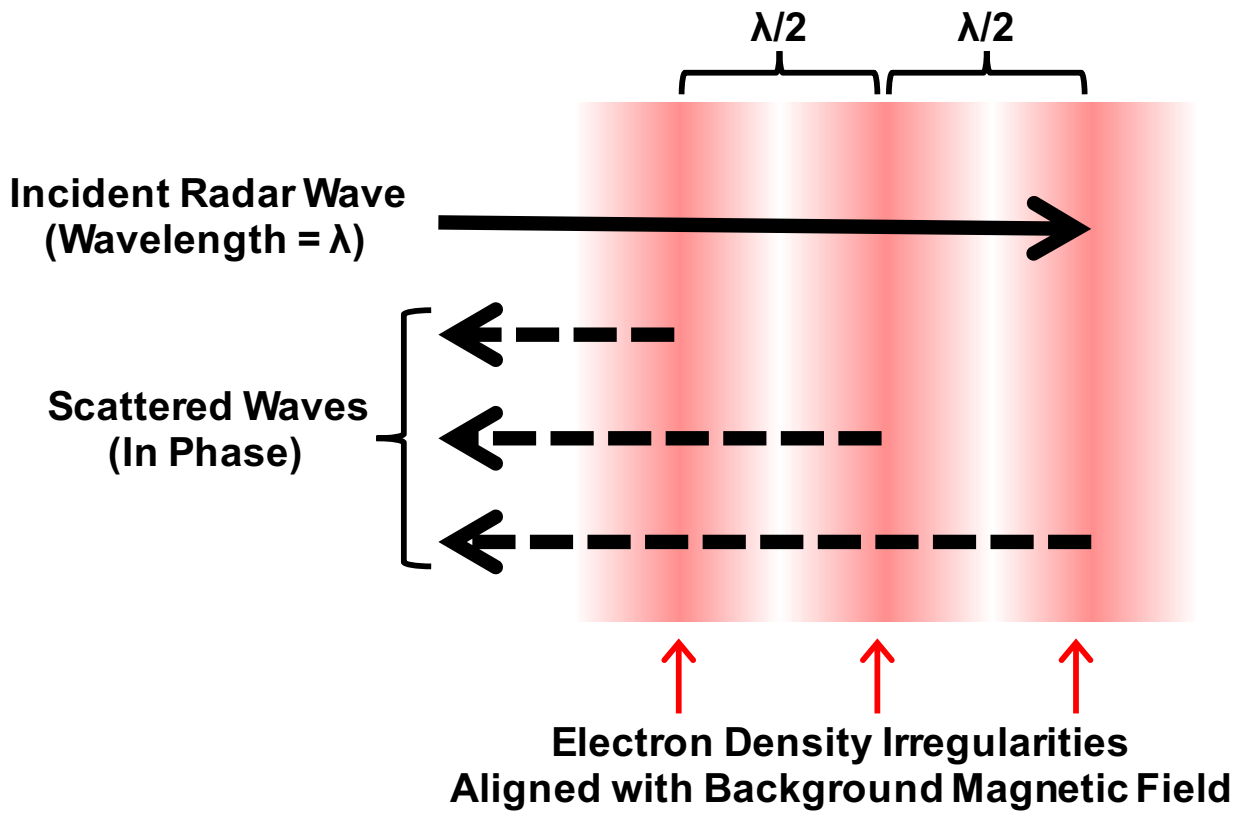


Figure 1.8: Illustration of coherent (Bragg) scattering of radar signals from ionospheric field aligned irregularities.

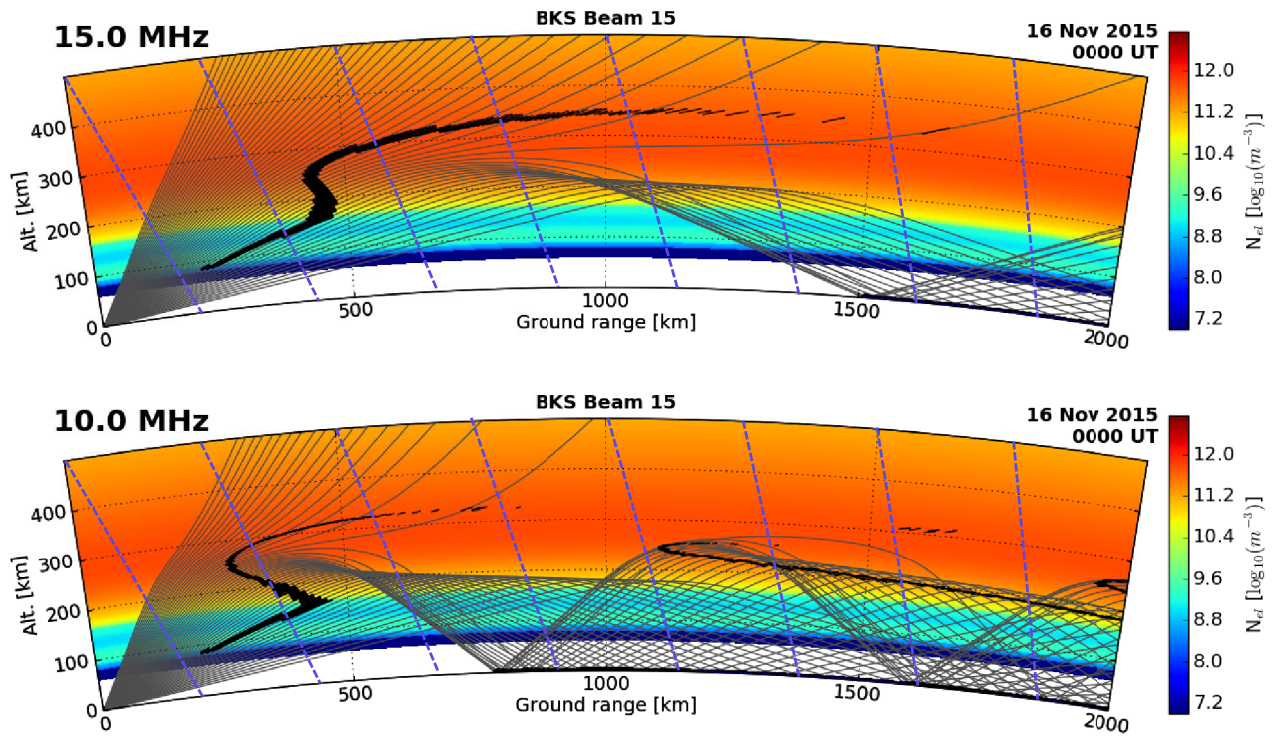


Figure 1.9: Raytrace of Blackstone SuperDARN radar at 10 MHz (bottom) and 15 MHz (top) using a procedure developed by *de Larquier et al.* [2013]. The gray curves represent radars rays, the background colors indicate IRI model electron densities [*Bilitza et al.*, 2011], the dashed purple lines show magnetic field inclination, and the thick black curve shows where the radar rays are orthogonal to the magnetic field within 1° .

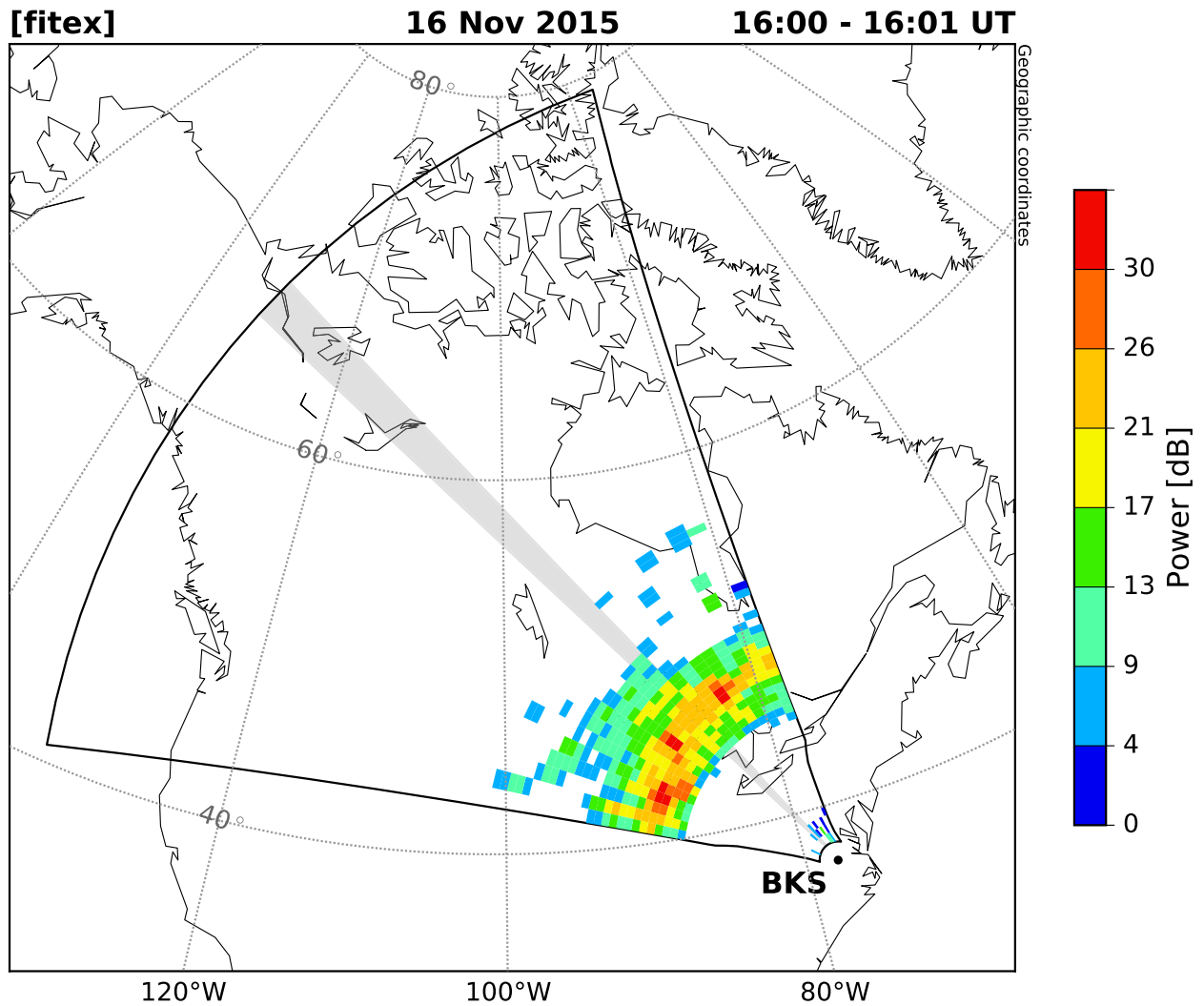


Figure 1.10: Scan plot of SNR/Power measurements made by the Blackstone, Virginia SuperDARN radar on 16 November 2015, 1600–1601 UT at 14.5 MHz. Beam 15 is shaded in gray. Wavefronts indicative of MSTIDs are visible in the ground scatter band.

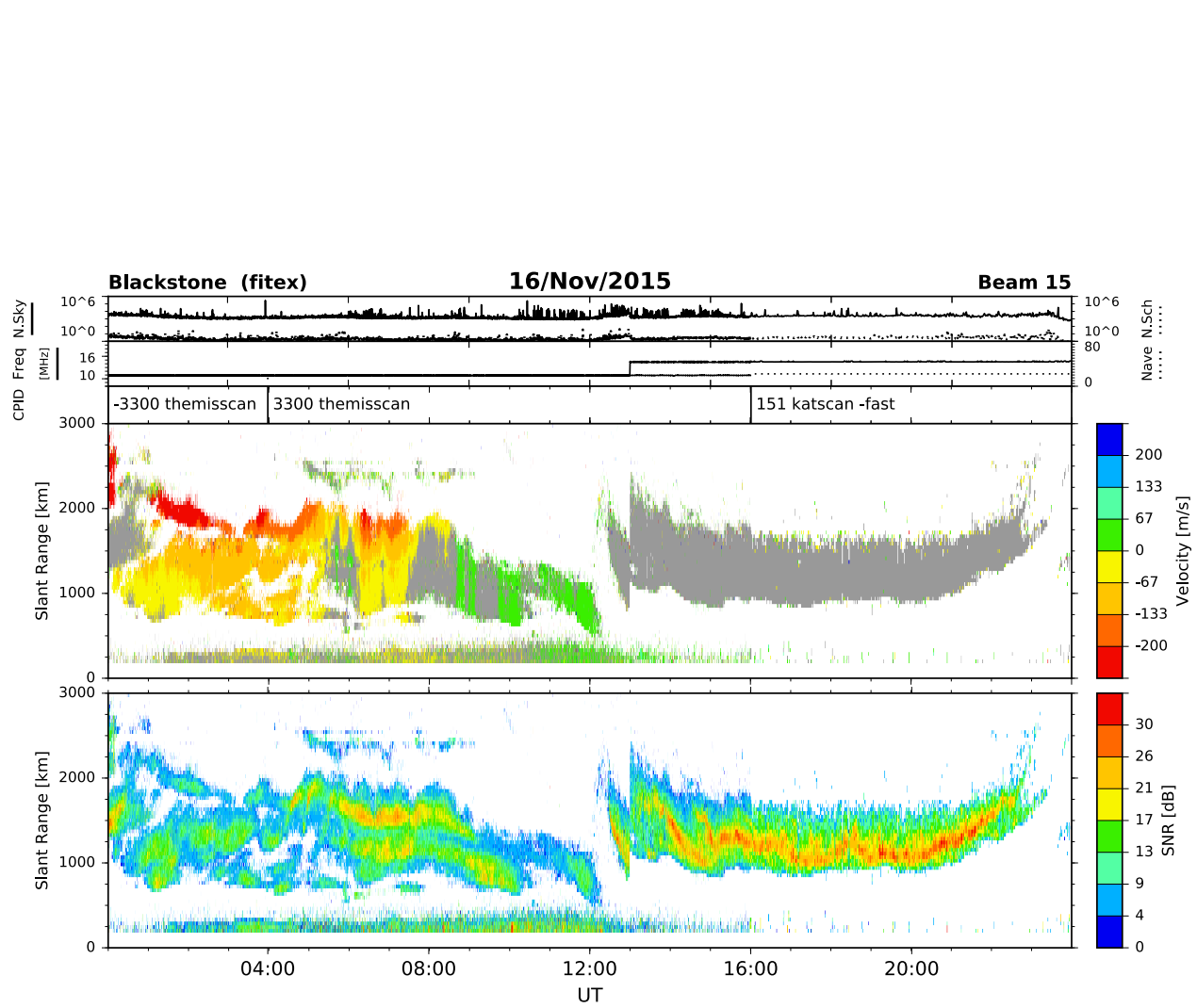


Figure 1.11: Range-Time-Intensity (RTI) plot of Doppler velocity and SNR measurements collected by the Blackstone, Virginia SuperDARN radar on 16 November 2015. Gray shading indicates measurements identified as ground scatter.

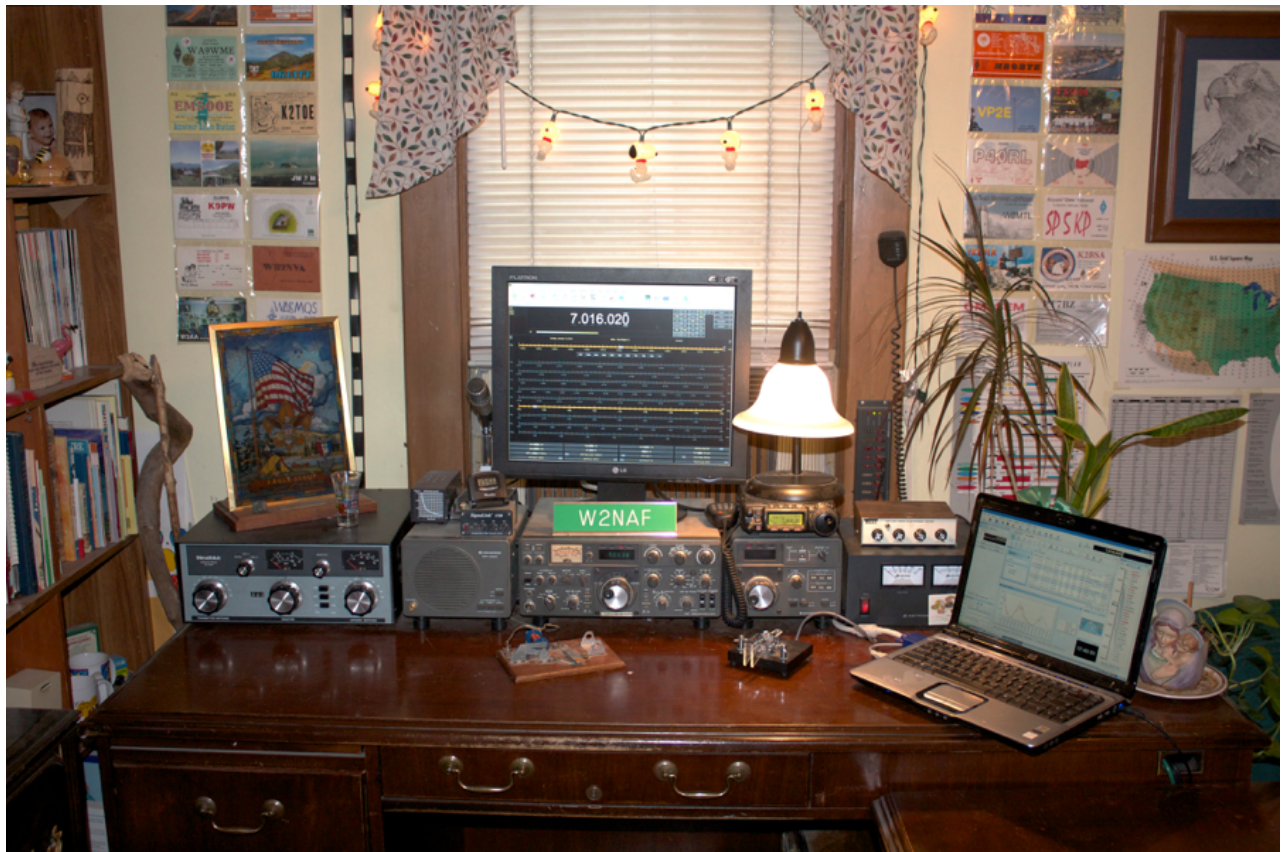


Figure 1.12: Example high frequency (HF) amateur radio station. Photo: N. A. Frissell

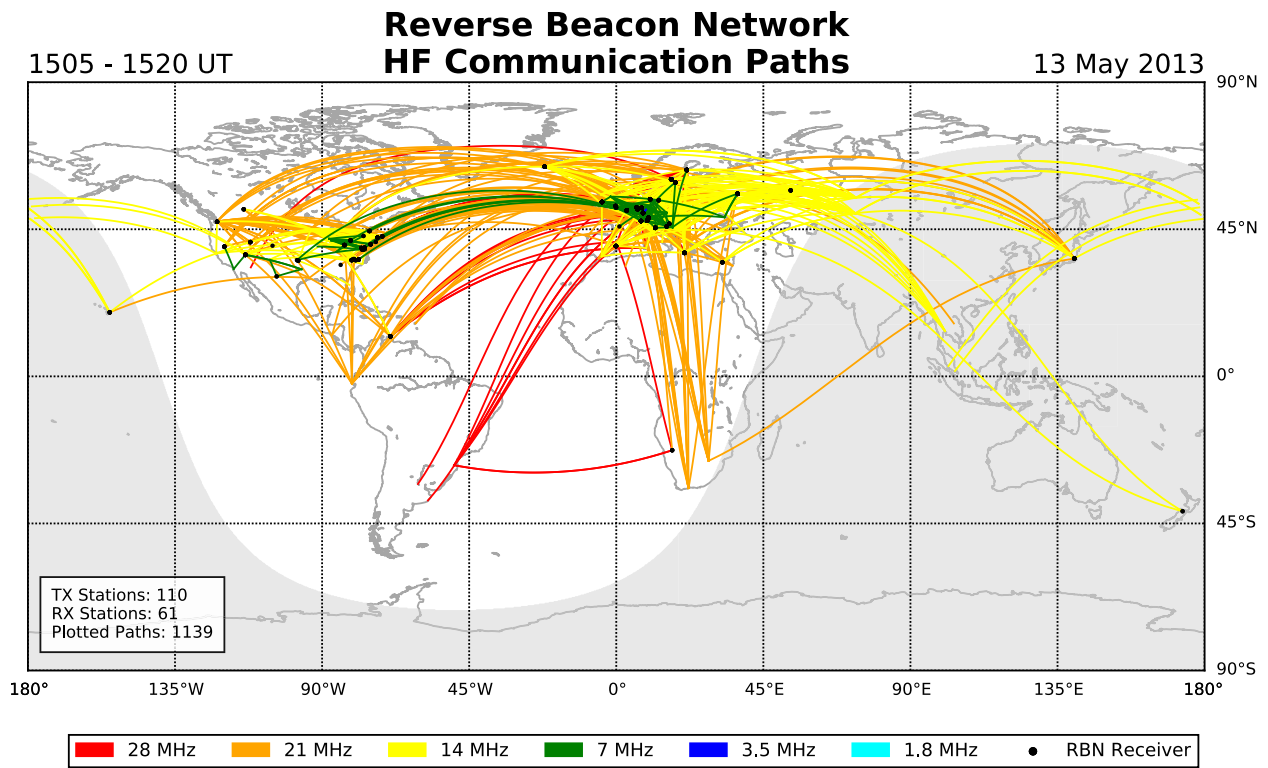


Figure 1.13: High frequency amateur radio communications links observed by the Reverse Beacon Network from 1505–1520 UT on 13 May 2013. From *Frissell et al.* [2014a], used with permission.

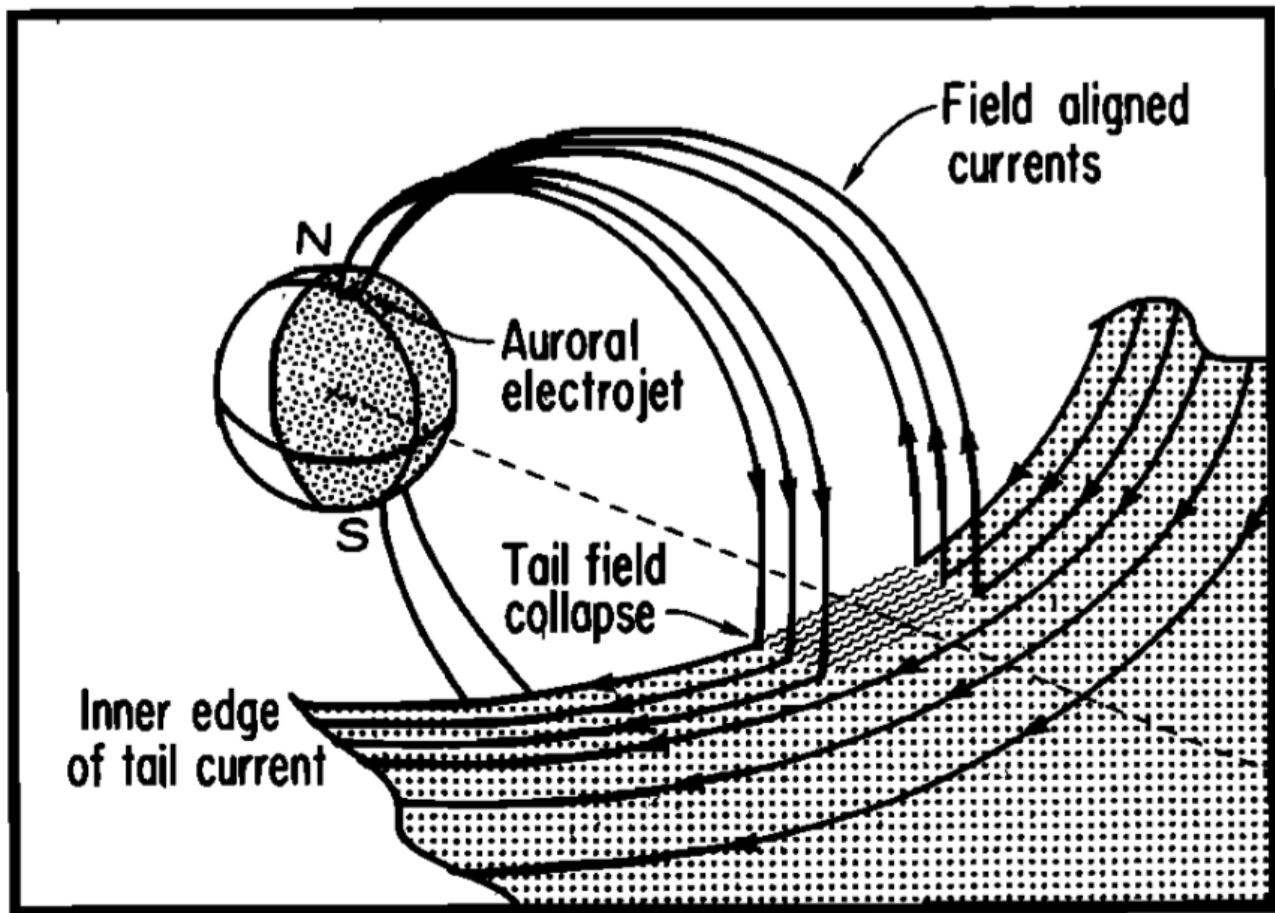


Figure 1.14: Illustration of the substorm current wedge formed from a diversion of the cross-tail current. From *McPherron et al.* [1973], used with permission.

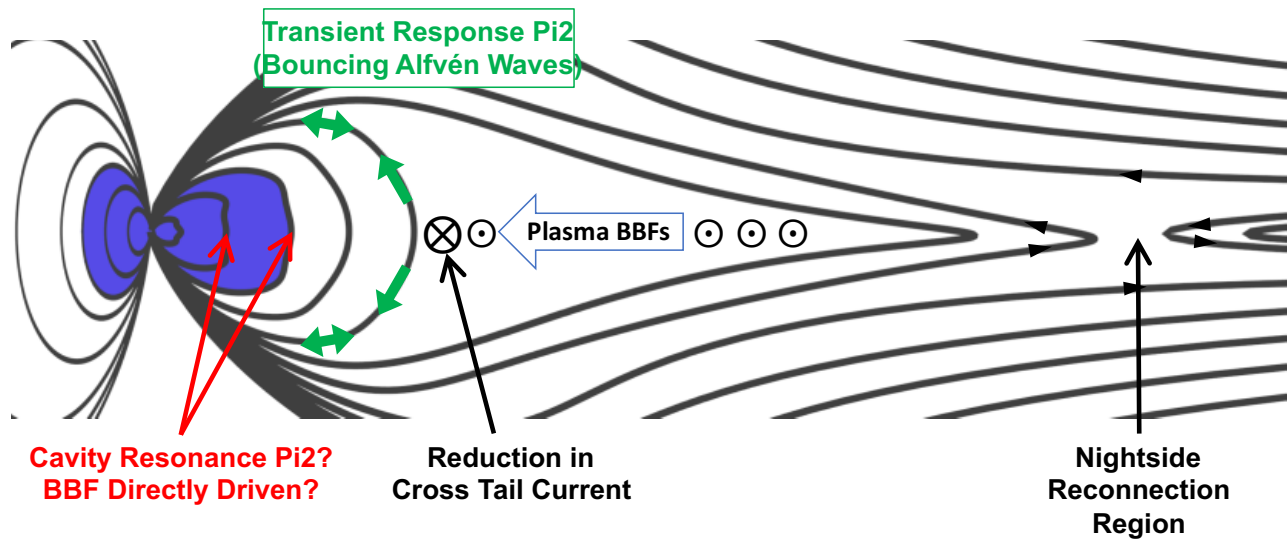


Figure 1.15: The magnetosphere at the onset of substorm expansion. Processes related to substorm current wedge formation (cross-tail current reduction) and the braking of bursty bulk flows against the nightside dipolar region are candidate energy sources for mid and low latitude Pi2 pulsations.

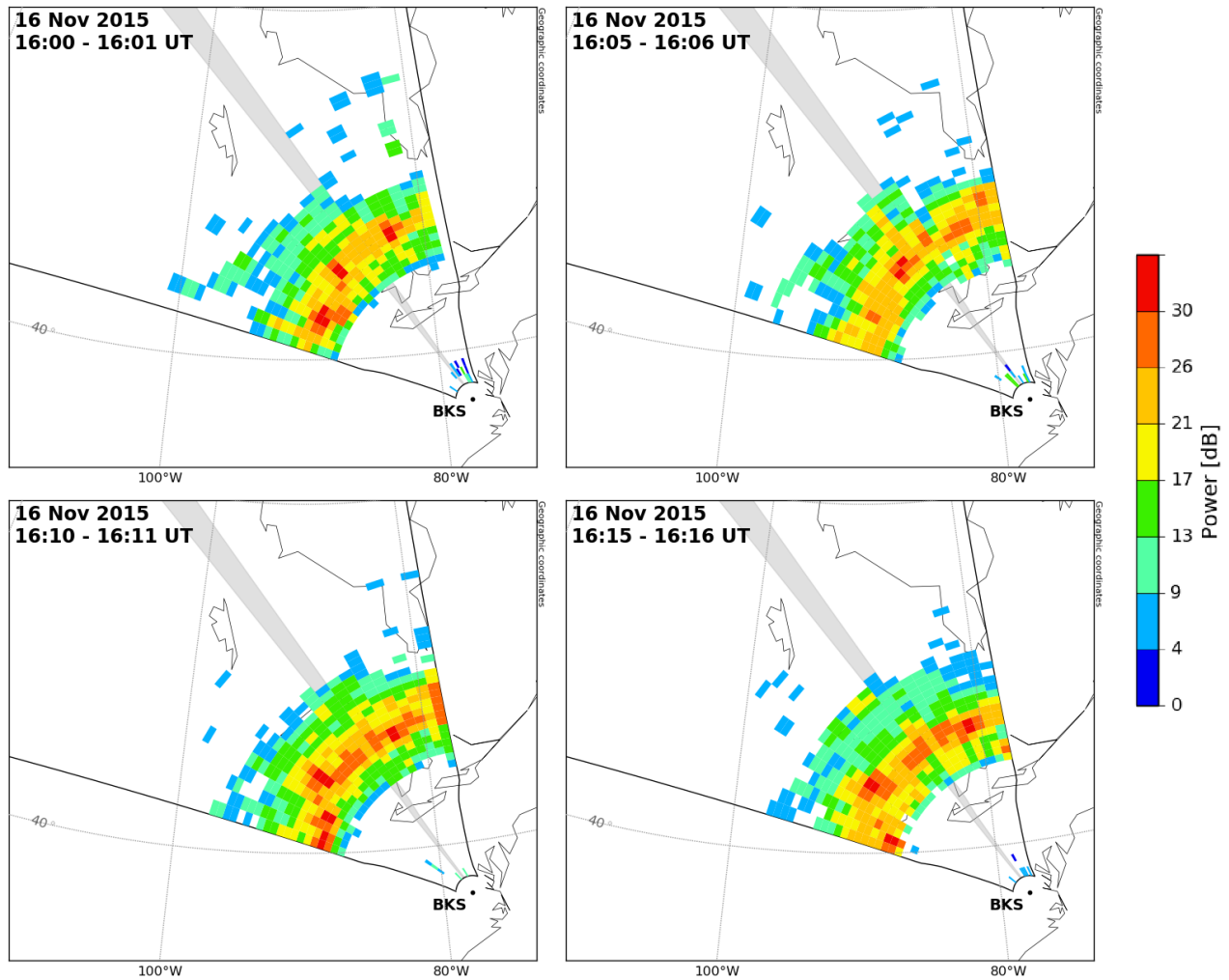


Figure 1.16: Four 1-minute scans of Blackstone SuperDARN power observations beginning at 1600 UT on 16 November 2015. Maps have successive 5 minute spacing. Beam 15 is shaded in gray. Wavefronts indicative of MSTIDs are visible in the ground scatter band and can be seen to move in range with time.

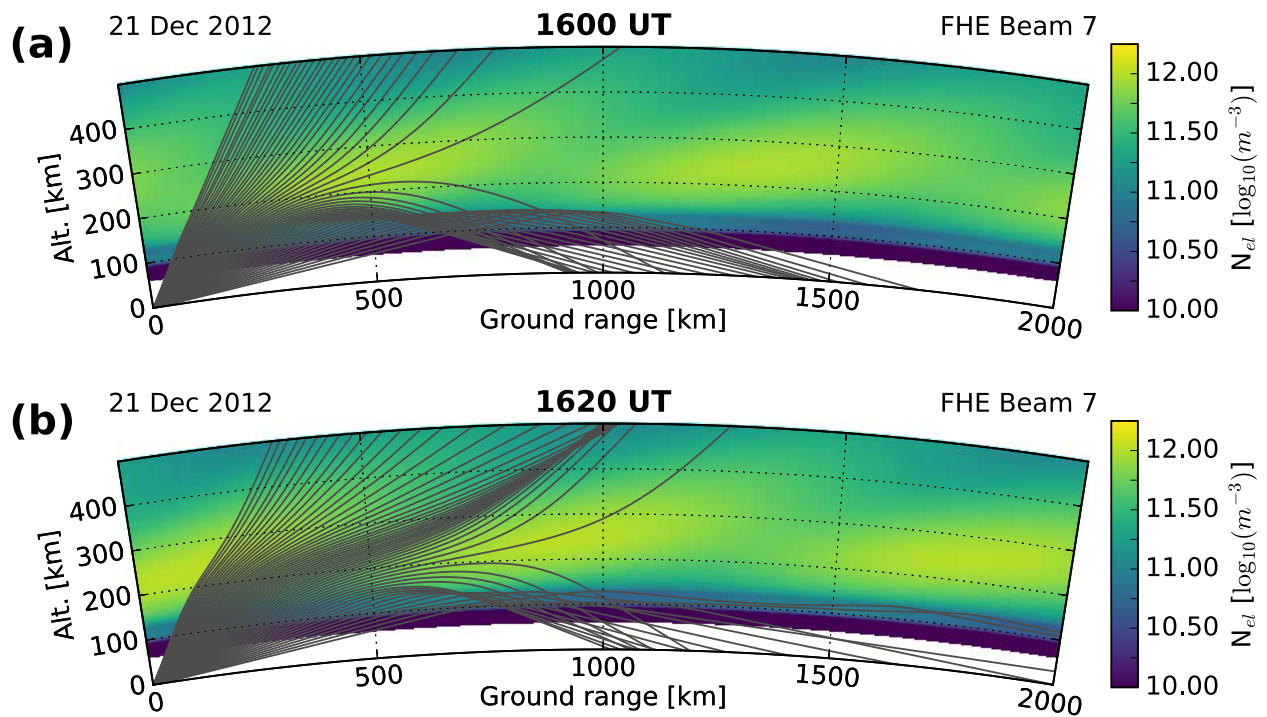


Figure 1.17: Raytrace of a SuperDARN radar operating at 14.5 MHz through the IRI perturbed with a model MSTID. The MSTID is modeled as a sinusoid with period $T = 40$ min and horizontal wavelength $\lambda_h = 450$ km. The top and bottom panels are separated by 20 minutes.

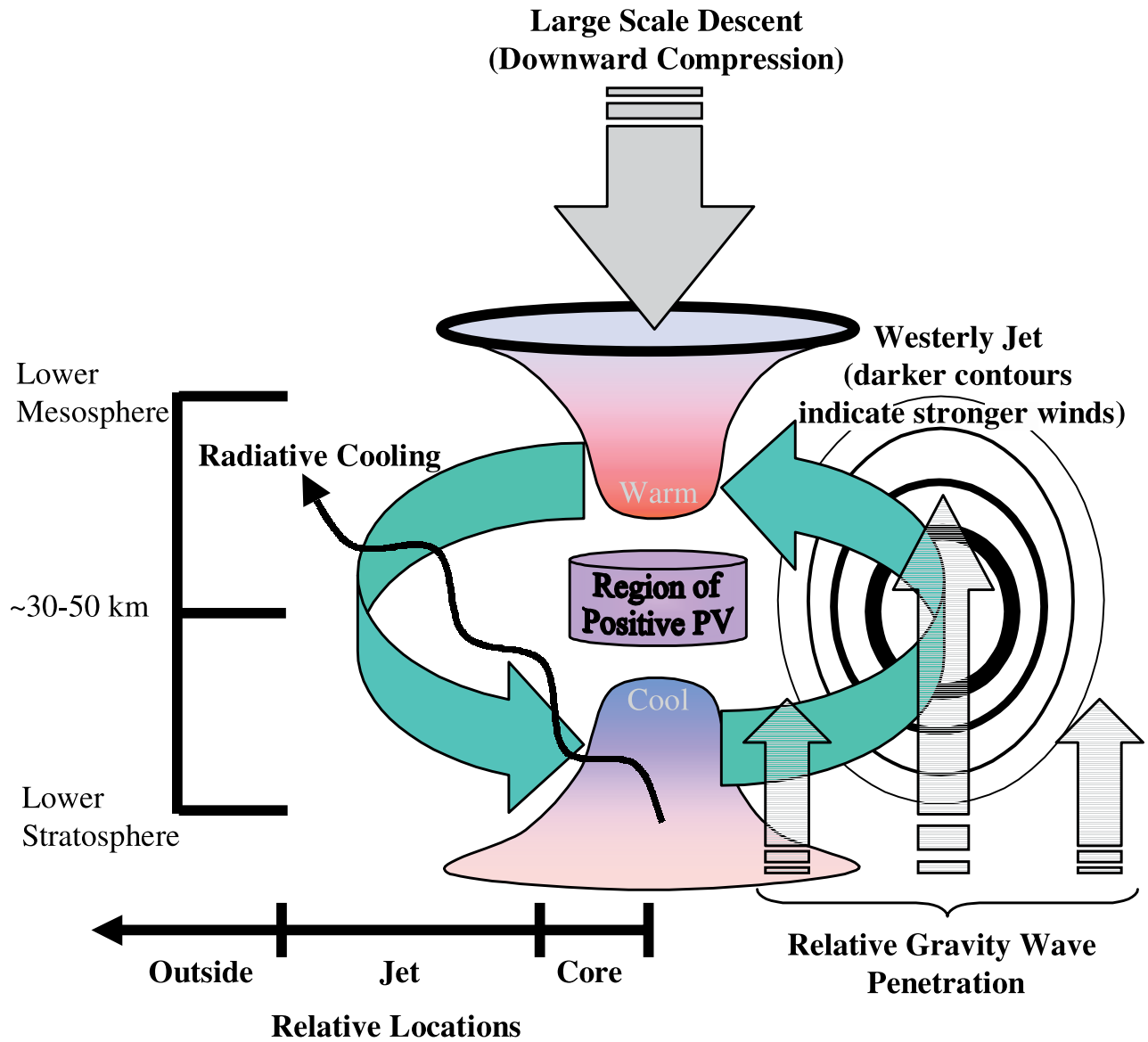


Figure 1.18: Schematic of nominal polar vortex configuration. Meridional temperature gradients and Coriolis effects create the high-speed flows in the jet. The jet can modulate atmospheric gravity waves propagating upward from below. From *Gerrard et al.* [2002], used with permission.

Chapter 2

First Radar Observations in the Vicinity of the Plasmapause of Pulsed Ionospheric Flows Generated by Bursty Bulk Flows

N. A. Frissell¹, J. B. H. Baker¹, J. M. Ruohoniemi¹, L. B. N. Clausen¹, Z. C. Kale², I. J. Rae², L. Kepko³, K. Oksavik⁴, R. A. Greenwald¹, and M. L. West⁵

¹Bradley Department of Electrical and Computer Engineering, Virginia Polytechnic Institute and State University, Blacksburg, Virginia, USA.

²Department of Physics, University of Alberta, Edmonton, AB, Canada.

³NASA Goddard Space Flight Center, Greenbelt, MD, USA.

⁴Department of Arctic Geophysics, The University Centre in Svalbard, Longyearbyen, Norway.

⁵Department of Mathematical Sciences, Montclair State University, Montclair, NJ, USA.

Published as:

Frissell, N. A., J. B. H. Baker, J. M. Ruohoniemi, L. B. N. Clausen, Z. C. Kale, I. J. Rae, L. Kepko, K. Oksavik, R. A. Greenwald, and M. L. West (2011), First radar observations in the vicinity of the plasmapause of pulsed ionospheric flows generated by bursty bulk flows, *Geophys. Res. Lett.*, 38, L01103, doi:10.1029/2010GL045857.

Abstract

Recent expansion of the SuperDARN network to mid-latitudes and the addition of a new high-time resolution mode provides new opportunities to observe mid-latitude ultra-low frequency waves and other ionospheric sub-auroral features at high temporal resolution. On 22 February 2008, the Blackstone SuperDARN radar and THEMIS ground magnetometers simultaneously observed substorm Pi2 pulsations. Similarities in measurements from the Blackstone radar and a magnetometer at Remus suggest a common generating mechanism. Cross-phase analysis of magnetometer data places these measurements at the ionospheric projection of the plasmopause, while fine spatial and temporal details of the radar data show evidence of field line compressions. About 1 min prior to ground Pi2 observation, 2 Earthward-moving Bursty Bulk Flows (BBFs) were observed by THEMIS probes D and E in the near-Earth plasma sheet. We conclude that the first 2 pulses of the Pi2s observed at Blackstone and Remus result from compressional energy generated by BBFs braking against the magnetospheric dipolar region.

2.1 Introduction

Pi2 refers to a class of ultra-low frequency (ULF) geomagnetic pulsations with an irregular waveform and a period of 40 - 150 s [*Jacobs et al.*, 1964]. They are thought to be generated by processes driven by current-carrying Alfvén waves or compressional waves produced during substorm onset [*Olson*, 1999]. Alfvén waves, which can be generated by a diversion of the cross-tail current during substorm current wedge (SCW) formation [*Baumjohann and Glassmeier*, 1984], are associated with high-latitude Pi2s. Compressional energy is thought to drive lower-latitude Pi2s, but *Olson* [1999] notes that the generating mechanism of compressional waves at substorm onset is unknown. *Fujita et al.* [2002] uses numerical modeling to show how SCW formation can generate a compressional impulse; *Kepko and Kivelson* [1999] and *Kepko et al.* [2001] suggest that such energy could be produced by the braking of Earthward-moving bursty bulk flows (BBFs) against the magnetospheric dipolar region due to a pressure gradient. BBFs are high speed, convective plasma flow bursts found in the inner plasma sheet thought to be caused by transient reconnection in the magnetotail [*Sergeev et al.*, 1992; *Angelopoulos et al.*, 1994]. Two mechanisms have been suggested for Pi2 generation from this compressional energy. The cavity mode resonance model (CMR) suggests that standing waves are excited in the plasmaspheric cavity [*Takahashi et al.*, 2001; *Nosé*, 2010], while the direct response BBF model (DR-BBF) suggests ground instruments directly sense compressional waves generated by BBF braking [*Kepko and Kivelson*, 1999; *Kepko et al.*, 2001]. In CMR, Pi2 period depends on plasmaspheric parameters; in DR-BBF, it depends on the inter-BBF period. *Kepko and Kivelson* [1999] and *Kepko et al.* [2001] found events that support DR-BBF; however, the studies do not show this conclusively. We present a case study using radar, ground magnetometer (GMAG), and satellite data that gives clear evidence of a ground Pi2 resulting from compressional energy generated by BBFs braking against the magnetospheric dipolar region.

The Blackstone radar (BKS) (37.10°N, 77.95°W) began operation in February 2008 as part of an effort to expand SuperDARN [*Chisham et al.*, 2009, and references therein] radar capabilities to the mid-latitude region. SuperDARN range resolution is 45 km, which corresponds to a 0.3° latitudinal resolution around 55°N magnetic latitude. The radar measures the line-of-sight (LOS) component of the $\mathbf{E} \times \mathbf{B}$ drift velocity of F region plasma when decameter-scale ionization irregularities are present and so can detect the electric field component of ionospheric pulsations. Previous studies of mid-latitude pulsations with SuperDARN radar techniques include *Gjerloev et al.* [2007] and *Greenwald et al.* [2008].

The NASA THEMIS mission consists of ground based observatories (GBOs) [*Mende et al.*, 2008] spread across North America and five identical satellites in highly elliptical orbits [*Angelopoulos*, 2008]. Each GBO consists of an all-sky imager and a fluxgate GMAG capable of detecting perturbations in the magnetic field that represent the integrated effects of ionospheric currents flowing on spatial scales of hundreds of kilometers.

2.2 Observations

We present an isolated substorm after a period of extended geomagnetic quiet conditions. On 22 February 2008 at 0436 UT, the auroral electrojet (AE) index rose from 25 to 175 nT over a 25 min period, and had been steady at 25 nT for 2 hr prior. The solar wind interplanetary magnetic field (SW IMF) B_z at the nose of the Earth's bow shock from the OMNI database [*King and Papitashvili*, 2006] turned southward at 0415 UT and varied between -2 and +1 nT until 0500 UT. During this interval the SW velocity v_x was ~ 490 km s^{-1} and the proton density was ~ 3.0 cm^{-3} . *Liu et al.* [2009] conducted a study of associated high-latitude phenomena.

Figure 2.1 is an AACGM [*Baker and Wing*, 1989] map of the 22 February event. Brown

asterisks indicate the locations of THEMIS GBOs. At 0436 UT, the Eastern portion of the GBO network was centered around midnight magnetic local time (MLT), allowing for good coverage of substorm activity. Beginning at 0436 UT, Pi2s were observed by GMAGs at all GBOs shown in Figure 2.1. Figure 2.2e shows the magnetogram from RMUS. Pi2 signatures (not shown) from other midlatitude THEMIS GBOs are similar, although a longitudinally dependent phase shift in nightside Pi2s can be observed. Pi2s were also seen by southern hemisphere magnetometers in the SAMBA (South American B-Field Array) chain and dayside magnetometers in the STEP 210 chain [Yumoto and C. P. M. N. Group, 2001]. B_x component magnetograms (not shown) from STEP 210 stations at Rikubetsu (37.29°N, 144.71°W AACGM, 1351 MLT) and Kototabang (16.32°N, 131.82°W AACGM, 1443 MLT) reveal Pi2s that are simultaneous and in-phase with RMUS B_x , although one-tenth the amplitude. Optical observations were limited due to generally cloudy conditions. However, white-light flux from Gillam (GILL) shows a sharp increase starting at 0436 UT [Liu et al., 2009]. Figure 2.1 also shows the magnetic footpoints of THEMIS D and E (THM-D,E) as determined by the T96 magnetic field model [Tsyganenko, 1996]. At 0436 UT, these probes were located at $(-10.9, 3.3, -2.3)$ and $(-10.2, 4.1, -2.1)$ R_E GSM, respectively, and were within $0.20 R_E$ of the neutral sheet.

An estimate of the auroral oval location for $K_p = 1$ [Holzworth and Meng, 1975] is shown in Figure 2.1. Measurements from the Total Energy Detector (TED) instrument on the NOAA POES satellite [Evans and Greer, 2006] have been overlaid and provide reasonable agreement. Also shown are the longitudinal estimates of the upward and downward field aligned currents (FACs) [Liu et al., 2009], as well as the position of the westward electrojet. Using a cross-phase analysis technique developed by Waters et al. [1991], we estimate the ionospheric projection of the plasmopause to be located between $L = 3 - 3.71$ ($54^\circ - 58^\circ$ AACGM latitude), as indicated by the region between the blue dashed lines near the bottom

of the map.

BKS LOS velocity measurements are shown in Figure 2.1 between 2200 and 0000 MLT and between 50° to 60° AACGM latitude. These velocities correspond to a 2 min scan over 16 beams beginning at 0444 UT. The thick dashed line indicates the location of the THEMIS mode “camping” beam, which provides 6 s resolution by interleaving camping beam measurements between those of normal beams. It can be seen that the BKS measurements are located at the ionospheric projection of the plasmopause in the pre-midnight subauroral region within a longitudinal sector defined by the SCW FACs.

Figure 2.2 presents time series data from the BKS radar, the RMUS GMAG, and THM-D and E. Both Figures 2.2a and 2.2b show range-time plots of BKS plasma velocity data from 54° to 58° AACGM latitude. Figure 2.2b shows data from the 6 s resolution camping beam while Figure 2.2a is from an adjacent 2 min resolution beam. The camping beam data of Figure 2.2b reveals fine structure in time and space that cannot be seen in Figure 2.2a, including ULF velocity pulsations with a latitudinal saw-tooth structure.

Figures 2.2c and 2.2d compare measurements from the BKS camping beam at range gate 21 (54.79°N , 12.49°W AACGM) with data from RMUS located at (54.65°N , 12.64°W AACGM). The data from RMUS have been average subtracted and rotated into the radar LOS look direction. Figure 2.2e shows the 3-component RMUS data for comparison. Many similarities can be seen when comparing the BKS data to the RMUS data, most notably in the waveforms of the Pi2 pulsations that begin ~ 0436 UT. The onset of the Pi2 in both the BKS and RMUS data correspond in time within one wave period to the auroral brightening at GILL and the observed AE enhancement.

Differences in observations allow the data sets to complement each other. In Figure 2.2e, the RMUS GMAG provides information about large scale current systems and 3-dimensional

measurements of the magnetic field. In Figures 2.2b and 2.2c, the radar provides localized measurements of the ionospheric electric field that contain significant spatial and temporal detail.

About 1 min prior to ground observations of Pi2s, THM-D and E observed BBFs. Figure 2.2f shows ion velocities measured by the Electrostatic Analyzers (ESA) [McFadden *et al.*, 2008] on both THM-D and E. Two BBFs corresponding to Earthward-moving velocity pulses can be seen in each data set.

2.3 Discussion

The resemblance of the BBF velocity pulses to the waveforms measured by RMUS and BKS is striking. In THM-D data, the time between BBF pulse peaks is ~ 135 s, while the time between the peaks of the first 2 pulses of both the RMUS and BKS data is ~ 138 s. The difference between these times is less than the time resolution of BKS, and the similarities in ground and space observations are suggestive of the DR-BBF model. We note that the peak of the second THM-E BBF occurs prior to that of THM-D. However, as the velocity amplitude of the second THM-D BBF is significantly higher than that of THM-E, we believe it is likely that the compression from the second THM-D BBF will extend that of THM-E. Therefore, it is the peak of the second THM-D BBF that is important for timing.

Figure 2.3 provides a detailed look at data first presented in Figure 2.2b. In Figure 2.3a, BKS beam 7 range gates 10 - 24 are averaged together in adjacent groups of 3 to create 5 velocity traces. Figure 2.3b is obtained by subtracting the mean background velocity from each trace. We note that Pi2s in B_x magnetograms (not shown) from THEMIS GBOs in Shawano (SWNO) (55.72°N , 17.62°W AACGM), Derby (DRBY) (54.99°N , 6.16°E AACGM), and RMUS are in phase, and thereby conclude that the phase relationships shown in Figure

2.3 depend only on latitude. Each trace corresponds to a different L-shell and represents the motion of different length field lines. We define coherence as identical velocities among traces after the removal of background velocities. Coherence should not be expected in nominal cases. Figure 2.3b reveals periods of both coherence and dispersion, as exemplified by the second pulsation. This coherence begins at 0440 UT (indicated by arrow) and continues until pulse maximum, which is marked as the beginning of the second dispersion. We interpret the coherence as a signature of compression by the second BBF, and the dispersion as a signature of system relaxation. During the relaxation, the highest latitude measurements change the slowest because they correspond to the movement of the longest field lines. From the second dispersion until the end of the presented interval, the traces exhibit little coherence as the forcing of the BBF has gone. Coherence and dispersion are also seen in the first pulse of Figure 2.3b; this corresponds to compression by the first BBF.

As an additional test, we estimated the signal transit time of the maxima of the first pulse from THM-D to the L-shell of the highest latitude BKS measurement. We first separated the signal path into 2 regions. In the first region, the BBF travels in a straight line at the initially measured velocity $v_x = 570.3 \text{ km s}^{-1}$ from THM-D at $-10.9 R_E$ to a braking region at $-10 R_E$ X-GSM [Birn *et al.*, 1999]. In the second region, we assumed energy was converted to a compressional wave traveling at the local Alfvén velocity (ranging from 270 to 3330 km s^{-1}) along the equatorial plane until the L-shell of the outermost BKS measurement at $-2.8 R_E$ X-GSM. The equatorial plane location and the magnetic field values for the Alfvén velocities came from the T96 model using disturbance storm time index $DST = 2.5 \text{ nT}$, SW dynamic pressure $p = 1.4 \text{ nPa}$, IMF $B_y = 3.5 \text{ nT GSM}$, and IMF $B_z = -0.5 \text{ nT GSM}$. Particle density was determined using THM-D measurements and a R^{-3} dependence from the center of the Earth [Clausen *et al.*, 2008]. This results in a total transit time of 80 s. The observed first pulsation maxima at THM-D occurred at 0437:14 UT while the corresponding first maxima

at BKS occurred at 0438:32 UT, giving an observed transit time of 78 s. This agrees well with our estimate.

We have shown that DR-BBF mechanisms drive the first 2 ground Pi2 pulses. It is possible these pulses provide energy that excites a CMR [Fujita *et al.*, 2002; Zhu and Kivelson, 1989]. This could account for the Pi2's global nature, the Pi2's continued ringing after the initial 2 pulses, and the simultaneity of the noon-midnight observations [Sutcliffe and Yumoto, 1989].

2.4 Conclusions

We have presented the first direct evidence of BBFs producing compressions at the plasma-pause. During an isolated substorm on 22 February 2008 at 0436 UT, Pi2s were observed simultaneously by the BKS SuperDARN radar and THEMIS GMAGs. Just over 1 min prior to observation of ground Pi2s, 2 Earthward-moving BBFs were observed by THM-D and E in the near-earth neutral sheet. Similarities in pulsations detected by the BKS radar and the RMUS GMAG suggest that a single source generated the Pi2s observed by these stations. Both stations were located in the pre-midnight sector of the sub-auroral region. Previously, these Pi2s could have been interpreted to be generated by the transient response SCW mechanism [Baumjohann and Glassmeier, 1984], but we find that the first 2 Pi2 pulses resulted from DR-BBF mechanisms. These compressions may also couple to a CMR. This conclusion is based on similarities of the BBF waveforms to the first 2 pulses observed by BKS and RMUS, a propagation timing analysis, and the prior work of Kepko and Kivelson [1999], and Kepko *et al.* [2001]. Additional evidence is derived from further study of the BKS radar data, which shows a coherence in the velocity perturbation with latitude as the pulses rise to maximum, but a dispersion in the velocities as the system relaxes. Cross-phase analysis of GMAG data places these measurements at the ionospheric projection of the plasmopause. Therefore, we

interpret these latitudinal variations in the radar data as evidence of compressions at the plasmopause.

2.5 Acknowledgments

Support for this research and funding for the construction of the Blackstone SuperDARN radar is provided by NSF grants ATM-0849031 and ATM-0946900. K. Oksavik thanks the Research Council of Norway for financial support. K_p and AE indices were obtained from the WDC in Kyoto. We acknowledge NASA contract NAS5-02099 and V. Angelopoulos for use of data from the THEMIS Mission. Specifically C. W. Carlson and J. P. McFadden for use of ESA data, S. Mende, C. T. Russell, and I. Mann for use of GMAG data, and the CSA for support of the CARISMA network. We thank J. Green for providing data from the NOAA/POES TED instrument, and E. Zesta for SAMBA GMAG data. STEP 210 GMAG data was copied from the Solar-Terrestrial Environment Laboratory, Nagoya University. SW and IMF data was obtained from the CDAWeb OMNI database by J. H. King and N. Papitashvili. Satellite positions and magnetic footprints were obtained with the TIPSOD program by NASA GSFC SSC.

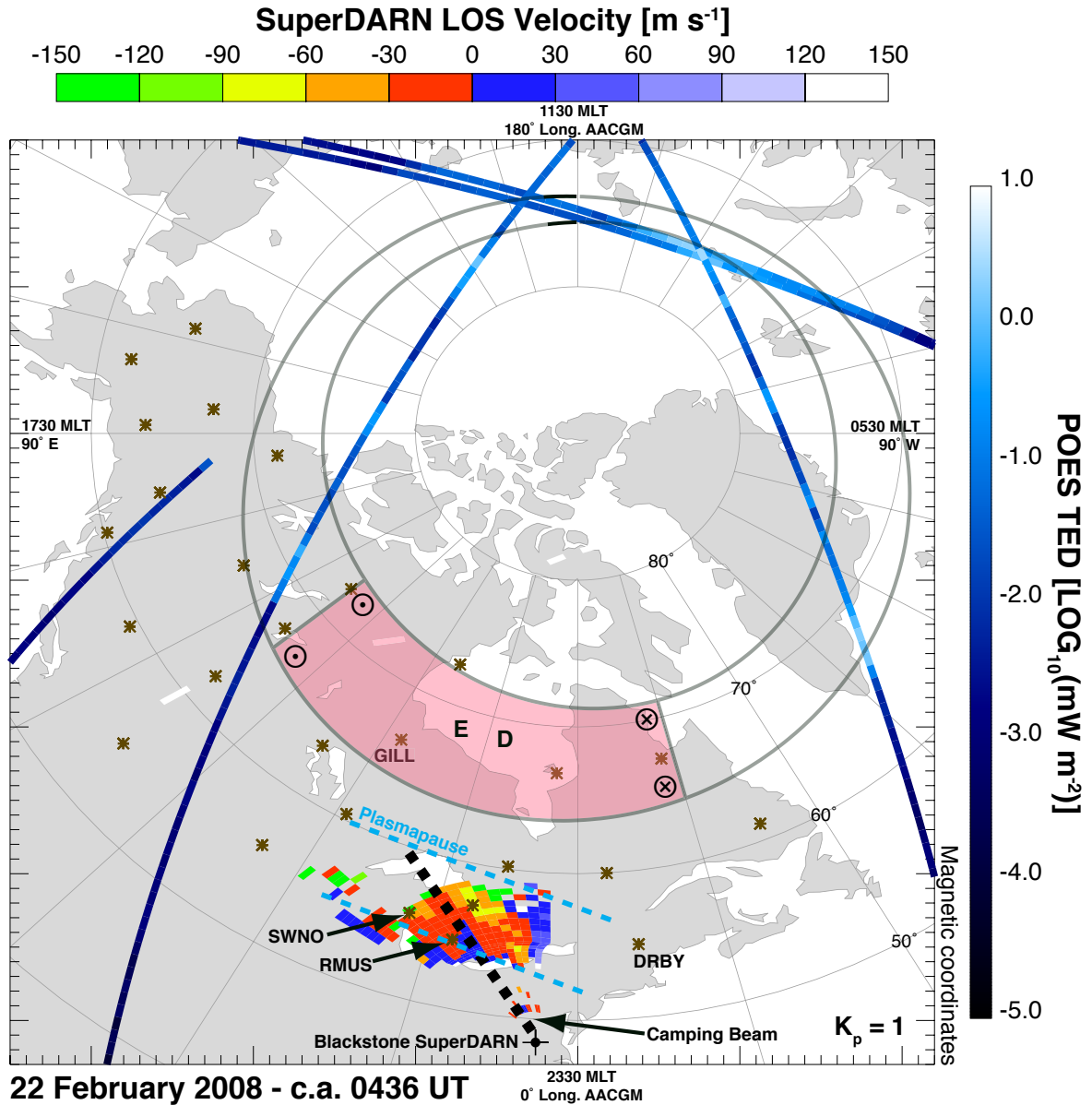


Figure 2.1: AACGM map for the substorm on 22 February 2008 at 0436 UT. The map includes LOS BKS velocity data at 0444-0446 UT (green-red-blue colors), POES auroral precipitation flux at 0430-0530 UT (blue colors), locations of GBOs (brown asterisks), footprints of two THEMIS probes (letters D and E), estimates of the auroral oval (gray circles), westward electrojet (pink color), SCW FACs (encircled dots), and plasmopause (between blue dashed lines).

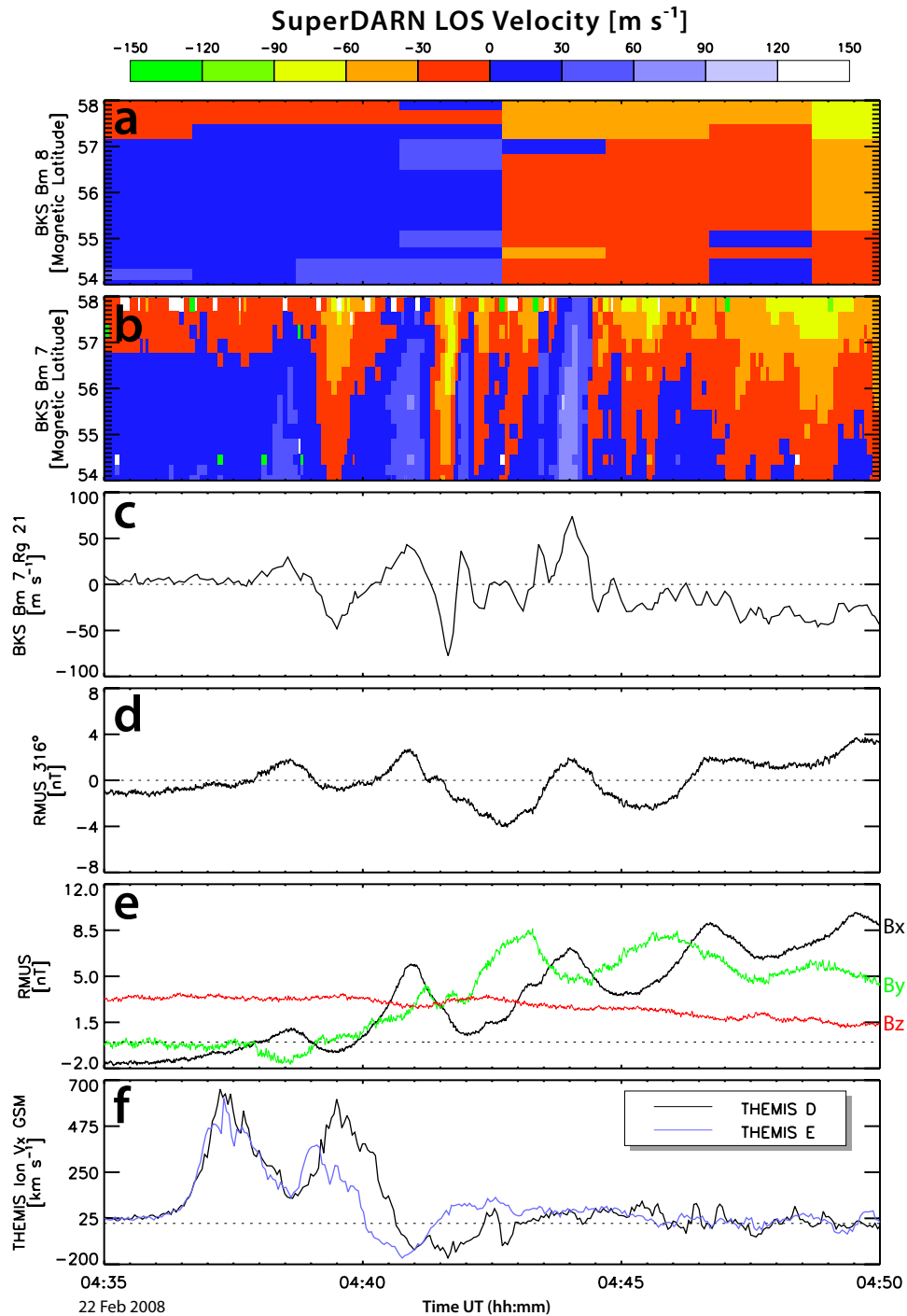


Figure 2.2: Time series data for a substorm on 22 February 2008. (a) BKS radar LOS velocity data from beam 8 with 2 min resolution. (b) BKS beam 7 shows Pi2s that cannot be observed in beam 8. (c) LOS velocity data from BKS beam 7, range gate 21. (d) RMUS GMAG component rotated into the LOS direction of the radar, baseline removed. (e) 3-component RMUS data, baseline removed. (f) Ion velocity data from THM-D and E.

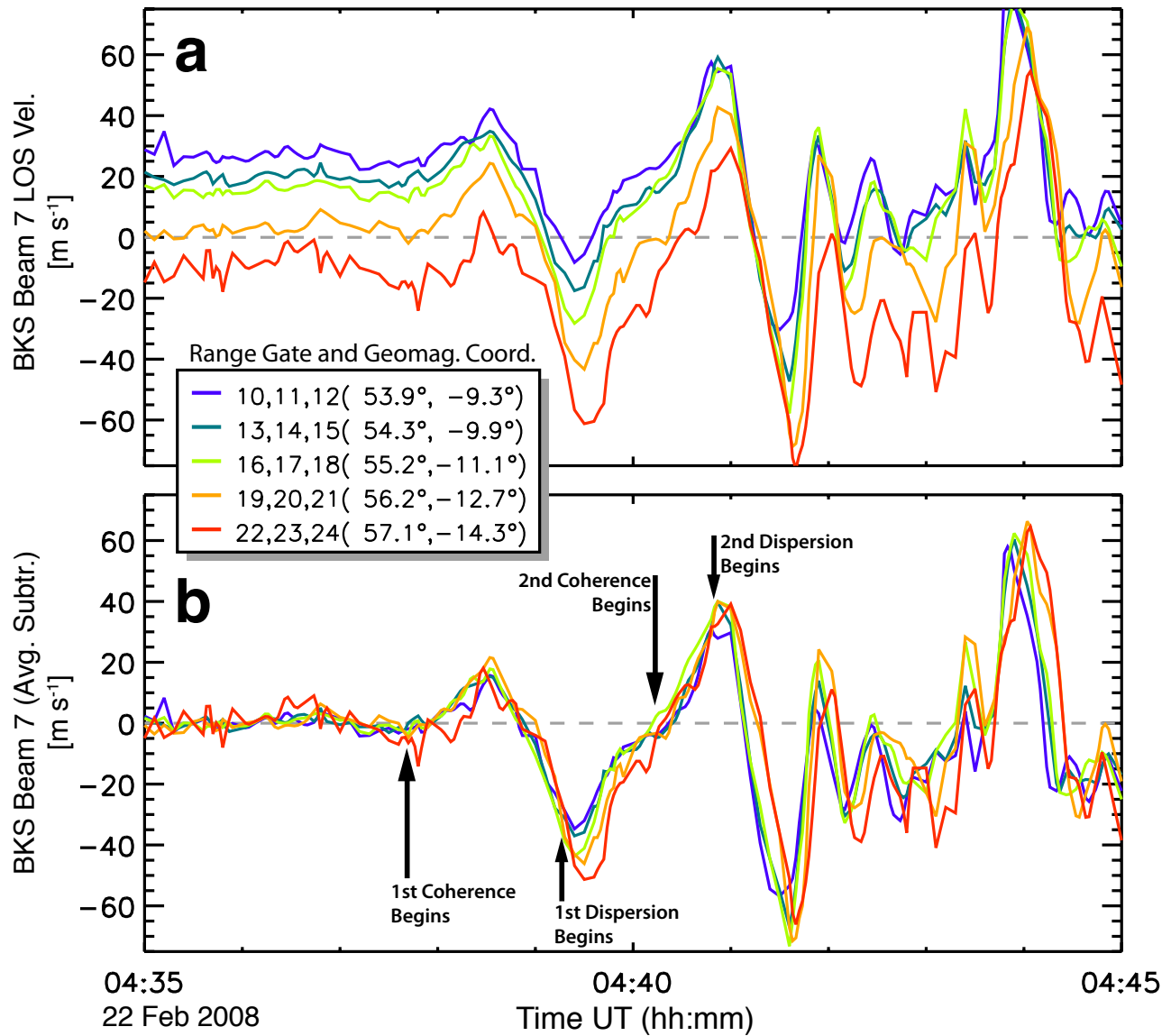


Figure 2.3: (a) 3 range gate averages of BKS beam 7 LOS velocity data. (b) Same as (a), but average subtracted. During intervals marked as coherences, the velocity traces from all latitudes move together as energy from BBF braking pushes on the field lines. During intervals marked as dispersions, field lines move back toward their original state.

Climatology of Medium Scale Traveling Ionospheric Disturbances Observed by the Midlatitude Blackstone SuperDARN Radar

N. A. Frissell¹, J. B. H. Baker¹, J. M. Ruohoniemi¹, A. J. Gerrard², E. S. Miller³, J. P. Marini⁴, M. L. West⁴, and W. A. Bristow⁵

¹Bradley Department of Electrical and Computer Engineering, Virginia Tech, Blacksburg, Virginia, USA.

²The Center for Solar-Terrestrial Research, New Jersey Institute of Technology, Newark, New Jersey, USA.

³The Johns Hopkins University Applied Physics Laboratory, Laurel, Maryland, USA.

⁴Montclair State University, Montclair, New Jersey, USA.

⁵Geophysical Institute, University of Alaska, Fairbanks, Alaska, USA.

Published as:

Frissell, N. A., J.B.H. Baker, J. M. Ruohoniemi, A. J. Gerrard, E. S. Miller, J. P. Marini, M. L. West, and W. A. Bristow (2014), Climatology of medium-scale traveling ionospheric disturbances observed by the midlatitude Blackstone SuperDARN radar, *J. Geophys. Res. Space Physics*, 119, 76797697, doi:10.1002/2014JA019870.

Abstract

A climatology of daytime midlatitude medium scale traveling ionospheric disturbances (MSTIDs) observed by the Blackstone SuperDARN radar is presented. MSTIDs were observed primarily from Fall through Spring. Two populations were observed: a dominant population heading southeast (centered at 147° geographic azimuth, ranging from 100° to 210°), and a secondary population heading northwest (centered at -50° azimuth, ranging from -75° to -25°). Horizontal velocities ranged from 50-250 m s^{-1} with a distribution maximum between 100 to 150 m s^{-1} . Horizontal wavelengths ranged from 100-500 km with a distribution peak at 250 km, and periods between 23-60 min, suggesting the MSTIDs may be consistent with thermospheric gravity waves. A local time (LT) dependence was observed such that the dominant (southeastward) population decreased in number as the day progressed until a late afternoon increase. The secondary (northwestward) population appeared only in the afternoon, possibly indicative of neutral wind effects or variability of sources. LT dependence was not observed in other parameters. Possible solar-geomagnetic and tropospheric MSTID sources were considered. The auroral electrojet (AE) index showed a correlation with MSTID statistics. Reverse ray-tracing with the HINDGRATS model indicates the dominant population has source regions over the Great Lakes and near the geomagnetic cusp, while the secondary population source region is 100 km above the Atlantic Ocean east of the Carolinas. This suggests the dominant population may come from a region favorable to either tropospheric or geomagnetic sources, while the secondary population originates from a region favorable to secondary waves generated via lower atmospheric convection.

3.1 Introduction

Medium Scale Traveling Ionospheric Disturbances (MSTIDs) are quasiperiodic density perturbations of the F-region ionosphere with periods between 15 to 60 minutes, wavelengths of several hundred kilometers, and velocities between 100 to 250 m s⁻¹ [e.g., *Ogawa et al.*, 1987]. MSTIDs have been demonstrated to be associated with both electrodynamic processes and atmospheric gravity waves (AGWs). MSTIDs undergoing electrodynamic enhancement processes typically appear at night as brightenings in airglow signatures and are associated with enhancements in plasma-neutral coupling in certain geometries [*Ogawa et al.*, 2009; *Kelley*, 2011]. MSTIDs have also been attributed to AGWs since *Hines* [1960], and these may be observed during all local times, seasons, and geomagnetic conditions. AGWs provide important dynamical coupling, as they transfer energy and momentum from one region of the atmosphere to another [*Fritts and Alexander*, 2003; *Alexander et al.*, 2010]. Although MSTIDs have been studied for many years, their sources and underlying physics are still not well understood.

MSTIDs are observed using both radio (e.g., radar, ionosonde, GPS-TEC) and optical (e.g., all sky imager, Fabry-Perot interferometer) techniques. Many studies have focused on the high latitude region, as it has been shown that geomagnetic influences have the ability to launch AGWs through processes such as Lorentz forcing and Joule heating [*Chimonas and Hines*, 1970]. Studies of MSTIDs using high latitude HF SuperDARN radars have linked them back to auroral zone sources [*Samson et al.*, 1990; *Bristow et al.*, 1994]. These studies also demonstrated that the MSTIDs can propagate over long distances, as some source regions were determined to be greater than 2000 km from the observation regions.

MSTID signatures observed by midlatitude radars share many similarities with high latitude observations, but it is unclear whether they share the same sources. The midlatitude region is

significantly farther from the auroral zone than the high latitude region, and the propagation mechanism suggested by *Samson et al.* [1990] and *Bristow et al.* [1994] is unlikely to support propagation to midlatitudes; *Francis* [1974] demonstrated that MSTIDs in this propagation mode undergo significant attenuation and loss of coherence after 3 to 5 wavelengths. Other sources may be significant contributors to midlatitude MSTIDs. Tropospheric sources, such as convective overshoot from hurricanes [*Vadas*, 2007] and large convective systems [*Nishioka et al.*, 2013], as well as AGWs launched by the solar terminator [*Kotake et al.*, 2007], have all been linked to midlatitude MSTID observations. Midlatitude MSTIDs are ubiquitous, routinely observed, and have been shown to propagate over long distances. In addition, the coupling processes between the neutral atmosphere and the ionosphere are very complex, and it has proved difficult to clearly identify sources.

Recently, there have been a number of studies of midlatitude MSTIDs that use SuperDARN HF radars. *Ishida et al.* [2008] conducted a statistical study using SuperDARN radars in Japan and Alaska that suggested that MSTID propagation from high to midlatitudes is possible. *Grocott et al.* [2013] conducted a more extensive study using the midlatitude, southern hemisphere Falkland Islands Radar. They found a correlation (albeit weak) between geomagnetic activity and MSTID occurrence, as well as a preferential equatorward direction of propagation for the majority of MSTIDs observed. They also identified a smaller MSTID population that was attributed to AGWs generated by winds traversing the Andes Mountains of South America.

In this study, we continue the search for sources of midlatitude MSTIDs by analyzing observations from the northern hemisphere SuperDARN radar located in Blackstone, Virginia. We start by comparing a very clear MSTID event observed by the Blackstone Radar (BKS) with a similar and coincident MSTID event observed by the high latitude Goose Bay Radar (GBR) in order to assess the likelihood of shared sources. We determine the MSTID

parameters using a cross-spectral analysis technique and examine these events in the context of geomagnetic activity. The analysis techniques introduced in this event study are then applied to a statistical study of MSTIDs observed by BKS from 1 June 2010 to 31 May 2011. Distributions of MSTID occurrence, propagation azimuth, velocity, wavelength, and period are presented. Seasonal and diurnal dependencies are identified in the observed MSTIDs. Sources of the MSTIDs are explored through correlations with the Auroral Electrojet (AE) index and reverse ray-tracing of gravity waves to their possible sources regions.

3.2 Instrumentation

3.2.1 SuperDARN

In this paper, we use data from radars located in Blackstone, Virginia (BKS) and Goose Bay, Canada (GBR) to observe MSTIDs. Figure 3.1a shows the locations of both radars and their fields-of-view (FOV) computed with a standard slant range mapping. The plots show the spatial distribution of backscattered power for a 1-minute scan performed on 19 November 2010 at 1440 UT. These radars are part of the Super Dual Auroral Radar Network (SuperDARN), an international array of high-frequency (HF) coherent scatter radars located in both the Northern and Southern Hemispheres [*Greenwald et al.*, 1995; *Chisham et al.*, 2007]. Each radar has a main linear phased array with 16 antennas and operates between 8 - 20 MHz in a variety of modes. In normal operation, these radars scan through 16 beams of 3.24° azimuthal separation and complete a full $\sim 52^\circ$ scan in 1 min. A $300 \mu\text{s}$ pulse provides 45 km range gates along each beam. Each beam has up to 110 range gates, providing range coverage extending beyond 3000 km.

The main purpose of SuperDARN is to make ionospheric line-of-sight velocity measurements

on the basis of the Doppler shift on coherent backscatter from decameter-scale field-aligned irregularities in the F-region ionosphere. However, not all scatter detected by a SuperDARN radar comes from ionospheric irregularities. Ionospheric density gradients may bend radar signals back toward Earth where they may scatter off of the ground (so-called “ground-scatter”). This is shown schematically in Figure 3.2a. Here, TIDs modulate the F-region ionosphere and cause quasiperiodic density rarefactions and enhancements in the ionospheric layer. The rarefaction results in a concave structure in ionospheric density that focuses the radar rays reflecting to the ground, while the enhancement creates a convex structure that defocuses them. As a result, moving bands of enhanced ground scatter power are indicative of rarefaction regions generated by a passing MSTID. Figure 3.1a shows ground scatter data observed by the GBR and BKS radars that includes red bands of enhanced backscatter power caused by the ionospheric focusing described above.

Typically, the slant range is used to measure the distance to SuperDARN targets in the ionosphere. The standard slant range mapping is used in Figure 3.1a. Because the TID occurs at the ionospheric reflection point rather than at the ground (Figure 3.2a), the measured slant range must be mapped to the ionospheric reflection point before any further analysis is done. Otherwise, errors will be made when calculating the wavelength and propagation direction of the TID. *Bristow et al.* [1994] calculated a ground-scatter mapped range that is slightly less than half of the slant range:

$$D \approx R_e \sin^{-1} \left[\frac{\sqrt{R^2/4 - h^2}}{R_e} \right] \quad (3.1)$$

Figure 3.2b illustrates the geometry of this equation. Here, D is the ground scatter mapped range, R_e is the radius of the Earth, R is the slant range, and h is the altitude of the ionosphere. Figure 3.1b shows the result of this mapping applied to the FOVs and data first shown in Figure 3.1a. Unless otherwise noted, all ranges in this paper are reported as ground

scatter mapped ranges with an assumed $h = 250$ km.

3.3 Observations

3.3.1 Event Study: 19 November 2010, 1200-2000 UT

We begin by analyzing an MSTID event on 19 November 2010 from 1200 to 2000 UT observed by both the high-latitude Goose Bay (GBR) radar and the mid-latitude Blackstone (BKS) radar. During this time, both radars observed very clear MSTID signatures with similar characteristics. We use this event to search for possible MSTID source(s) while illustrating MSTID features and analysis techniques. In particular, the analysis techniques described here allow for the determination of MSTID parameters such as propagation azimuth, horizontal velocity, horizontal wavelength, and period. Many previous studies have suggested auroral/geomagnetic sources to be the cause of MSTIDs at both high-latitudes [*Samson et al.*, 1990; *Bristow et al.*, 1994] and mid-latitudes [*Grocott et al.*, 2013]. We have chosen the GBR and BKS radars because they cover similar longitudinal sectors, making it more likely that both radars could see MSTIDs generated by a single auroral source.

RTI Analysis

A one-minute scan of power data beginning on 19 November 2010 at 1440 UT was presented in Figure 3.1. The enhanced red regions correspond to ionospheric density rarefactions caused by MSTIDs passing through the fields-of-view (FOVs) of the radars. However, it is not possible to see the time evolution of the MSTIDs using this format. Figure 3.3 shows the time-evolution of the data from the most northward looking beam of each radar in Range-Time-Intensity (RTI) format. As discussed in Section 3.2.1, good F-region ground

scatter is required to make MSTID observations. GBR observes strong ground scatter from ~ 1330 to 2000 UT between ~ 600 to 1200 km range, while BKS observes strong ground scatter from ~ 1230 to 2200 UT between ~ 200 to 600 km in range. Because these observations are made in the Northern Hemisphere in the late fall, BKS receives more daylight than GBR and therefore observes a longer period of ground scatter. Both stations show significant MSTID activity as soon as good ground scatter conditions appear following sunrise. MSTID signatures are seen as red slanted striations in the data, and selected MSTIDs have been identified with dotted lines and boxes for later analysis. The negative slope of the striations indicates that the MSTID structures are moving toward the radar with time. A sequence of striations with consistent slopes constitutes an MSTID wavetrain. The MSTID activity is quite complex; multiple, different MSTID wavetrains can be seen in the RTI plots by observing changes in slope and shape. A good example of this occurs in the beginning of the boxed GBR data, where a remnant of an MSTID wavetrain with a shallow slope can be seen mixing with the first striation of the next wavetrain.

We now focus on the clearest MSTID signatures, which have been identified with dotted lines in Figure 3.3, in order to make quantitative estimates of MSTID parameters. The slope and spacing of the dotted lines, which we placed visually on the figure, were used to calculate average period, frequency, and phase velocity. The GBR MSTIDs have an average period of 24 min (0.69 mHz) and phase velocity of 243 m s^{-1} , while the BKS MSTIDs have an average period 32 min (0.51 mHz) and phase velocity of 88 m s^{-1} . This simple method of analysis, which uses only line-of-sight measurements of the MSTIDs, provides a good starting point for estimating MSTID parameters. However, some questions are raised. First, do line-of-sight measurements made with this technique properly observe MSTIDs at all orientations relative to the radar look direction? Second, is there an analysis technique that uses all of the radar data available and overcomes the issues that single beam measurements create?

It is likely that the orientation of the radar beam look direction relative to the MSTID propagation direction does affect observed MSTID parameters. For a stationary MSTID structure in an otherwise smooth ionosphere, a single beam can only measure the correct wavelength if the MSTID is orthogonal to the beam look direction. If the MSTID were to rotate in either direction from the orthogonal, the observed wavelength would increase. Once the MSTID is parallel to the beam orientation, the MSTID wavelength will be infinite along that beam. Therefore, we must consider an instrumental bias regarding the sensitivity of the radar to MSTIDs moving in particular directions relative to the field-of-view. One method of addressing this issue is to use data from more than one look direction (beam) of the radar. In this particular case study, GBR Beam 6 (Figure 3.3a) shows very clear MSTID signatures. Meanwhile, the most westward and eastward GBR Beams 0 and 15 (not shown) show very diminished MSTID signatures. In contrast, BKS shows strong MSTID signatures in all beams for this event. Next, we describe a technique that uses the data from all available beams when calculating MSTID frequency/period, horizontal wavelength, and horizontal velocity. There may still be an additional instrumental look-direction bias after applying this technique. We discuss this bias during the statistical study at the end of Section 3.3.2.

MUSIC Analysis¹

Our subsequent analysis uses the Multiple Signal Classification (MUSIC) algorithm, which was first described in general by *Schmidt* [1986] and first implemented for use with SuperDARN data by *Samson et al.* [1989, 1990] and then *Bristow et al.* [1994]. MUSIC is a cross-spectral analysis technique that can take into account all data within a scan for a given time period and determine parameters for multiple MSTIDs passing through the FOV. We have reimplemented MUSIC for this study, following closely the procedure described by *Samson et al.* [1990]. We

¹This section is expanded compared to the published *Frissell et al.* [2014b] study.

now analyze the 19 November 2010 event while explaining the MUSIC procedure.

Two hours of data representative of the average MSTID conditions observed by each radar are chosen, as indicated by the boxes shown in Figure 3.3. The data selection is limited in both time and range. However, it is important to note that data from all beams, not just those shown in Figure 3.3, are used in the MUSIC analysis. To facilitate signal processing, an equispaced dataset is created through linear interpolation first in range and then in time. At this point, each range-beam cell time series is bandpass filtered using a 0.5–1.2 mHz ($T = 14 - 33$ min) passband to isolate the dominant MSTID. The power spectral density of each time series is then computed with an FFT. To determine the frequency of the most dominant signal within the radar FOV, the power spectral density matrix is integrated with respect to range and beam. The FFT bin with the largest integrated power spectral density is identified as frequency of the observed MSTIDs. The dominant frequency observed by both GBR and BKS is $f = 7.0$ mHz ($T = 24$ min).

To determine the wavenumbers of the observed MSTIDs, the spectra computed above are then used to calculate a cross-spectral density matrix D_{lm} :

$$D_{lm} = \sum_{\omega} s(\mathbf{r}_l, \omega) s^*(\mathbf{r}_m, \omega) \quad (3.2)$$

Here, $s(\mathbf{r}_l, \omega)$ is the spectrum measured at location l and $s^*(\mathbf{r}_m, \omega)$ is the complex conjugate of the spectrum measured at location m . Locations l and m range from 0 to M , where $M + 1$ is the total number of range-beam cells under analysis. *Schmidt* [1986] shows that if there are p signals (MSTIDs) incident on the sensor array (radar range-beam cells), D_{lm} will have p or less eigenvalues > 0 corresponding to the incident signals and $M - p$ eigenvalues approximately equal to 0 corresponding to noise. These $M - p$ noise eigenvalues correspond to set of noise eigenvectors that are orthogonal to space spanned by the signal eigenvectors.

Therefore, the power spectral density $P(\mathbf{u})$ for a particular signal (MSTID) may be estimated as:

$$P(\mathbf{u}) = \frac{1}{\sum_{j=p+1}^M \mathbf{u}^t \mathbf{v}_j \mathbf{v}_j^t \mathbf{u}} \quad (3.3)$$

Here, \mathbf{v}_j for $j = (p + 1, M)$ is the set of noise eigenvectors, \mathbf{u} is the test signal vector, and superscript t denotes the Hermitian adjoint. A plane wave model of test signal vector \mathbf{u} was used, with components in the form of $u_m = \exp(ik_x x_m + ik_y y_m)$. A local Cartesian coordinate system (+ x North, + y East) was defined assuming a flat ionosphere with the origin at the center of the selected range-beam cell array. An array of wavenumbers were tested by systematically varying k_x and k_y over the range of -0.05 to 0.05 rad km⁻¹.

The final result of this horizontal wavenumber estimation for the 19 November 2010 event is shown in Figure 3.4 for GBR (upper) and BKS (lower). An image processing watershed algorithm determines the location of the largest local maxima within the array. This algorithm detected three MSTIDs in GBR, and one MSTID in BKS. The dominant MSTIDs (largest local maxima) are marked with the numeral (1). For GBR, (1) is located at horizontal wave numbers $k_x = 0.025$, $k_y = -0.016$, and $k = 0.030$. This corresponds to a horizontal wavelength of $\lambda = 2\pi/k = 212$ km and a horizontal propagation azimuth of $\phi = 123^\circ$ with respect to geographic North. The phase velocity is $v_p = \omega/k = 147$ m s⁻¹. For BKS, (1) is located at horizontal wave numbers $k_x = 0.019$, $k_y = -0.026$, and $k = 0.032$. This corresponds to a horizontal wavelength of $\lambda = 195$ km and a horizontal propagation azimuth of $\phi = 144^\circ$. The phase velocity is $v_p = 135$ m s⁻¹. Both of these dominant MSTIDs are propagating southeastward, which is consistent with the MSTIDs moving toward the radars in the RTI plots of Figure 3.3.

We have tested the MUSIC estimator via forward modeling, and it has proved to be robust under a variety of signal and noise inputs. As with any technique, however, there are caveats to be aware of. Wavenumber estimation errors may occur due to some bias in radar look-direction sensitivity, the assumption of a locally flat ionosphere, and unreasonably large horizontal wavelengths as k approaches 0. As typical MSTID field-of-view scales are $\lesssim 0.10 R_E$, we believe the flat ionosphere approximation is appropriate in this implementation. To address the issue of large wavelengths as k approaches 0, we reject MSTIDs with $\lambda_h > 750$ km, which is consistent with the definition of MSTIDs [Ogawa *et al.*, 1987]. Finally, we note that only a single temporal frequency is resolved to characterize all MSTIDs within an observational window, which will likely result in an incorrect phase velocity calculation for some observed MSTIDs. To address this, we use only the most dominant observed MSTID in automated analysis. In a case study, manual techniques can be used to resolve separate frequencies for multiple MSTIDs within a given sampling window.

Possible MSTID Sources

Based on observational similarities with MSTIDs analyzed by Samson *et al.* [1990] and Bristow *et al.* [1994], the GBR observations presented here have the characteristics of an MSTID associated with an AGW generated by Lorentz forcing or Joule heating in the auroral zone. Ishida *et al.* [2008] and Grocott *et al.* [2013] both suggest that mid-latitude MSTIDs, such as those observed by BKS, could also be generated in the auroral zone through geomagnetic forcing processes. To search for a possible geomagnetic source, we examined data from a longitudinal chain of magnetometers distributed along the Eastern coast of North America through Greenland, as well as a chain in Alaska. Figure 3.5 shows the B_x north-south component of the North American-Greenland magnetometer chain. All magnetometers above 70° MLAT show a disturbance that peaks at 0910 UT (indicated by the red vertical

dashed line), indicative of a surge in the westward electrojet. The times of first MSTID observations by BKS (green dashed line) and GBR (blue dashed line) are also indicated on the magnetogram. This disturbance can also be seen at the same latitude in the Alaskan chain (magnetogram not shown). As this disturbance is seen in both chains, it is likely that the surge is continuous across the entire North American continent. The largest disturbance is seen at Cape Dorset (CDRT), there being no disturbances equatorward of this station, and the magnitude of the disturbances diminishes poleward. Therefore, the surge likely occurs near the magnetic latitude of CDRT (73.8° MLAT).

Figure 3.6 is a map in magnetic coordinates that shows the locations of the magnetometers (blue dots), the latitude of the electrojet surge (blue dashed circle), and the 19 November 2010 1440 UT scan of filtered radar data from GBR and BKS. A black arrow in the middle of each radar FOV indicates the MSTID propagation direction determined by the MUSIC analysis. GBR is quite close to the surge latitude (<1350 km from CDRT) and shows an MSTID propagating away from the CDRT region. It would take only a few hours for an MSTID to arrive at GBR from CDRT using the speeds and azimuth calculated here. This is reasonable and suggestive of an auroral source for the GBR observations. BKS is much farther away, and the propagation time from the high latitude source region to the BKS observation point would cause the MSTID to arrive well after the first BKS MSTID observation. Therefore, although the BKS MSTID direction indicates that the source is poleward of the observations, it is quite difficult to attribute the electrojet surge at CDRT to the midlatitude MSTIDs for this particular event. In the next section, we will continue our search for MSTID sources with a statistical study, utilizing the analysis tools we have described here.

3.3.2 Statistical Study

We now present a statistical analysis of MSTID observations made by the Blackstone (BKS) radar from 1 June 2010 through 31 May 2011 for the purpose of understanding the behavior and characteristics of MSTIDs at midlatitudes and to further the search for the likely sources of these MSTIDs.

Sampling Window Selection and Classification

We begin by defining the procedure for MSTID identification used in this study. Each day of the study is divided into two-hour sampling windows that allow for between two to four cycles of MSTIDs within each window. Because we are interested in daytime MSTIDs, only sampling windows with start times between 0800 and 1700 magnetic local time (MLT) are included in the study. We further constrained the problem by restricting the sampling windows to radar ranges that typically contain adequate ground scatter for MSTID identification. We chose to retain data between range gates 10 through 35 based on the observations shown in Figure 3.7, which show the normalized ground scatter occurrence for BKS from 1 June 2010 through 31 May 2011 as a function of month and local time (UT - 5 hours). This choice of range gate limits was further confirmed by manually examining RTI plots of individual sampling windows.

An initial search was conducted by manually examining power range-time-intensity (RTI) plots from each of the 1562 sampling windows. Every sampling window was placed into one of three categories: MSTID, quiet, or discard. Figure 3.8 shows example RTI plots from each category. Sampling windows are demarcated by vertical blue dashed lines. Range gate limits 10 and 35 are marked with green horizontal dashed lines. Data within the white regions of the plots are used for analysis. Figure 3.8a shows examples of “MSTID periods” on 19 November

2010 between 1400 to 2200 UT. MSTID signatures can be seen in every sampling window shown in this figure. In contrast, Figure 3.8b shows examples of “quiet periods” during every sampling window on 13 September 2010 between 1400 to 2200 UT. Quiet periods are sampling windows that contain abundant ground scatter but have minimal signatures of MSTID activity. Some MSTID activity may be present during quiet periods, but it should be substantially less than that of an “MSTID period”. Finally, Figure 3.8c shows examples of “discard periods” on 16 May 2010 between 1400 to 2200 UT. Discard periods are sampling windows in which there is not sufficient ground scatter to make an adequate determination as to whether or not an MSTID is present.

The results of the manual search were used to generate distributions of ground scatter fraction and spectral content that were then used to select appropriate threshold values to objectively classify each of the sampling periods. Figure 3.9 shows the results of this search. The top panels (red) show distributions for MSTID periods, the middle panels (green) show distributions for quiet periods, and the bottom panels (blue) show distributions for discarded periods. 29 of the 1562 sampling windows were not included because there was either no data available, or there were data gaps in the sampling window longer than 10 minutes. The left column (Panels a-c) shows distributions of the ground scatter fraction (GSF), that is, the number of ground scatter returns within a sampling window divided by the total possible number of ground scatter returns. Here, the aim is to identify an appropriate threshold for GSF that allows for automated identification of periods with sufficient ground scatter to identify MSTIDs. A threshold value of 0.25 was selected for the GSF (identified by vertical dashed lines). In subsequent analysis, sampling windows with GSF values below this threshold will be classified as discards, while sampling windows with a $\text{GSF} \geq 0.25$ will move on to be classified as either MSTID or quiet periods.

The right column (Panels d-f) of Figure 3.9 shows distributions of the total spectral power

within the MSTID band, which can be used to distinguish “MSTID periods” from “quiet periods”. This is calculated by first bandpass filtering ($0.3 \text{ MHz} < f < 1.2 \text{ MHz}$) each individual beam-range cell power parameter time series within a sampling window and then computing the FFT magnitude. The resulting array is then integrated to give a single value representing the total MSTID power within the sampling window. A threshold value of 2800 is selected (again identified by vertical dashed lines). Sampling windows that have not been discarded and have total spectral power values that fall below this threshold are classified as quiet, while all remaining sampling windows are classified as MSTID. Figure 3.10 is in the same format as Figure 3.9, but now shows the final results of the classification process. We reviewed the results of this automatic classification process and found them to be similar to the results of the original manual classification. These automated classifications will be used for the remainder of this statistical study.

Occurrence Statistics of MSTIDs

As a result of the search and classification process described in Section 3.3.2, 629 MSTID periods and 360 quiet periods were found. Figure 3.11 shows occurrence statistics as a function of season for both the MSTID periods (upper) and quiet periods (lower). The MSTIDs were found most often in the late fall through early spring (October through March) with the MSTIDs observed in November and December being especially prominent. Quiet periods were observed in late spring and early fall. Almost no observations were made during June and July.

It is useful to revisit the ground scatter distribution shown in Figure 3.7 when interpreting the seasonal dependence of Figure 3.11. The best ground scatter conditions for MSTID observations at BKS occur from January through April and September through December. From May through August the ground scatter is more variable and closer in range to the

radar. This is likely due to an enhanced D and E region ionosphere during the summer. The enhanced D region suppresses F-region ground scatter due to absorption, while scatter from Sporadic E and E-region field aligned irregularities overpowers the F-region ground scatter [de Larquier et al., 2011]. Although this presents an instrumental bias in the observation of MSTIDs during the summer, Figure 3.11 shows evidence that MSTID occurrence actually decreases toward summer. During the late spring and early fall, but before the drop-off in observations during June and July, the MSTID observations decrease as the quiet period observations increase. This indicates that the true MSTID count is also likely to decrease during June and July.

Geomagnetic Dependence of MSTID Occurrence

We can correlate the MSTID occurrence statistics with the Auroral Electrojet (AE) index in order to gauge the importance of high latitude geomagnetic processes on midlatitude MSTID generation. We obtained the AE measurement with the greatest magnitude during each sampling window and plot histograms for both the MSTID periods (upper) and quiet periods (lower) in Figure 3.12. The histograms show that AE is generally higher for the MSTID periods versus the quiet periods, indicating slightly enhanced auroral activity during MSTID periods. The MSTID period distribution has a mean AE of 169 nT while the quiet period distribution has a mean of 120 nT. In order to show that the distributions of MSTID events versus quiet events are in fact different, the Kolmogorov-Smirnov (K-S) test was applied. For these AE distributions, the K-S statistic is $D = 0.1869$ with $P = 0.000$. Because D is small, yet statistically significant ($P \ll 0.05$), this provides evidence that the two distributions are in fact different. This supports the hypothesis that geomagnetic activity correlates with the occurrence of midlatitude MSTIDs.

Propagation Characteristics of MSTIDs

We now proceed by processing each MSTID sampling window identified in Section 3.3.2 using the Multiple Signal Classification (MUSIC) algorithm as described in Section 3.3.1 in order to determine distributions of MSTID frequency and period, horizontal wavelength, horizontal velocity, and horizontal propagation azimuth. For this statistical study, a 0.3-1.2 mHz ($T = 14 - 56$ min) passband filter was applied to all data as recommended by *Bristow et al.* [1994, 1996]. As multiple MSTIDs may be present within a sampling window, we selected only the strongest MSTID with a horizontal wavelength $\lambda < 750$ km from each window. Due to the spatial sampling grid of the radar, the lower limit of observable wavelengths is on the order of 90 km. Because observed velocities are given as ω/k , possible horizontal velocities fall in the range of $30 \lesssim v \lesssim 900$ m s⁻¹. This choice of filtering is appropriate based on the definition of MSTIDs given in Section 3.1 and will also cause the results to focus on the most dominant MSTIDs observed.

Figure 3.13 shows the MSTID parameter distributions calculated using this analysis. Gaussian distributions were fit to estimate the mean and standard deviation of each parameter. These results are summarized in Table 3.1 and are used to drive the HINDGRATS (HINDcast Gravity wave RAY Tracer) reverse ray-trace model in a source region search described in Section 3.3.2. The top three panels show the distributions of (a) frequency and period, (b) horizontal wavelength, and (c) horizontal velocity, respectively. The majority of values are within normal ranges for midlatitude MSTIDs. Most MSTIDs have frequencies between 0.28 and 0.70 mHz corresponding to periods ranging from 23 to 60 min. The bulk of the MSTID horizontal wavelengths range from 100 to 500 km with a distribution maximum near 250 km. Likewise, the majority of MSTID velocities fall between 50 to 250 m s⁻¹ with a distribution maximum near 150 m s⁻¹.

The propagation azimuth distribution is shown in the bottom panel of Figure 3.13; 0° azimuth points toward geographic North, and East goes in the positive direction. It reveals two separate populations of MSTIDs. The larger, dominant population is heading southeast (centered at 147° , ranging from 100° to 210°), and the smaller population is heading northwest (centered at -50° , ranging from -75° to -25°). We examined the seasonal occurrence, frequency, wavelength, and velocity distributions of each population separately (not shown). Both populations have very similar occurrence and frequency distributions as those shown in Figures 3.11a and 3.13a. The dominant, southeastward population also has wavelength and velocity distributions similar to Figures 3.13b and 3.13c, with a sharp peak around $\lambda = 250$ km and the majority of velocities between 100 to 150 m s^{-1} . However, the northwest heading population has wavelength and velocity distributions that are more spread than Figures 3.13b and 3.13c, with the bulk of wavelengths ranging between 200 to 500 km and the bulk of velocities ranging from 100 to 300 m s^{-1} .

These two azimuth distributions are directed very nearly parallel and anti-parallel to the radar boresight direction, which is indicative of a possible instrumental bias toward these look directions. However, the predominant equatorward and eastward results are consistent with other midlatitude MSTID studies, including those using different instruments and/or analysis techniques [Kotake *et al.*, 2007; Ishida *et al.*, 2008; Grocott *et al.*, 2013]. These studies typically attribute the equatorward MSTID observations to high latitude sources. The smaller, northwest-heading population is likely generated by different sources than the dominant population, possibly associated with the solar terminator or tropospheric sources. There is also evidence that suggests the neutral wind may play a role in controlling the propagation direction of the observable MSTID populations. This is discussed further in Section 3.3.2.

Local Time Dependence of MSTIDs

By binning the azimuth distribution of Figure 3.13d with respect to magnetic local time (MLT), we can look at the diurnal variations of the two MSTID populations. Figure 3.14 shows four MLT time bins, each two hours long, ranging from 08 to 16 MLT. The dominant, southeast-heading MSTID population decreases in number from 08 to 14 MLT before increasing again in the 14 to 16 MLT bin. By contrast, the northwest-heading population steadily increases as the day progresses; it is not clearly present until the afternoon.

The strong local time dependence of the northwest-heading population suggests a time-dependent source region. AGWs launched by the dusk terminator might generate such waves and explain the increase in MSTIDs with local time. *Kotake et al.* [2007] reports northwest-heading summertime afternoon MSTIDs that they attribute to AGWs launched by the dusk terminator in a perpendicular direction to the terminator. However, our observations occur mostly in the winter when the dusk terminator geometry is aligned to launch southwestward rather than northwestward waves. Even so, we examined the relationship between the MSTID parameters presented here with distance to the terminator and with solar declination angle, but did not find any physical dependence. This suggests that the terminator is not the source of these MSTIDs, or at least not the mechanism controlling the observed local time dependence.

The effects of neutral winds might explain the MLT dependence observed in the northwestward MSTID population. To first order, thermospheric neutral winds may modulate or filter AGWs (that may underlie the observed MSTIDs) when they propagate parallel to the flow [*Waldock and Jones*, 1986]. Doppler shifts may reduce the vertical scales of gravity waves that propagate parallel to the wind flow, leading to more rapid dissipation by viscosity, and also modulating the effectiveness of their perturbations of the ionospheric densities. Many studies have

observed this effect by looking at MSTID measurements along with models of thermospheric wind velocities [Waldock and Jones, 1986; Bristow *et al.*, 1996; Afraimovich *et al.*, 1999; Ishida *et al.*, 2008]. We tested our observations against this hypothesis by using the Horizontal Wind Model 2007 (HWM07), which provides an empirical, statistical model of the Earth's atmospheric zonal and meridional winds from 0 - 500 km altitude [Drob *et al.*, 2008]. Figure 3.15 presents results from an HWM07 run for 19 November 2010 for undisturbed conditions ($A_p = 0$). This date was chosen because it is representative of the period when the majority of our MSTID measurements were observed and also corresponds with the case study event examined in Section 3.3.1. Figure 3.15 shows an array of maps giving the magnitude and direction of the horizontal winds for altitudes from 200-350 km and times that correspond with the MLT time bins presented in Figure 3.14. The radar observations of MSTIDs analyzed in this paper are obtained in the F-region ionosphere at approximately 250 km altitude, which corresponds with row 3 of Figure 3.15. A blue star in each map indicates the center location of the BKS MSTID observations. The 8-10 MLT and 10-12 MLT maps between 250-350 km altitude show that the horizontal winds are strongly ($> 60 \text{ m s}^{-1}$) northwest all around the BKS observation region. This corresponds to the times when no northwest-heading MSTIDs are observed by BKS in Figures 3.14a and 3.14b. In the afternoon, however, Figure 3.15 shows that the wind velocities decrease in magnitude and rotate clockwise in the vicinity of the BKS observation region. This corresponds to the times when the northwest-heading MSTID population grows in Figures 3.14c and 3.14d. This correspondence supports the neutral wind filtering observations reported by previous authors.

HINDGRATS Ray Tracing Analysis of MSTID Source Regions

To further investigate possible source regions of the observed MSTIDs, we used the results of the climatology presented in this study to drive HINDGRATS (HINDcast Gravity wave RAY

Tracer), a reverse gravity wave ray-trace model. HINDGRATS is based on the Gravity wave regional Or Global RAY Tracer (GROGRAT) ray-tracing model, run in a reverse ray-tracing mode [Gerrard *et al.*, 2004; Brown *et al.*, 2004]. The model results are shown in Figure 3.16 and utilized a $2.5^\circ \times 2.5^\circ$ global atmospheric background that was based on yearly averaged HWM07-NRLMSISE00 empirical values. HWM07 (Horizontal Wind Model 2007) provides an empirical, statistical model of the Earth's atmospheric zonal and meridional winds from 0 - 500 km altitude [Drob *et al.*, 2008], while NRLMSISE00 (Naval Research Laboratory Mass Spectrometer Incoherent Scatter Radar 2000) is an empirical model providing atmospheric and ionospheric composition and temperatures [Picone *et al.*, 2002].

Figure 3.16 shows the results of eight separate runs conducted for both the northwest-heading and southeast-heading MSTID populations at 14, 16, 18 and 20 UT. Each panel in Figure 3.16 is marked with the UT run time and the approximate corresponding MLT time for the BKS observation region. These times correspond with the time bins used in Figure 3.14 and the run times shown in Figure 3.15. All runs were calculated with a non-time varying, stationary, background atmosphere. The starting gravity wave parameters were Gaussian distributed with mean k , l , and Ω (zonal wavenumber, meridional wavenumber, and observed frequency, respectively) values and one-standard deviation widths given in Table 3.1. These gravity waves were started at 220 km altitude (due to upper altitude model limitations) with amplitudes fixed at 10 m s^{-1} . All waves discussed herein propagated from their source regions in under 6 hours. Green traces in each panel represent individual waves from these distributions, while the red traces show the average of an entire run.

For the waves coming from the northwest (MSTID population heading southeast), the source region is calculated to be above the Great Lakes (mean geographic 43° N , 87° W) during the 14 and 16 UT runs. For the 18 and 20 UT runs, the source region is found to be $\sim 90\text{-}120$ km altitude over central Canada (mean geographic 54° N , 98° W). We also calculated the

great circle distance from the center of the BKS observation region (geographic 38.3° N, 79.3° W) to the mean source location for each model run. For the 14, 16, 18, and 20 UT runs, these distances are 710, 1060, 2530, and 2310 km, respectively. This trend corresponds well with the southeast-heading observations of Figure 3.14. That is, as the source region moves farther from the observation region, fewer MSTIDs are observed.

We note that each of these model runs indicates that the gravity wave source region lies between ~90-120 km altitude. This mesospheric-lower thermospheric region is known to be a complex mixture of dynamics and chemistry, including a region where gravity waves can be generated by at least two mechanisms: 1) secondary gravity wave generation induced by lower atmospheric (a.k.a., primary) gravity wave breaking and 2) from auroral and sub-auroral processes. The Great Lakes region is ripe for convective activity, frontogenesis, jet stream instability, etc., and therefore a probable source region for tropospherically generated AGWs. It is also reasonable to think that energy and momentum generated at high latitudes (such as from geomagnetic sources) could also propagate into this region. The source location identified over central Canada for the 18 and 20 UT runs has an average location of 65° N magnetic latitude and 1200 MLT [*Baker and Wing, 1989*], a region typically identified with the geomagnetic cusp [*Newell and Meng, 1988*] that has been identified as a likely source of high-latitude MSTIDs [*Bristow et al., 1994*].

The atmospheric gravity wave population from the Atlantic shows much less variation in location as a function of time than the AGW population from the northwest. The Atlantic population has a mean location of geographic 34° N, 74° W and an altitude of approximately 85 km. The average great circle distance from the BKS observation region is ~690 km, and varies less than 100 km throughout the 14 to 20 UT observation period. Even so, the average distance is observed to move closer to the radar with time. As with the southeast-heading dominant MSTID population, the number of northwest-heading MSTIDs increases (Figure

3.14) as the source region moves closer to the radar. The region identified here is along the climatological hurricane track east of the Carolinas where AGW generation would be more likely due to secondary waves generated via lower atmospheric convection [e.g., *Vadas and Crowley, 2010*].

3.4 Summary and Conclusions

We have presented a climatology of daytime midlatitude medium scale traveling ionospheric disturbances (MSTIDs) observed by the Blackstone (BKS) SuperDARN radar from 1 June 2010 through 31 May 2011 in a region southeast of the Great Lakes. MSTIDs were observed primarily from the late fall through early spring. Two populations were observed: the largest population heading southeast centered at 147° geographic azimuth, and a smaller, secondary population heading northwest centered at -50° geographic azimuth. Both populations have horizontal propagation velocities ranging from 50 to 250 m s^{-1} , horizontal wavelengths ranging from 100 to 500 km, and periods between 23 to 60 min. Sources of the observed MSTIDs were explored. A small but significant correlation of the MSTID population with the auroral electrojet (AE) index suggests geomagnetic activity may contribute to MSTID production. Reverse gravity-wave ray tracing using the HINDGRATS (HINDcast Gravity wave RAy Tracer) model shows that the southeast-heading MSTIDs are likely to come from regions favorable to atmospheric gravity wave (AGW) production by both tropospheric and geomagnetic sources, while the northwest-heading MSTID population is likely to come from a region over the Atlantic Ocean favorable to AGWs produced by tropospheric sources. A comparison of HINDGRATS results with the BKS observations suggests more MSTIDs are observed as the source region moves closer to the observation region. Finally, a comparison of the diurnal variations in the northwest-heading MSTID population with Horizontal Wind

Model 2007 (HWM07) thermospheric winds suggests neutral wind modulation or filtering may factor in to these observations.

In the future, a climatological study of MSTIDs using additional midlatitude radars is called for. By looking at MSTID behavior across longitudinal sectors and over a variety of terrain, it should be possible to gain a better understanding of the relative importance of geomagnetic versus tropospheric sources. Future studies should also include ionospheric-thermospheric modeling and an evaluation of parameters indicative of tropospheric sources.

3.5 Acknowledgments

The Virginia Tech authors acknowledge the support of the NSF under grant ATM-0946900 and ATM-0849031. AJG was supported by NSF ATM-0734241. The AE index was obtained from the World Data Center in Kyoto. We acknowledge NASA contract NAS5-02099 and V. Angelopoulos for use of ground magnetometer data from the THEMIS Mission. Specifically: S. Mende and C. T. Russell (NSF grant AGS-1004814), E. Steinmetz, Augsburg College, the Geophysical Institute Magnetometer Array operated by the Geophysical Institute, University of Alaska (<http://magnet.asf.alaska.edu>), the USGS Geomagnetism Program (<http://geomag.usgs.gov>), and the Tromsø Geophysical Observatory, University of Tromsø, Norway. We acknowledge the use of the Free Open Source Software projects used in this analysis: Ubuntu Linux, python, IPython, matplotlib, NumPy, SciPy, scikit-learn, and others.

	Mean	Std. Dev.
f [mHz]	0.47	0.07
λ [km]	250	65
v [m s ⁻¹]	130	35
Dominant Azm	147°	18°
Secondary Azm	-50°	18°

Table 3.1: MSTID parameters determined from distribution shown in Figure 3.13 using BKS data from 1 June 2010 through 31 May 2011.

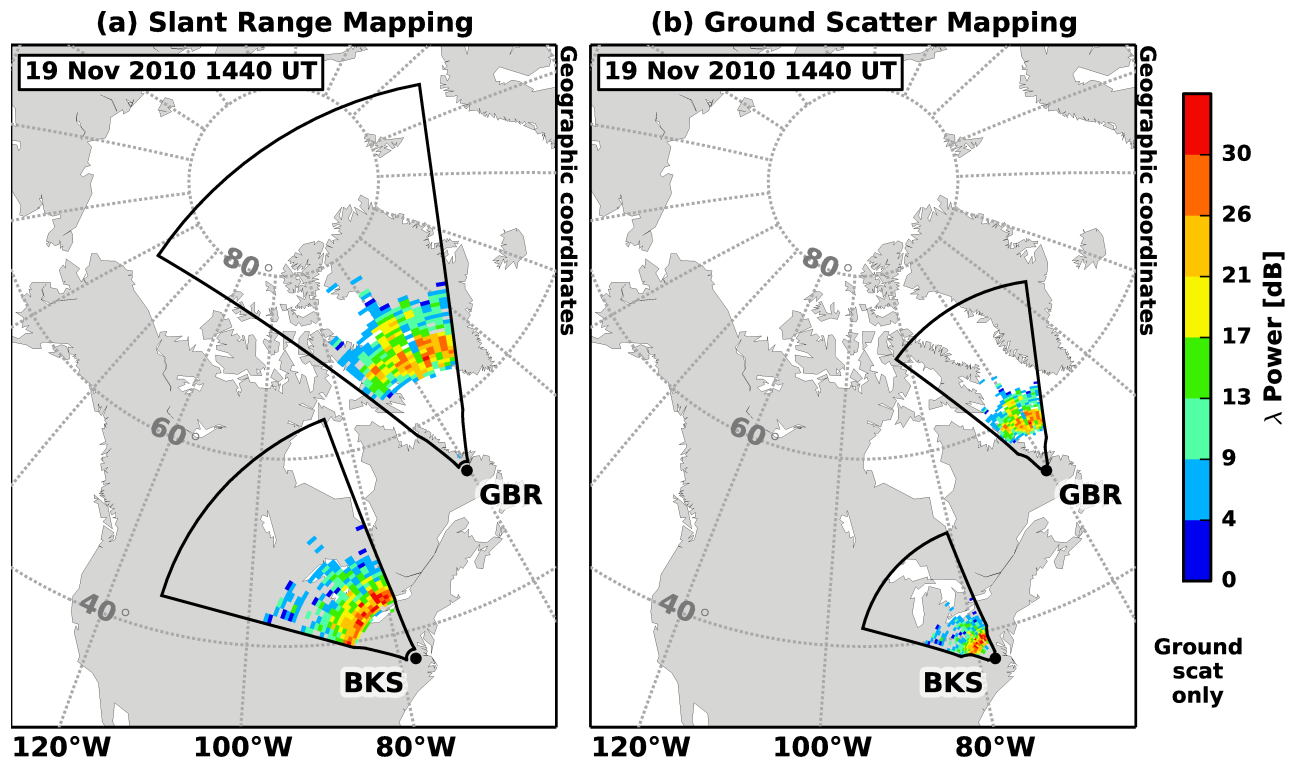


Figure 3.1: Ground scatter power data and FOVs from the BKS and GBR radars showing MSTIDs during a one minute scan starting on 19 November 2010 at 1440 UT: (a) standard slant range mapping; (b) ground scatter mapping as defined by Equation 3.1.

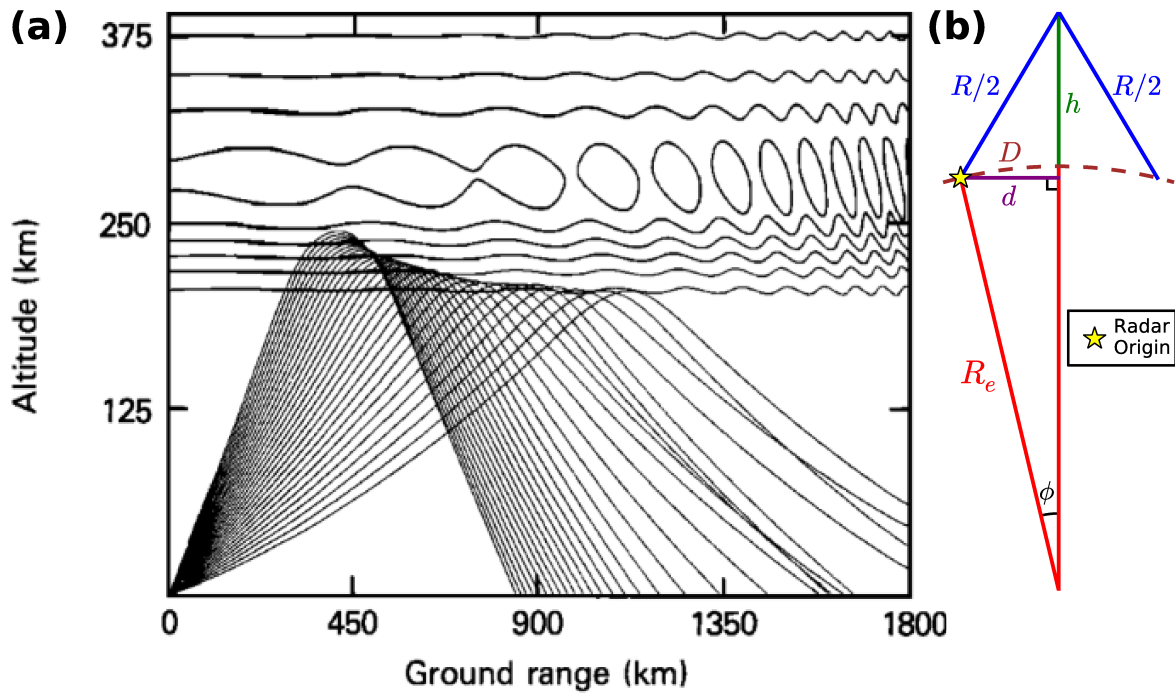


Figure 3.2: (a) HF ray-tracing from *Samson et al.* [1990] showing radar rays modulated by an MSTID passing through the F-Region ionosphere. Concavities in the ionospheric density focus rays on the ground, while convex regions defocus the rays. (b) Geometry used to derive the ground scatter mapping formula (Equation 3.1).

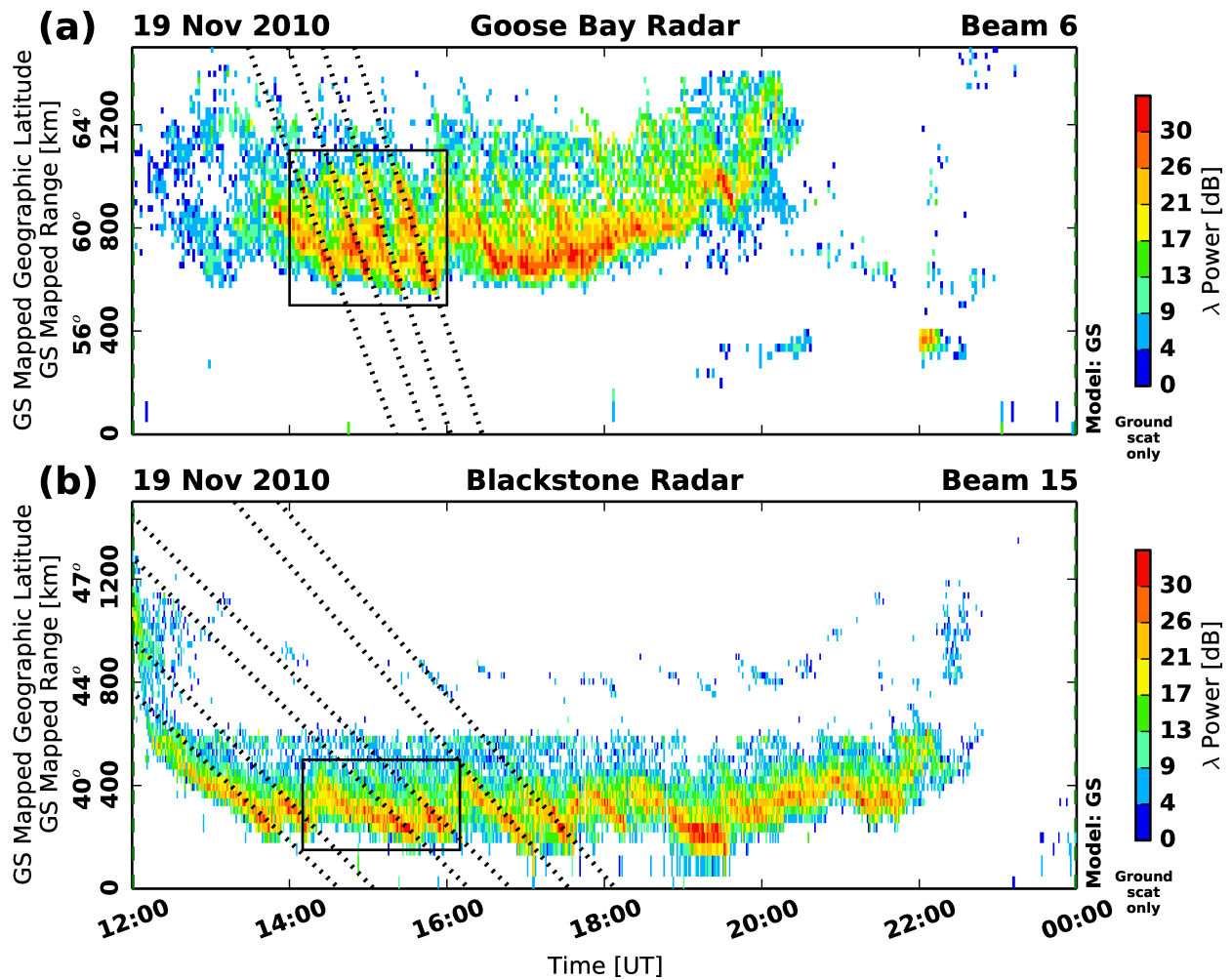


Figure 3.3: Range-time-intensity (RTI) plot of ground scatter power showing MSTIDs observed by both GBR Beam 6 (Panel a) and BKS Beam 15 (Panel b) during the daylight hours of 19 November 2010. MSTID signatures are observed as bright red stripes with a negative slope. Black dotted lines and boxes have been drawn over MSTIDs and regions selected for further analysis. See text for details.

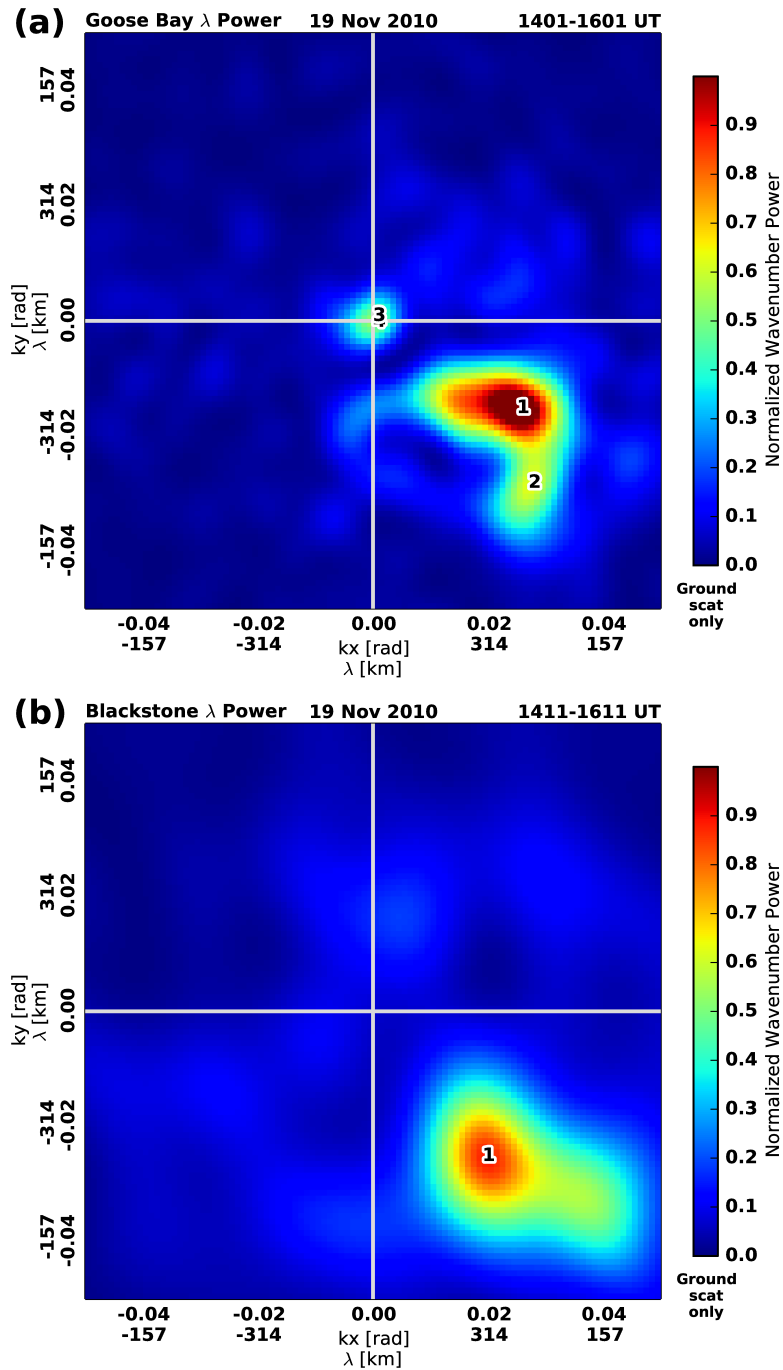


Figure 3.4: Horizontal wavenumber spectrum computed using the MUSIC algorithm for 19 Nov 2010 GBR 1401-1601 UT (top) and BKS 1411-1611 UT (bottom). k_x is the North-South wave number; k_y is the East-West wave number. An image processing watershed algorithm determines the location of the largest local maxima within the array.

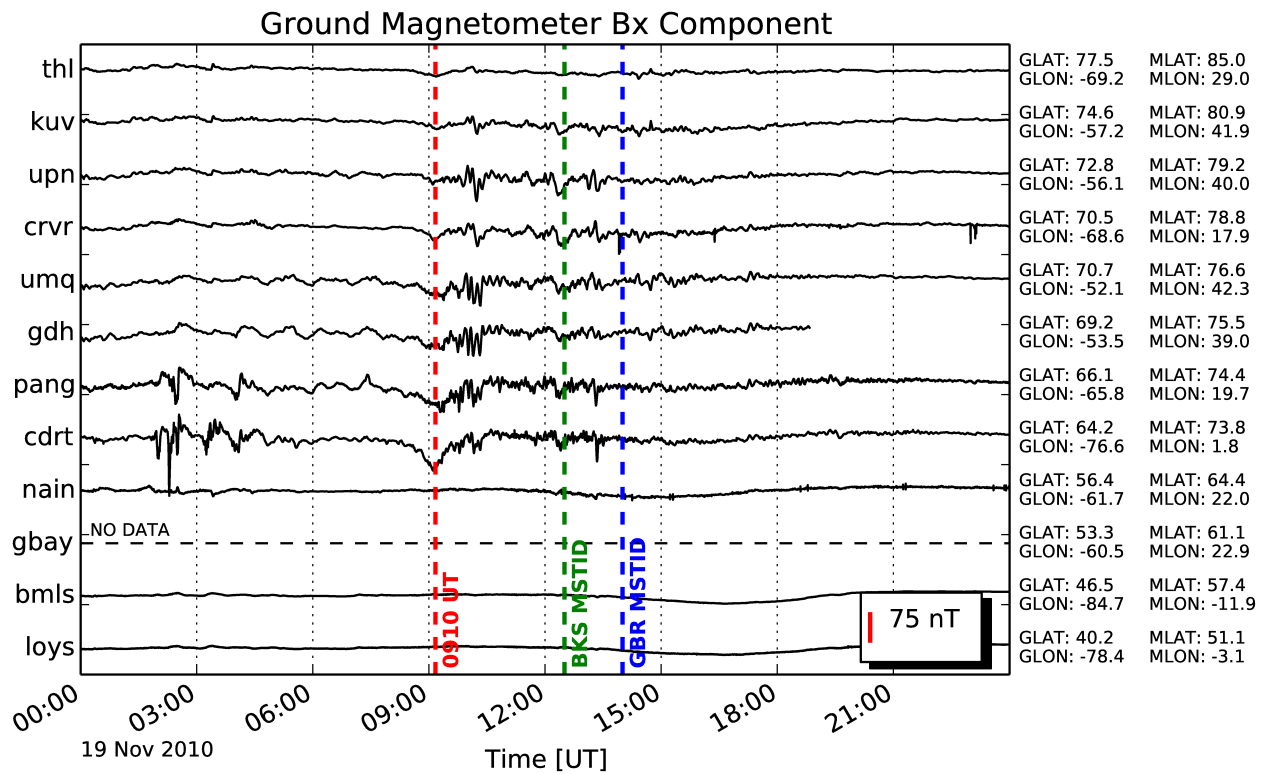


Figure 3.5: Stackplot of magnetograms showing the north-south B_x component of the North American-Greenland magnetometers identified in Figure 3.6. At 0910 UT, this chain was located in the morning sector near 0600 MLT. All magnetometers above 70° MLAT show a disturbance that peaks at 0910 UT (indicated by the red vertical dashed line). The green vertical dashed line at 1230 UT and the blue vertical dashed line at 1400 UT indicate the first observations of the MSTIDs at BKS and GBR, respectively.

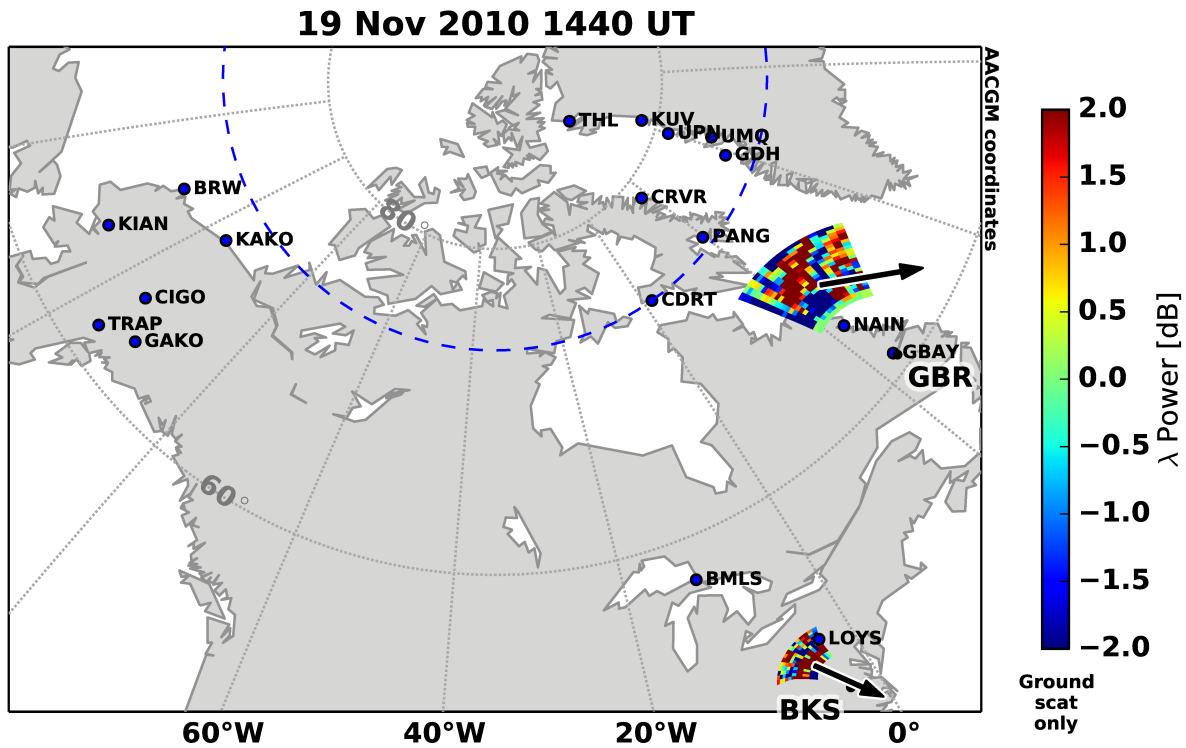


Figure 3.6: Map in magnetic coordinates of the 19 November 2010 MSTID event. GBR and BKS show filtered ground scatter power data from a one-minute scan starting at 1440 UT. The black arrows over the radar data indicate the average MSTID propagation azimuth as measured by the MUSIC algorithm. Blue dots indicate the location of ground magnetometer stations. The blue dashed circle is located at 74° MLAT, the likely magnetic latitude of a source auroral surge.

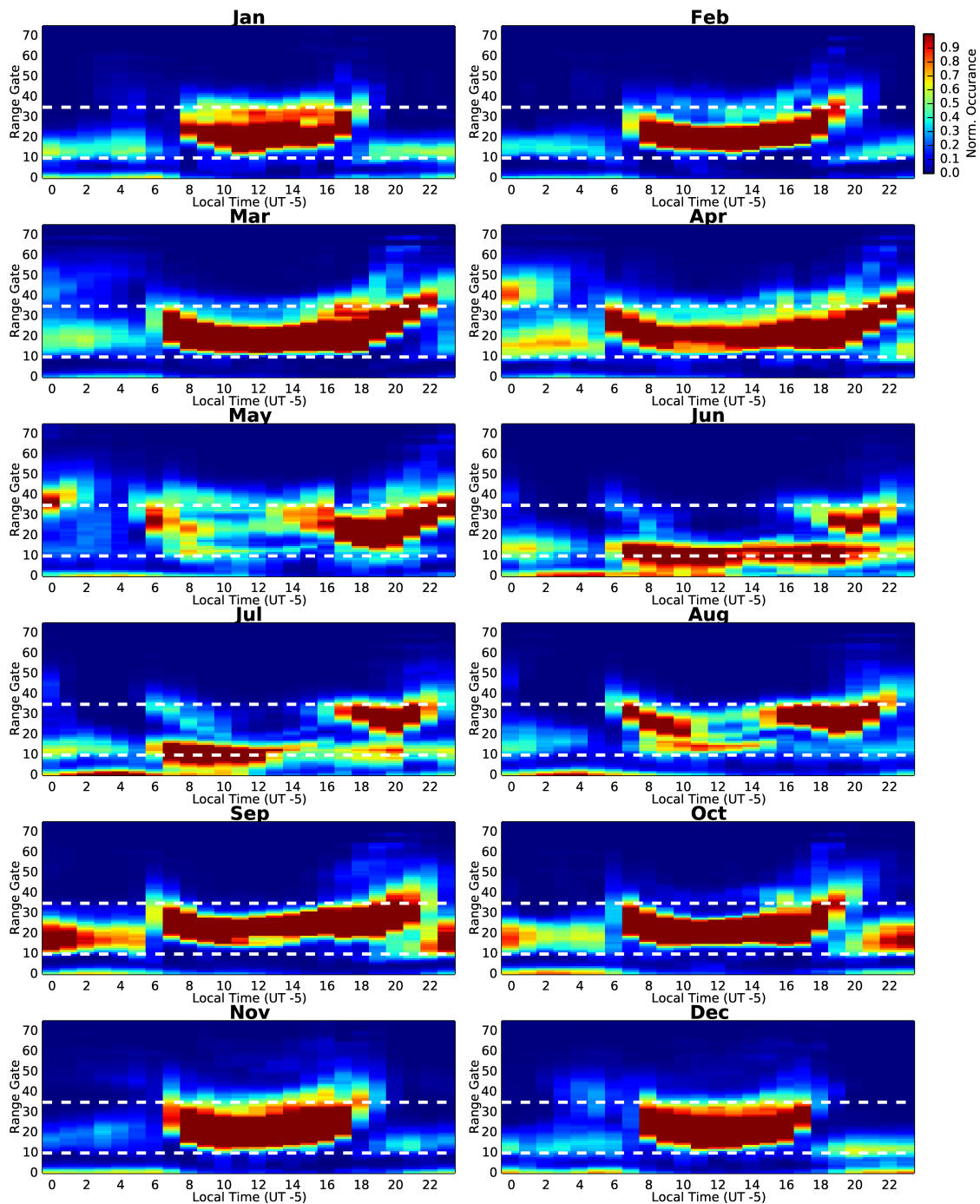


Figure 3.7: Normalized ground scatter occurrence for BKS from 1 June 2010 through 31 May 2011 as a function of month and local time (UT - 5 hours). The best ground scatter conditions for MSTID observation is found between range gates 10-35 (demarcated with white dashed lines).

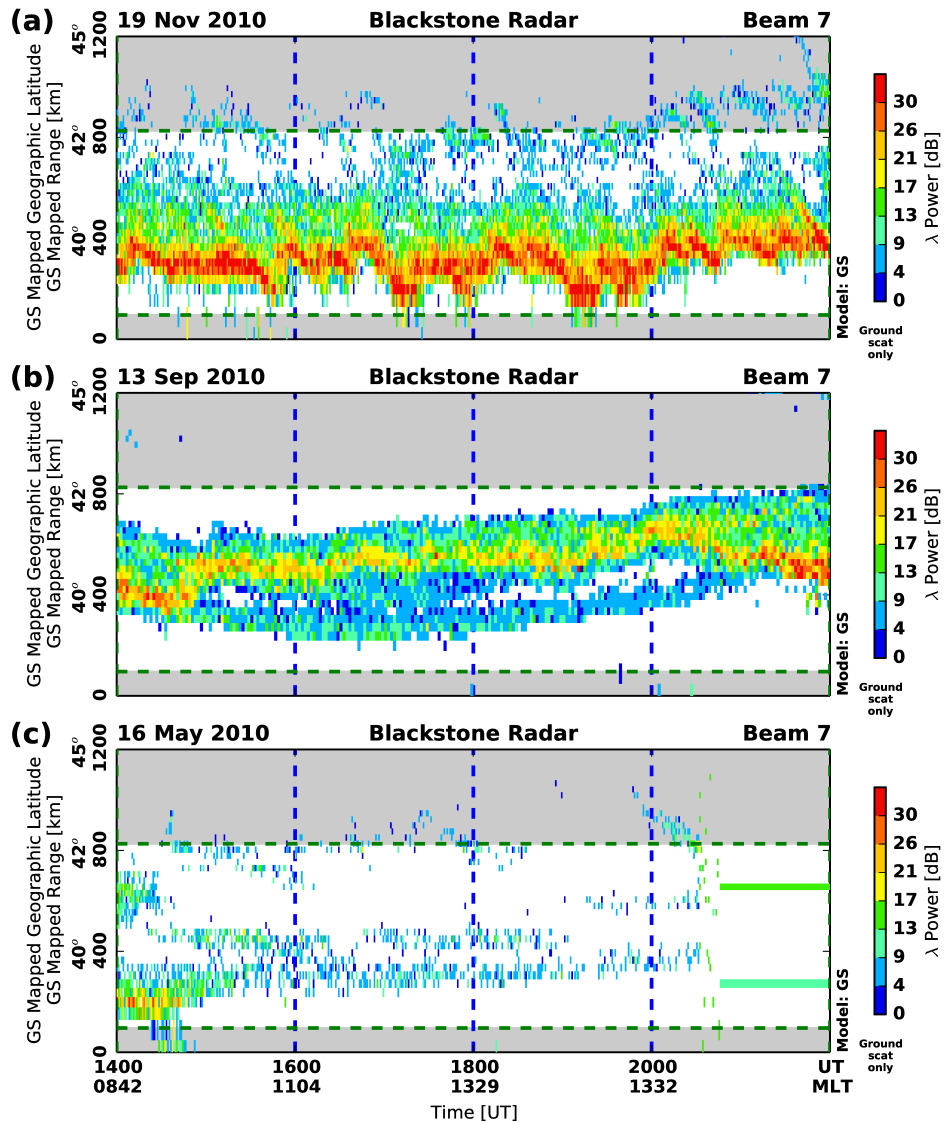


Figure 3.8: Examples of MSTID, quiet, and discard periods used in the statistical study of Section 3.3.2. Each RTI plot shows only ground scatter data from BKS Beam 7 and is divided into four 2-hour windows. (a) MSTID periods are shown in every 2-hour event period on 19 November 2010 from 1400-2200 UT; (b) Quiet periods are shown in every 2-hour period on 13 September 2010 from 1400-2200 UT; (c) Discard periods are shown in every 2-hour period on 16 May 2010 from 1400-2200 UT.

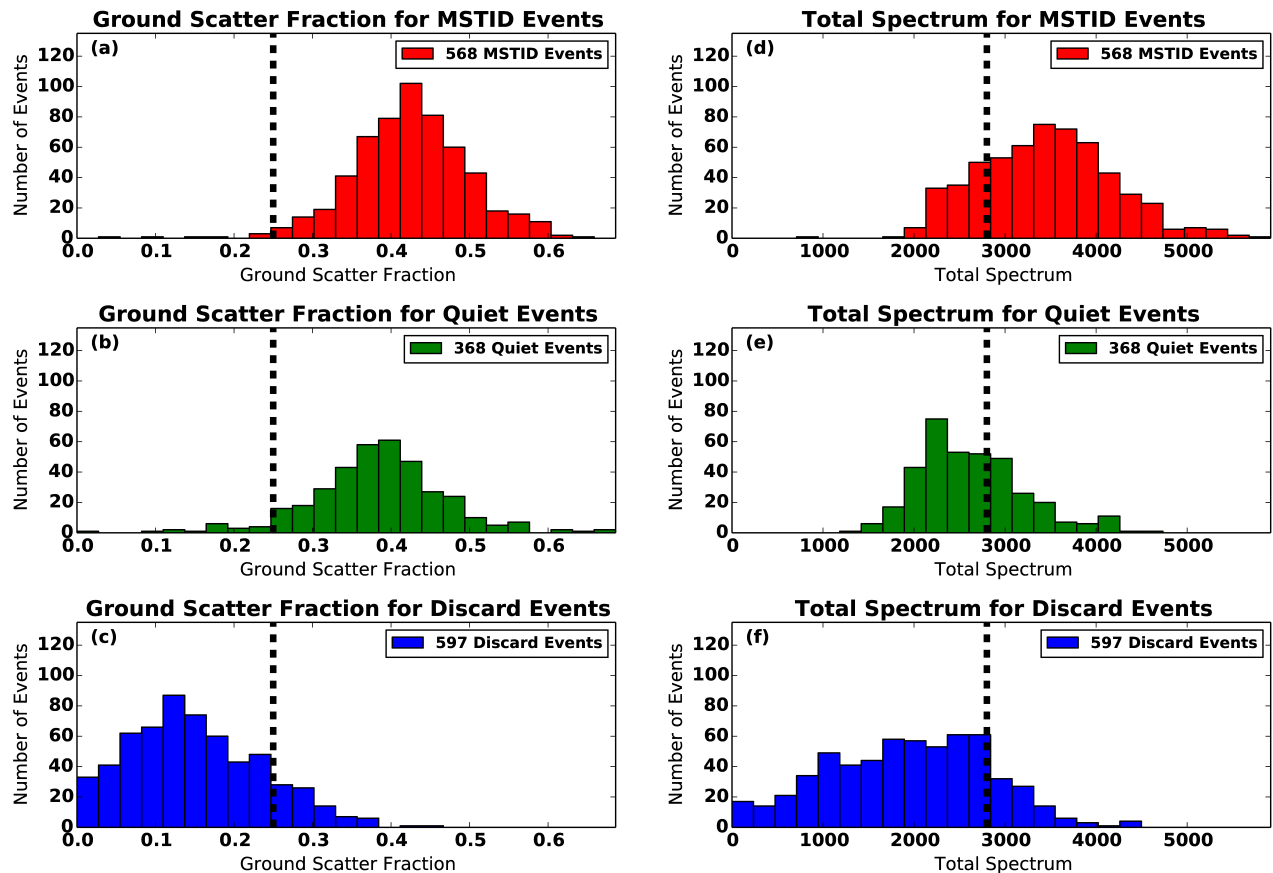


Figure 3.9: Distributions of the ground scatter fraction (left column) and total spectrum power (right column) for manually identified MSTID events, quiet events, and discard events. Vertical dashed lines in each plot show the threshold values used to reclassify the events in an automated manner. Events with a ground scatter fraction < 0.25 are moved to the discard category. The remaining events are then reclassified as “MSTID events” if the total spectrum parameter ≥ 2800 and “quiet events” if the total spectrum is less than this threshold. See Section 3.3.2 for details.

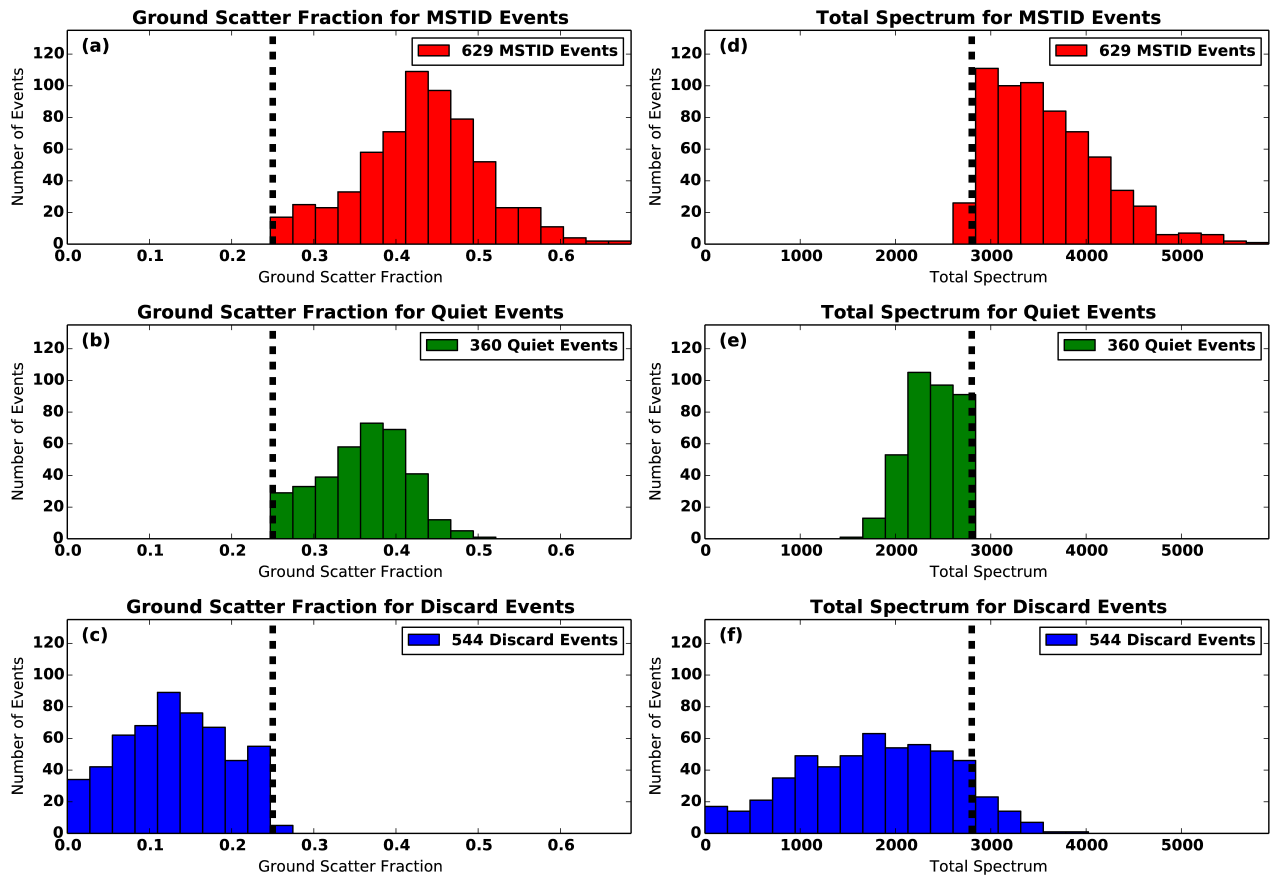


Figure 3.10: Distributions of the ground scatter fraction (left column) and total spectrum (right column) for study events after the automatic classification criteria have been applied. See Section 3.3.2 for details.

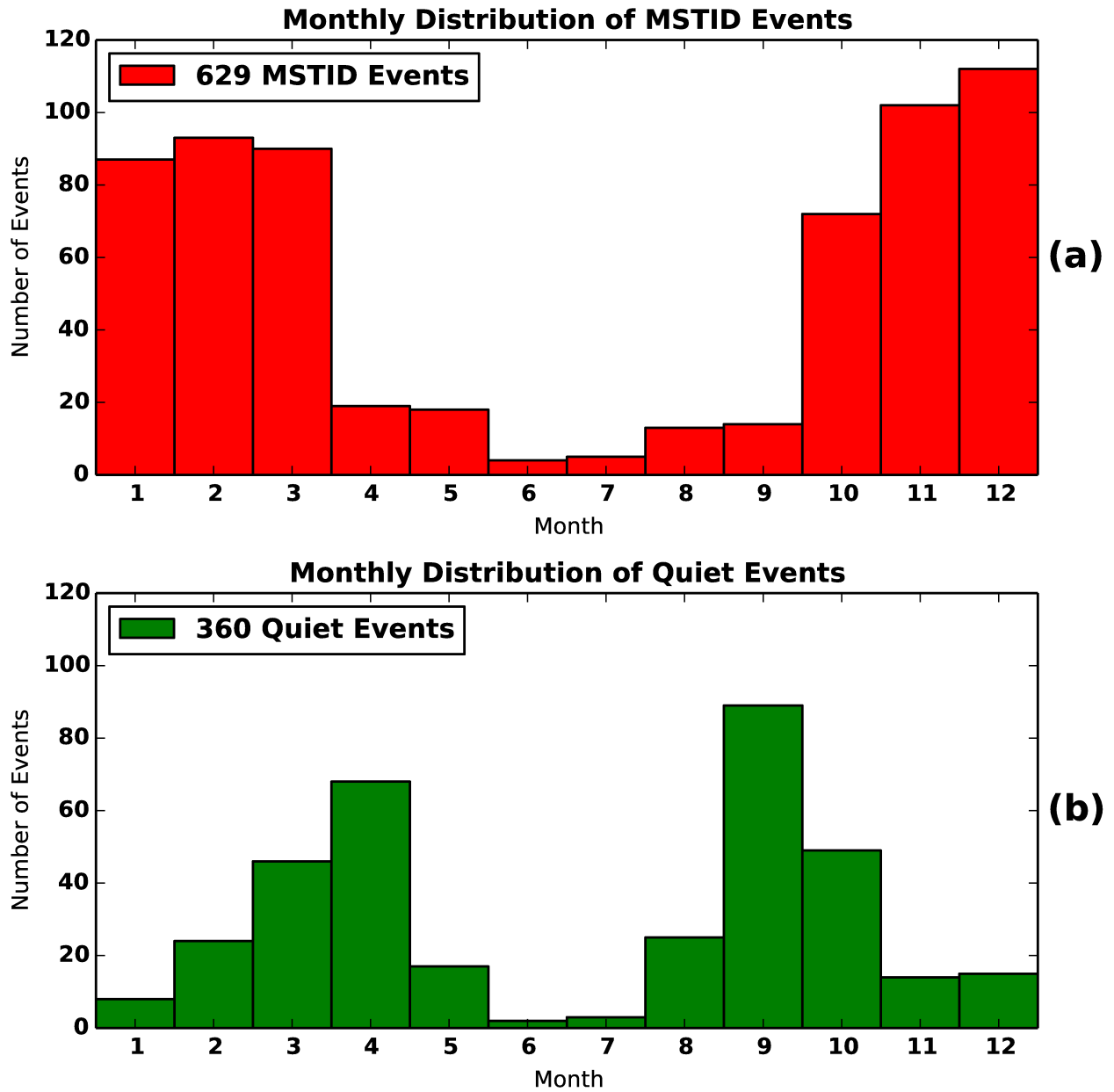


Figure 3.11: Occurrence distributions for BKS radar from 1 June 2010 to 31 May 2011 from 0800 to 1700 MLT (i.e. daylight conditions) for (a) MSTID periods, and (b) Quiet periods (good ground scatter without MSTIDs).

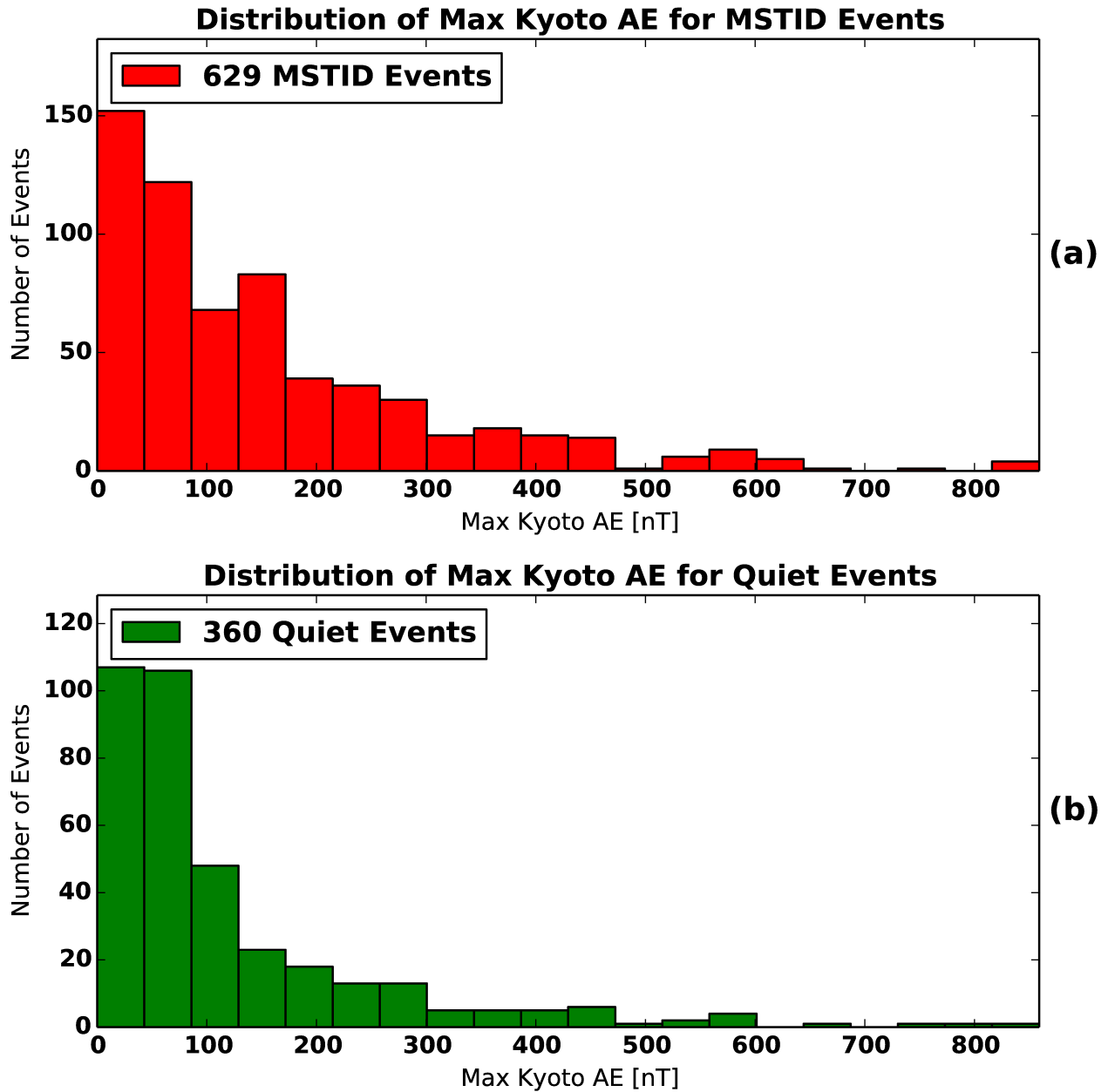


Figure 3.12: Auroral Electrojet (AE) distributions for BKS radar from 1 June 2010 to 31 May 2011 between 0800 and 1700 MLT (i.e. daylight conditions) for (a) MSTID periods, and (b) Quiet periods (good ground scatter without MSTIDs).

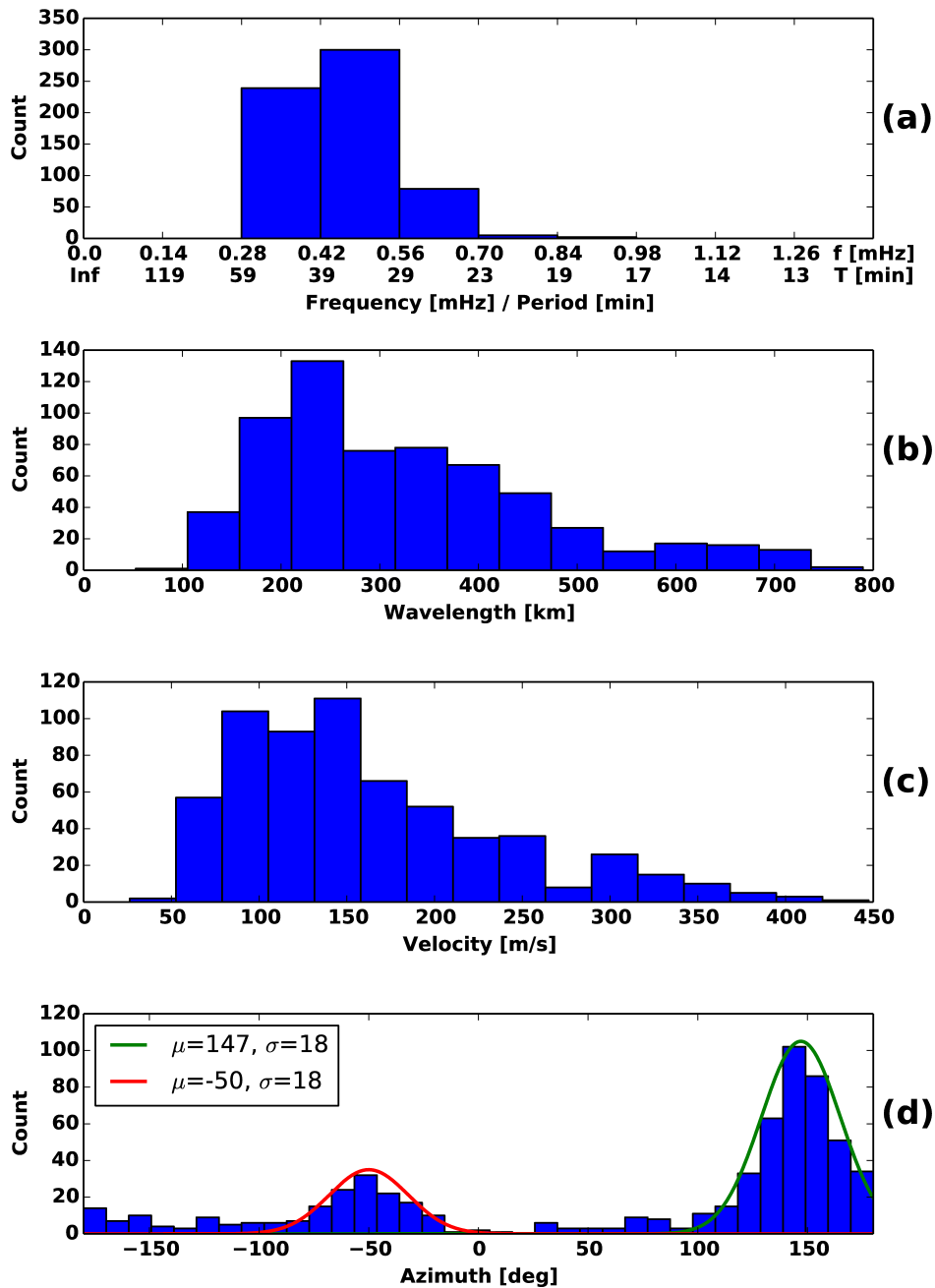


Figure 3.13: MSTID parameter distributions computed using the MUSIC analysis for BKS radar from 1 June 2010 to 31 May 2011 from 0800 to 1700 MLT (i.e. daylight hours) showing (a) frequency and period, (b) horizontal wavelength, (c) horizontal velocity, and (d) azimuth relative to geographic North.

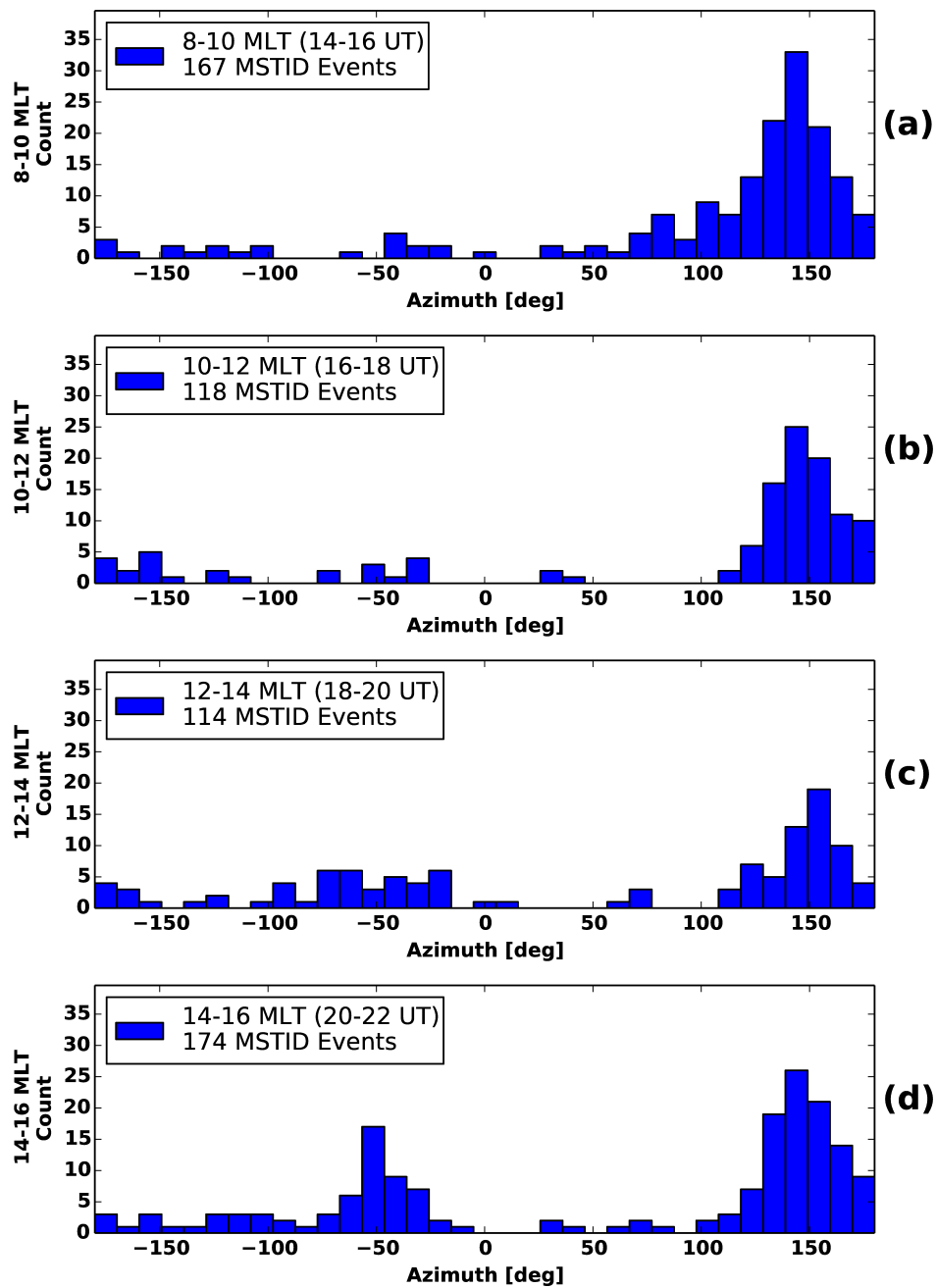


Figure 3.14: Magnetic local time (MLT) bins of MSTID geographic azimuth for BKS radar from 1 June 2010 to 31 May 2011 from 0800 to 1600 MLT. The dominant population (centered at $\sim 150^\circ$) decreases with MLT, while the secondary population (centered at $\sim -50^\circ$) appears in the afternoon. The MLT bins shown are: (a) 08-10 MLT, (b) 10-12 MLT, (c) 12-14 MLT, and (d) 14-16 MLT.

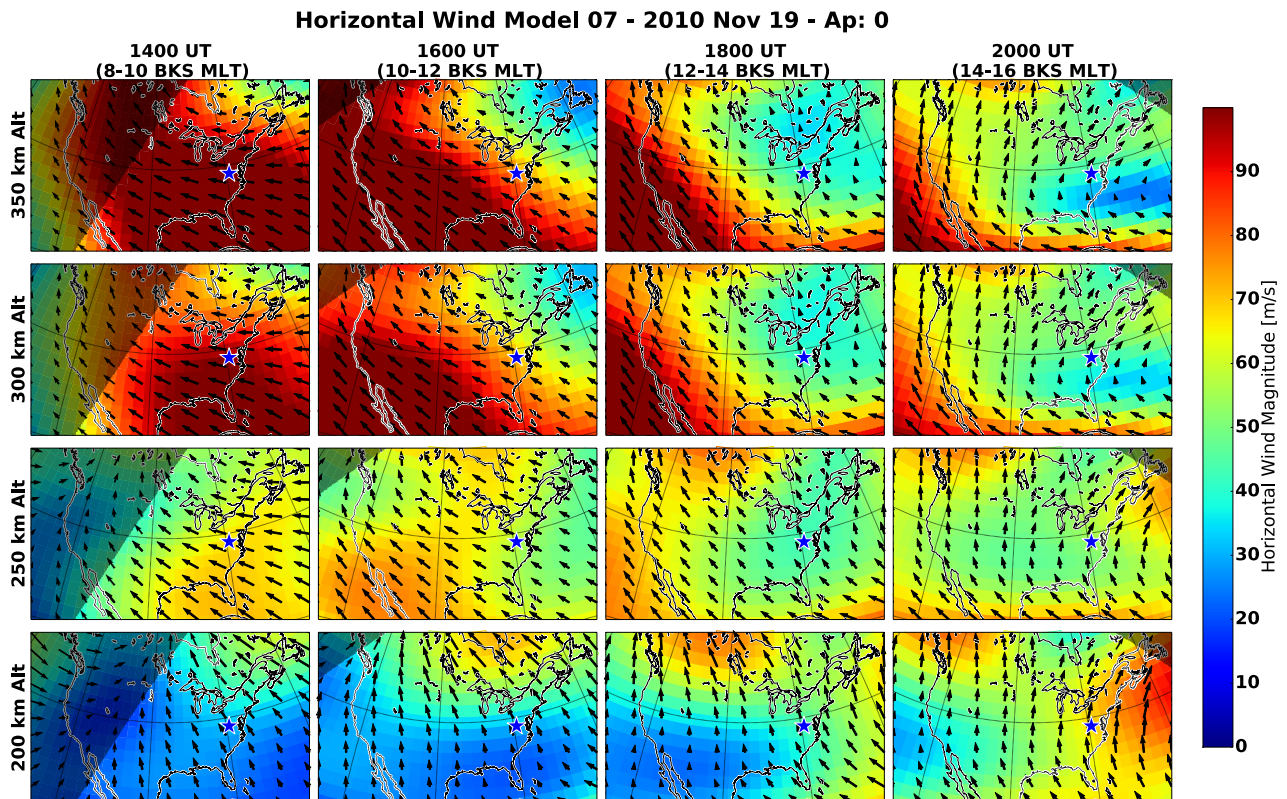


Figure 3.15: Results from a run of the Horizontal Wind Model 2007 on 19 November 2010 for undisturbed conditions ($A_p = 0$). This array of maps shows the magnitude and direction of the horizontal winds for altitudes from 200-350 km and times that correspond with the MLT time bins presented in Figure 3.14. The blue star indicates the center of the BKS MSTID observation region. The northwest-heading MSTID population in Figure 3.14 only appears when the winds are not parallel to the MSTID propagation direction.

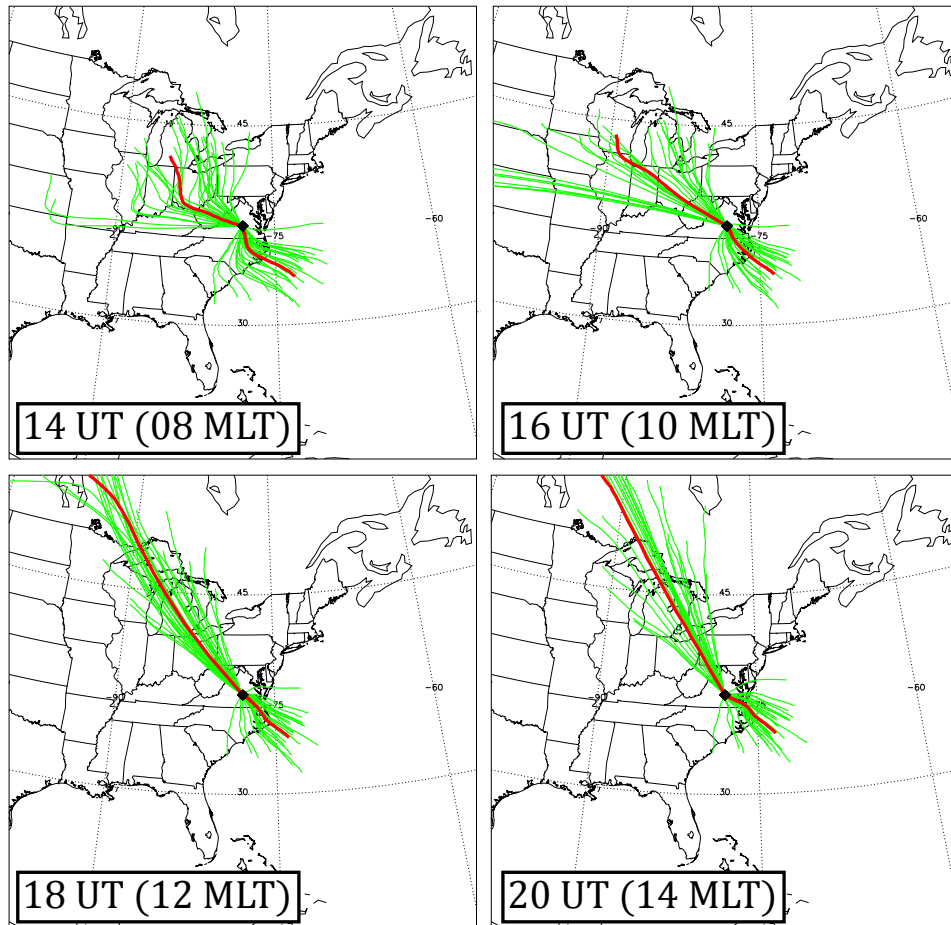


Figure 3.16: Results of the HINDGRATS reverse ray-tracing model on geographic maps using the climatology results summarized in Table 3.1 as gravity wave seed values. Waves were traced backward from the location of BKS (black diamond) at 220 km altitude. The red trace is the climatological mean, and the green traces are samples of perturbed wave structures. Model runs using yearly-averaged background atmospheres for 14, 16, 18, and 20 UT are shown. For each time, two separate model runs were conducted: the southeastward (dominant) MSTID population originates above the Great Lakes and Canada, and the northwestward (secondary) MSTID population originates over the Atlantic Ocean east of the Carolinas.

Chapter 4

Sources and Characteristics of Medium Scale Traveling Ionospheric Disturbances Observed by High Frequency Radars in the North American Sector

N. A. Frissell¹, J. B. H. Baker¹, J. M. Ruohoniemi¹, R. A. Greenwald¹, A. J. Gerrard², E. S. Miller³, and M. L. West⁴,

¹Bradley Department of Electrical and Computer Engineering, Virginia Tech, Blacksburg, Virginia, USA.

²The Center for Solar-Terrestrial Research, New Jersey Institute of Technology, Newark, New Jersey, USA.

³The Johns Hopkins University Applied Physics Laboratory, Laurel, Maryland, USA.

⁴Montclair State University, Montclair, New Jersey, USA.

Published as:

Frissell, N. A., J. B. H. Baker, J. M. Ruohoniemi, R. A. Greenwald, A. J. Gerrard, E. S. Miller, and M. L. West (2016), Sources and characteristics of medium-scale traveling ionospheric disturbances observed by high-frequency radars in the North American sector, *J. Geophys. Res. Space Physics*, 121, doi:10.1002/2015JA022168.

Abstract

Medium Scale Traveling Ionospheric Disturbances (MSTIDs) are wave-like ionospheric perturbations routinely observed by high frequency radars. We focus on a class of MSTIDs observed during the winter daytime at high and mid latitudes. The source of these MSTIDs remains uncertain, with the two primary candidates being space weather and lower atmospheric processes. We surveyed observations from four high latitude and six mid latitude SuperDARN radars in the North American sector from November through May of 2012 to 2015. The MSTIDs observed have horizontal wavelengths between ~ 150 to 650 km and horizontal velocities between ~ 75 to 325 m s⁻¹. In local fall and winter seasons the majority of MSTIDs propagated equatorward, with bearings ranging from $\sim 125^\circ$ to 225° geographic azimuth. No clear correlation with space weather activity as parameterized by *AE* and Sym-H could be identified. Rather, MSTID observations were found to have a strong correlation with polar vortex dynamics on two timescales. First, a seasonal timescale follows the annual development and decay of the polar vortex. Second, a shorter 2–4 week timescale again corresponds to synoptic polar vortex variability, including stratospheric warmings. Additionally, statistical analysis shows MSTIDs are more likely during periods of strong polar vortex. Direct comparison of the MSTID observations with stratospheric zonal winds suggests a wind filtering mechanism may be responsible for the strong correlation. Collectively, these observations suggest that polar atmospheric processes, rather than space weather activity, are primarily responsible for controlling the occurrence of high and mid latitude winter daytime MSTIDs.

4.1 Introduction

Medium Scale Traveling Ionospheric Disturbances (MSTIDs) are quasi-periodic enhancements and depletions of ionospheric electron densities. They typically have periods of 15–60 minutes, horizontal wavelengths of several hundred kilometers, and horizontal phase speeds of less than approximately 300 m s^{-1} [e.g., *Ogawa et al.*, 1987; *Samson et al.*, 1990]. Although some MSTIDs are associated with electrodynamic processes [e.g., *Kelley*, 2011; *Miller et al.*, 2014], this paper is concerned with MSTIDs that are associated with atmospheric gravity waves (AGWs) [e.g., *Hines*, 1960; *Yeh and Liu*, 1974; *Hunsucker*, 1982; *Hocke and Schlegel*, 1996]. MSTIDs have been extensively studied in both the high and mid latitude regions [e.g., *Evans et al.*, 1983; *Waldock and Jones*, 1986; *Ogawa et al.*, 1987; *Samson et al.*, 1989, 1990; *Bristow et al.*, 1994, 1996; *Kotake et al.*, 2007; *Ishida et al.*, 2008; *Hernández-Pajares et al.*, 2012; *Grocott et al.*, 2013; *Frissell et al.*, 2014b]. All of these studies report the same general results for both latitudinal regions, specifically that MSTID activity peaks in the fall and winter and minimizes in the summer, and that the majority of MSTIDs propagate toward the equator.

The source of these climatological MSTIDs remains an open question. The dominant equatorward MSTID propagation direction reported in previous studies suggests a high latitude source for the majority of MSTIDs. Numerous high latitude HF radar studies [*Samson et al.*, 1989, 1990; *Bristow et al.*, 1994, 1996; *Bristow and Greenwald*, 1996] favor a mechanism whereby AGWs generated by space weather and auroral sources couple with the ionosphere to create the MSTIDs [*Chimonas and Hines*, 1970; *Francis*, 1974]. However, these studies also note that there is a high probability of MSTID observation during geomagnetically quiet periods, and state that AGWs from tropospheric sources may also contribute to MSTID observations.

Recently, the Super Dual Auroral Radar Network (SuperDARN) of HF radars has expanded

equatorward to mid latitudes [*Baker et al.*, 2007; *Frissell et al.*, 2011]. It was found that the mid latitude radars routinely observe MSTIDs similar to those seen at high latitudes, and the possibility of a common source for both latitudinal regions was introduced [*Ishida et al.*, 2008; *Grocott et al.*, 2013; *Frissell et al.*, 2014b]. Recent GPS-TEC studies, such as *Hernández-Pajares et al.* [2012], also present data that suggests high and mid latitude daytime MSTIDs share a common source. *Grocott et al.* [2013] and *Frissell et al.* [2014b], both of which used one year of data from single SuperDARN radars in the Southern and Northern hemispheres, respectively, found that both space weather and tropospheric sources potentially contribute to mid latitude MSTID populations. Previous mid latitude HF Doppler MSTID experiments such as that of *Waldock and Jones* [1987] found more support for tropospheric than space weather sources.

We therefore ask, “Are the majority of MSTIDs observed at high and mid latitudes driven externally by space weather, or internally by atmospheric processes?” To address this question, we use three years of observations from an extended network of SuperDARN HF radars providing broad coverage at mid and high latitudes over the North American continent. By applying spectral techniques, we have developed a robust method for detecting and quantifying MSTID activity for each radar, allowing us to compare MSTID activity levels with measurements representative of potential sources. Auroral and space weather activity are represented by the *AE* and *Sym-H* indices. Internal atmospheric processes are represented by polar-region tropospheric and stratospheric data, focusing on the polar vortex. The polar vortex jet is a well known source of AGW generation and filtering [*Wu and Waters*, 1996; *Whiteway et al.*, 1997; *Ern et al.*, 2004; *Gerrard et al.*, 2011].

The paper is organized as follows: Section 4.2 describes our method for observing and quantifying MSTID activity with SuperDARN radars, the indices used for characterizing space weather activity, and the data used for examining internal atmospheric processes.

Section 4.3.1 presents climatologies of our mid and high latitude MSTID observations, while Section 4.3.2 presents a time series of data to provide insight into the behavior of MSTIDs and candidate driving parameters. The relationships identified here are then quantified using correlation and statistical analyses in Section 4.3.3. Section 4.3.4 provides a closer comparison of MSTID observations with lower and middle atmospheric zonal winds and temperatures. Section 4.4 discusses our findings, including the relative importance of space weather and polar vortex activity on MSTID occurrence. Finally, we summarize our work in Section 4.5.

4.2 Datasets and Methodology

4.2.1 SuperDARN

The Super Dual Auroral Radar Network (SuperDARN) is a network of high frequency (HF, 8–20 MHz) radars designed to probe the Earth’s ionosphere and its relationship to space [Greenwald *et al.*, 1995; Chisham *et al.*, 2007]. Although the network was originally constructed to image the high latitude auroral zone, it has recently been expanded to middle latitudes [Baker *et al.*, 2007; Frissell *et al.*, 2011]. Due to the ionospheric refraction of HF radio waves, these radars can image MSTIDs through a process illustrated in Figure 4.1. Figure 4.1a shows the Field-of-View (FOV) of the Fort Hays East (FHE) SuperDARN radar superimposed on a 250 km altitude cut of the International Reference Ionosphere (IRI) [Bilitza *et al.*, 2011]. The IRI has been perturbed with a MSTID modeled as a sinusoidal disturbance with a point source in the Arctic polar region. FHE Beam 7 is outlined in bold. Figure 4.1b shows the results of ray-tracing the signals from the radar when transmitted at 14.5 MHz [Coleman, 1998; de Larquier *et al.*, 2013] through the perturbed IRI along Beam 7. Rays are traced between 5° and 60° elevation angle with a 0.1° step (but plotted with a

1° step). This panel includes rays that are returned to Earth due to vertical gradients in the bottomside F-region ionosphere (approximately 150 to 250 km altitude) that create a signature known as F-region ground scatter (GS). Finally, Figure 4.1c shows the simulated FHE Beam 7 radar data as the model MSTID progresses in time. Ray focusing caused by the MSTID creates enhancements in the F-region GS power at certain ranges visible as increased concentrations of the gray lines at the Earth's surface, roughly at 1000 and 1800 km ground range. As the MSTID moves through the radar FOV, the region of enhanced GS power also moves in range. This equatorward moving MSTID generates the negatively sloped GS signature seen in the Range-Time-Intensity (RTI) plot of Figure 4.1c. The period of $T = 40$ min can be obtained almost by visual inspection of the RTI plot. Because we are interested in the MSTID at its location in the ionosphere, rather than the location of the scatter on the ground, a ground scatter range mapping has been applied to the data in Figure 4.1c and the subsequent calculations in this paper. This mapping is discussed in detail by *Bristow et al.* [1994] and Section 2.1 of *Frissell et al.* [2014b].

Figure 4.2 shows the GS-mapped FOVs of the radars selected for this study. The data shown is representative of a wintertime MSTID-active period and was collected on 21 Dec 2012. Bright regions (reds and yellows) at near ranges show the GS focusing region that is modulated by the MSTIDs. Individual wavefronts are especially prominent in the FHE and BKS data. For this study, ten radars appropriate to MSTID observations were selected in total: PGR, SAS, KAP, and GBR in the high latitudes, and CVW, CVE, FHW, FHE, BKS, and WAL in the mid latitudes. Table 4.1 provides the names, locations, and principal investigator institutions for each radar. This selection of radars provides excellent coverage over the entire North American continent and allows for continuity of observations between latitudinal regions. SuperDARN radars can only image MSTIDs using the GS technique described above when the ionospheric conditions allow for the observation of adequate F-region ground scatter.

This occurs primarily during daylight hours in the fall and winter months [Frissell *et al.*, 2014b]. Therefore, this study only used data from 1 November through 30 April collected during daylight hours, which is approximately 14 to 22 UT for the North American continent. We analyzed three observational seasons of high-quality MSTID data, beginning in November 2012 and ending in April 2015.

Figure 4.3 shows representative examples of MSTID-active and MSTID-quiet data, presented in the same RTI format as Figure 4.1c. Figure 4.3a shows 8 hours of data during a MSTID-active day on 21 Dec 2012, while Figure 4.3b shows data during a MSTID-quiet day on 19 Jan 2013. Both sets of data are from FHE Beam 7. Throughout the MSTID-active day, negatively-sloped GS power enhancements can be seen indicative of MSTIDs moving toward the radar. Slanted, dashed lines have been drawn to highlight selected wavefronts. In contrast, the MSTID-quiet day of Figure 4.3b shows the GS band remaining centered at approximately 500 km range throughout the entire day following sunrise. Some MSTID activity is observable, but it is at a significantly lower level and coherent wavetrains are not easily seen compared to Figure 4.3a. In order to describe MSTID occurrence across extended periods of observations, we have divided each day into two-hour sampling windows: 14–16, 16–18, 18–20, and 20–22 UT. These are indicated as a1–a4 and b1–b4. In Section 4.2.2, we describe the calculation of an MSTID Index that quantifies the level of MSTID activity within each sampling window. Later, the MSTID index will be compared with the indices of both space weather and polar vortex activity in order to identify which mechanism is primarily responsible for controlling the occurrence of the MSTIDs.

4.2.2 MSTID Index

The MSTID information collected by each radar is reduced into a MSTID Index for the purpose of estimating MSTID activity level and classifying sampling windows as MSTID-active or MSTID-quiet. Figure 4.4 illustrates this procedure using FHE 2012–2013 data. Each faint colored curve in Figure 4.4a represents the MSTID-band ($15 \leq T \leq 60$ min) spectrum of a 2-hour sampling window. The bold curves labeled a2–a4 and b2–b4 correspond to the sampling windows shown in Figure 4.3. Windows a1 and b1 were discarded due to their close proximity to the dawn terminator. The black, dashed curve shows the FHE 2012–2013 seasonal mean. The FHE MSTID Index is calculated for each sampling window by subtracting the mean curve and then integrating with respect to frequency. Sampling windows with an MSTID Index ≥ 0 are classified as MSTID-active periods and plotted in red. Sampling windows with an MSTID Index < 0 are classified as MSTID-quiet periods and plotted in blue. Figure 4.4b shows the MSTID Index time series for the FHE 2012–2013 observational season, which reveals several episodic features and significant temporal organization over long timescales. Specifically, the MSTID Index is not randomly distributed with time, but rather exhibits variations on both seasonal and multi-week time scales. These features will be discussed in detail in Section 4.3.2.

4.2.3 Space Weather Indices

To investigate the likelihood of MSTIDs being generated by space weather sources, we use both the Auroral Electrojet (*AE*) index and the Sym-H index. The *AE* index is a ground magnetometer measurement of magnetic perturbations produced by currents in the auroral zone [Davis and Sugiura, 1966]. We obtained the *AE* index from the Kyoto World Data Center for Geomagnetism (<http://wdc.kugi.kyoto-u.ac.jp/>). The Sym-H index is a mid

latitude ground magnetometer index that estimates the strength of geomagnetic storms and large-scale space weather activity [Iyemori, 1990; Dubyagin et al., 2014]. We obtained the Sym-H data via the OMNI dataset [King and Papitashvili, 2006] through the NASA Space Physics Data Facility (<http://spdf.gsfc.nasa.gov/>).

4.2.4 Neutral Atmospheric Data

In order to compare MSTID activity with internal atmospheric dynamics, we used geopotential, zonal wind, and temperature data from the European Centre for Medium-Range Weather Forecasts (ECMWF) Tropical Ocean and Global Atmosphere (TOGA) 2.5° Global Surface and Upper Air Analyses dataset [European Centre for Medium-Range Weather Forecasts, 1990]. Specifically, we focused our comparative analysis on the polar vortex, a large-scale, cyclonic wind system centered over the polar region [e.g. Schoeberl et al., 1992; Gerrard et al., 2002]. The polar vortex has its base in the upper troposphere and extends into the stratosphere, and vortex-associated dynamics are known to have an effect on thermospheric and ionospheric heights even at middle and low latitudes [Goncharenko et al., 2013; Pedatella and Liu, 2013]. The strength of the polar vortex may be measured by comparing geopotential data at the 1 and 10 mb pressure levels (approximately 50 and 30 km altitude, respectively) [Gerrard et al., 2002].

Geopotential can be approximated by the gravitational force times the height above mean sea level of a specified atmospheric pressure. Contours of geopotential Z at the 1 and 10 mb levels are presented in a time series of maps in Figure 4.5 that spans the 2012–2013 observing season for MSTIDs. The polar vortex is strong when the contours at both levels are well aligned, such as in November and December of 2012. The polar vortex is disrupted when the red and blue contours are not aligned, such as on 15 January 2013 and in April 2013.

To quantitatively estimate the strength of the polar vortex for the purposes of comparing with the MSTID Index, we define a Polar Vortex Index ζ as

$$\zeta = -\frac{\Sigma Z_r - E(\Sigma Z_r)}{\sigma(\Sigma Z_r)} \quad (4.1)$$

$$\Sigma Z_r = \sum_{180^\circ\text{E}}^{180^\circ\text{W}} \sum_{65^\circ\text{N}}^{90^\circ\text{N}} (Z_{1\text{ mb}} - Z_{10\text{ mb}})^2 \cdot \sin \phi_L \quad (4.2)$$

Here, $Z_{1\text{ mb}}$ and $Z_{10\text{ mb}}$ are the geopotentials at the 1 and 10 mb levels, while ϕ_L is the colatitude. E and σ are the seasonal expectation value and standard deviation operators, respectively. Larger positive values of ζ indicate more coherent polar vortex conditions, while larger negative numbers indicate a more disrupted polar vortex. The value of ζ associated with each time period presented in Figure 4.5 is printed in the upper right hand corner of each map.

4.3 Results

We now present the study results, beginning in Section 4.3.1 with a climatology of MSTIDs observed at both high and mid latitudes. In Section 4.3.2, we show a time series of the MSTID observations and candidate driving parameters. This section reveals long time-scale organization in both the MSTID Index and Polar Vortex Index that are not observable in the space weather indices. These relationships are then quantified in Section 4.3.3 using probability and lag correlation analyses. Finally, Section 4.3.4 directly compares the MSTID and Polar Vortex indices to tropospheric and stratospheric temperatures and zonal winds.

4.3.1 MSTID Climatology

Using the procedure described by *Frissell et al.* [2014b], we estimated the period, horizontal wavelength, and propagation azimuth for the strongest MSTID identified in each MSTID-active sampling window. Figures 4.6 and 4.7 show histograms generated from this analysis showing the overall MSTID climatology for high and mid latitudes, respectively. These results are summarized in Table 4.2. The red dashed line in Figures 4.6a and 4.7a show the transfer function magnitude of the filter used to select for the MSTID band. Additionally, all detected MSTIDs with horizontal wavelengths greater than 750 km were rejected, as is indicated by the red vertical dashed line in Figures 4.6b and 4.7b. This cutoff value was chosen for two reasons. First, MSTIDs are defined as having horizontal wavelengths only up to several hundred km [*Ogawa et al.*, 1987]. Second, the detection algorithm employed determines λ_h as the inverse of the horizontal wavenumber ($2\pi/k$), which quickly approaches an infinite wavelength for small values of k .

In general, the high and mid latitude climatologies are very similar. Figures 4.6a and 4.7a show that the majority of MSTIDs at both high and mid latitudes have periods T between 30 and 40 min. Figure 4.6b shows the range of horizontal wavelengths for most high latitude MSTIDs is $150 \lesssim \lambda_h \lesssim 450$ km, while Figure 4.7b shows that the mid latitude distribution is shifted to somewhat longer wavelengths of $200 \lesssim \lambda_h \lesssim 650$ km. In Figures 4.6c and 4.7c, the majority of both high and mid latitude MSTID horizontal phase velocities fall in the range of $75 \lesssim v_p \lesssim 325$ m s⁻¹. However, a sharp decrease in high latitude MSTID counts appears at $v_p \gtrsim 175$ m s⁻¹. Finally, Figures 4.6d and 4.7d show that almost all observed MSTIDs at high and mid latitudes are traveling toward the equator with geographic azimuths in the range of approximately 125° to 225°.

4.3.2 Time Series of MSTIDs and Candidate Drivers

Figure 4.8 presents the time series of SuperDARN MSTID (Panels a–c), polar vortex (Panel d), and geomagnetic data (Panels e, f) for the 2012–2013 observational season. Each of these panels is explained in more detail below.

The top two panels, Figures 4.8a and 4.8b, show the MSTID Index for each sampling window for each radar broken into sets of high and mid latitude radars. Within each vertical 2-hour UT time bin of Figures 4.8a and 4.8b, the MSTID index from each of the radars is organized from West on the bottom to East on the top. Red colors indicate MSTID-active periods, while blue colors indicate MSTID-quiet periods. Gray squares represent missing data.

Figure 4.8c presents a reduction of the MSTID data shown in Figures 4.8a and 4.8b. The light gray and solid blue lines show the “Continental MSTID Index”, which is computed by averaging the MSTID indices for all radars on a given day and computing the standard z -score based on the mean and standard deviation of the season. The light gray line is the raw data, and the blue line is a smoothed, 4-day running average. A data quality parameter, the number of good sampling windows per day (n Data Points), is plotted as a dotted line on the same panel. A daily MSTID Score is derived from the number of MSTID-active and MSTID-quiet periods observed on a given day. This is plotted in the background of Figure 4.8c, with MSTID-active days (MSTID Score > 0) in red and MSTID-quiet days (MSTID Score ≤ 0) in blue.

Figures 4.8d, 4.8e, and 4.8f show the time series of the Polar Vortex, AE , and Sym-H indices, respectively. These data sets have been described in Sections 4.2.3 and 4.2.4. In each panel, the light gray line shows the raw data and the solid blue line shows a smoothed, 4-day running mean. The smoothed data will be used in a correlation analysis in Section 4.3.3.

Visual inspection of Figure 4.8 reveals a number of important insights into the data. From

the top two panels, Figures 4.8a and 4.8b, it is evident that the high and mid latitude radars see increases and decreases in MSTID activity together. Also, MSTID activity is relatively constant across all radars in each UT time bin, suggesting MSTID activity is not strongly dependent on longitude and local time.

Two major timescales can be observed in the MSTID data of Figures 4.8a–4.8c. First, there is a seasonal timescale. From November through mid-January, the average MSTID activity level is high. From mid-January until the end of the observational season on 30 April, the average level of MSTID activity is distinctly lower. Second, a multi-week timescale is also present. Events typically last about 2 to 4 weeks and appear to be aperiodic. For example, periods of enhanced MSTID activity occur from 15 Nov to 6 Dec 2012, from 15 Dec 2012 to 7 Jan 2013, and from 1 Feb to 1 Mar 2013. Conversely, clear depressions of MSTID activity are observed from 7–14 Dec 2012, and 8–30 Jan 2013. The January 2013 depression is especially prominent, reaching a minimum on 20–21 Jan 2013.

Figure 4.8d shows that the seasonal and multi-week timescales present in the MSTID Index are also visible in the Polar Vortex Index. The Polar Vortex Index is mostly above average from November through February, and then tapers to low values by the end of the season. The mid-January depression that was prominent in the MSTID Index is again a prominent feature of the Polar Vortex Index, although shifted in time. Following this depression, both the MSTID Index and Polar Vortex Index recover together from 24 Jan to 1 Mar 2013. Additionally, small depressions can be seen in the Polar Vortex Index from 4–14 Dec 2012 that may correspond to the reduction in MSTIDs around the same time. Overall, the Polar Vortex Index appears to lead the MSTID Index by approximately 1 to 2 weeks.

By contrast, a clear correlation between MSTID activity and the indices of space weather activity cannot be observed. The *AE* index of Figure 4.8e and the Sym-H index of Figure 4.8f do not show evidence of either the seasonal or multi-week timescales present in both

the Continental MSTID Index or the Polar Vortex Index. The raw data shown by the black traces indicates that space weather activity is impulsive and occurs on time scales of hours to days. The blue 4-day running mean smooths the *AE* and Sym-H data to time scales similar to that of the MSTID and Polar Vortex indices. When high levels of activity occur simultaneously in *AE* and Sym-H (generally large positive values of *AE* and positive values followed by large negative values in Sym-H), a decrease in valid radar observations and hence the *n* Data Points quality parameter (Figure 4.8c, dashed line) can be observed. Examples of this include the days around 13 Nov 2012, 25 Jan 2013, 1 Mar 2013, and 17 Mar 2013. This is not unexpected, as geomagnetic storms are known to disrupt HF radio wave propagation. However, these disruptions do not typically have a strong effect on the Continental MSTID Index. Furthermore, it is worth noting that MSTID activity is observed to be high during periods of both high (e.g., 12–24 Nov 2012; 15–23 Dec 2012) and low (e.g., 25 Dec 2012 to 6 Jan 2013) space weather activity.

To summarize this section, the 2012–2013 time series presented in Figure 4.8 illustrates a number of trends. First, changes in MSTID activity levels are seen collectively by high and mid latitude radars at all longitudes across North America. Namely, the MSTID activity levels are high and relatively stable from November through the beginning of January, but steadily decrease from mid-January through the end of the observing season on 30 April. In addition to this seasonal trend, shorter, multi-week events also occur. The most notable of these events occurs in Jan 2013. These same trends can also be observed in the Polar Vortex Index, but not in the *AE* and Sym-H space weather indices. Rather, these indices have the strongest effect on the number of valid radar observations, and not on MSTID activity levels. These trends can also be observed in the 2013–2014 and 2014–2015 time series, which are available in the supplemental material to this paper.

4.3.3 Probability and Correlation Analysis

The time series presented in Section 4.3.2 suggests that atmospheric processes represented by the Polar Vortex Index are more closely associated with MSTID activity than the space weather processes represented by the AE and Sym-H indices. In this section, we further quantify these relationships.

Figure 4.9 shows the statistical dependence of MSTID observations on the AE , Sym-H, and Polar Vortex indices using data from all radars and all three observational seasons. Conditional probability density functions were calculated for both MSTID-active (red curves) and MSTID-quiet (blue curves) days as a function of each possible driver index. For the AE and Sym-H indices, there is only a small difference between the MSTID-active and MSTID-quiet distributions at low levels of geomagnetic activity, and almost no difference at moderately disturbed and disturbed levels. However, Figure 4.9c shows clear differences between the MSTID-active and MSTID-quiet distributions for the Polar Vortex Index such that MSTID-active days are more probable when the Polar Vortex index $\zeta > 0$, while MSTID-quiet days are somewhat more probable when the Polar Vortex index $\zeta < 0$.

Next, we conducted a time-lagged correlation analysis between the Continental MSTID Index and the Polar Vortex, AE , and Sym-H indices. Again, we used data from all ten radars and all three observational seasons. These results are presented in Figure 4.10a, which shows correlation coefficients represented by solid lines. Dashed lines indicating the 95% confidence interval as determined by a Monte Carlo technique using $S = 2000$ resamples. Positive lag values indicate the number of days in which the Continental MSTID index lags the tested parameter. Stars indicate the strongest correlation value and appropriate lag time. Figure 4.10a shows that the Polar Vortex index (red line) is the most highly correlated of the three parameters, with a maximum correlation of $R \approx 0.7$ at a lag of 12 days. AE and Sym-H

both have maximum correlation coefficients of $|R| \approx 0.3$ with a lag of 1 to 2 days. The AE and Sym-H indices have similar correlation magnitudes, but opposite signs. This is expected as both parameters are measures of space weather activity, but AE becomes more positive during disturbed times, while Sym-H generally becomes more negative.

In order to test whether the correlation coefficients calculated in Figure 4.10a were affected by the quality of radar observations, we also performed the lagged correlation analysis of the test parameters with the n Data Points quality parameter (introduced in Figure 4.8c, dashed line). These results, shown in Figure 4.10b, show that the Polar Vortex Index has $|R| \lesssim 0.2$ correlation with n Data Points at all lags. However, both AE and Sym-H have maximum $|R| \approx 0.3$ at lags of 0 to 1 days. This suggests that the AE and Sym-H correlations with the MSTID Index identified in Figure 4.10a are more likely due to geomagnetic activity disrupting HF radar propagation than an actual change in the amount of MSTIDs observed. To ensure the validity of these correlation results, we repeated the analysis using varying types and amounts of smoothing. We applied rolling mean and rolling median smoothing windows of 1 to 5 days in 1 day steps for each of the AE , Sym-H, and Polar Vortex indices. Each of these tests were consistent with the results of Figure 4.10.

4.3.4 Comparison with the Lower and Middle Atmosphere

Sections 4.3.2 and 4.3.3 have presented evidence pointing to a strong connection between the processes that drive the stratospheric geopotential-derived Polar Vortex Index and the MSTID observations made by North American SuperDARN radars. Three interesting features have come from this analysis. First, both the Continental MSTID Index and the Polar Vortex Index demonstrate a seasonal behavior in which values are high and quasi-constant in the late fall, but decline as winter turns to spring. Second, both datasets show evidence of

related episodic events that occur on timescales of approximately two to four weeks. Finally, variations of the MSTID observations lag the Polar Vortex Index by approximately one to two weeks. In this section, we analyze the Continental MSTID Index and the Polar Vortex Index in conjunction with lower and middle atmospheric wind and temperature data to investigate these three features in more detail.

Figure 4.11 presents altitude profiles (0–45 km) of zonally averaged temperatures poleward of 60° N for all three MSTID observational seasons from 2012 to 2015. This data comes from the ECMWF dataset described in Section 4.2.4. The Continental MSTID Index is superposed as a bold, black line and the Polar Vortex Index is superposed as a dotted line. A dashed line marks the winter solstice of each year (i.e. December 21st). It can be seen that the Polar Vortex Index is a good 1-dimensional proxy for the average intensity of the 2-dimensional temperature contours of each of the three years. That is, stable vortex conditions occur when stratospheric temperatures are cold, but when the polar vortex is disrupted there is warming observed in the lower stratosphere. This accounts for both the seasonal and multi-week timescales of the Polar Vortex Index. More specifically, Figure 4.11 shows that the atmospheric temperature profile is relatively constant with respect to time prior to the winter solstice, as is the Polar Vortex Index. Following solstice, the atmosphere warms from the top down due to the steady downward residual circulation and adiabatic compression of air [Meriwether and Gerrard, 2004]. Eventually, spring heating leads to gradual polar vortex breakdown. Each year, especially following winter solstice, short timescale warmings of the stratosphere occur that are the cause of the short-term variability in the Polar Vortex Index, as discussed as “subtle vortex motion” in Gerrard *et al.* [2002]. The most dramatic event in Figure 4.11 is the Sudden Stratospheric Warming (SSW) of January 2013, but smaller warmings (e.g., Jan–Apr 2014) are also observed to contribute to Polar Vortex Index variability. Figure 4.11 reveals that the Continental MSTID Index, like the Polar Vortex

Index, also conforms with the major trends in atmospheric temperature.

Ultimately, the temperature variations of Figure 4.11 are directly related to changes in the atmospheric winds. Figure 4.12 presents the zonal wind counterpart to Figure 4.11 with eastward winds in red and westward winds in blue. Again, the Continental MSTID Index is shown as a solid black line, while the Polar Vortex Index is indicated by a dotted line. Figure 4.12 offers an explanation for the observed delay between the MSTID Index and the Polar Vortex Index, as the change in zonal wind direction better corresponds to variability in the MSTID observations. This is suggestive of a critical-level filtering mechanism of a preexisting lower atmospheric AGW spectrum [e.g. *Lindzen, 1981; de Wit et al., 2014*]. The MSTID Index is observed to decrease as the lower stratospheric zonal winds slow from eastward and become more westward. The MSTID Index recovers as the winds return eastward. Arrows have been added to Figure 4.12 to highlight specific examples of this behavior. The most dramatic events occur during Dec 2012, Jan 2013, and Jan 2015, when winds change direction from the stratosphere all the way to the ground. However, numerous weaker cases may also be observed in this figure, such as in Feb to Apr of both 2014 and 2015. In some of these cases, a gentle slowing of the eastward winds appears to cause a depression in the amount of observed MSTIDs.

4.4 Discussion

In an effort to determine whether space weather activity or atmospheric processes account for the majority of mid and high latitude MSTIDs, we have examined HF radar MSTID observations along with indices representing space weather and middle atmospheric activity. Our findings are highly suggestive that a single large-scale mechanism is adequate for explaining the majority of MSTIDs at both mid and high latitudes. First, the climatologies

of Figures 4.6 and 4.7 show that both high and mid latitude MSTID populations have similar frequency, horizontal wavelength, horizontal phase velocity, and propagation heading distributions. Almost all MSTIDs travel equatorward, suggesting a polar source for both latitudinal regions. Although this is not sufficient to point to a single mechanism, the MSTID Index time series presented in Figures 4.8a and 4.8b provide more convincing evidence. MSTID activity enhancements and depressions are observed simultaneously in both the high latitude observations of Figure 4.8a and the mid latitude observations of Figure 4.8b. Furthermore, Figures 4.8a and 4.8b show coherence in a longitudinal sense as well. MSTID activity levels from the eastern part of the continent are typically similar to those simultaneously seen in the west. If the MSTIDs were controlled by localized mechanisms, we would not expect to see this level of coherence in either latitude or longitude. The suggestion of a single mechanism for both mid and high latitude MSTIDs is consistent with *Ishida et al.* [2008].

Numerous prior theoretical and observational MSTID studies at high latitudes have identified space weather activity as the primary generator of AGWs that couple to MSTIDs, even though a strong correlation with space weather indices was not found [e.g., *Francis*, 1974; *Samson et al.*, 1989, 1990; *Bristow et al.*, 1994; *Bristow and Greenwald*, 1996]. Very recent mid-latitude papers, including *Grocott et al.* [2013], *Frissell et al.* [2014b], and *Oinats et al.* [2016], also searched for links to space weather activity, but found a marginal association at best. Similarly, the present study does not find convincing evidence that space weather activity contributes significantly to MSTID occurrence. Figures 4.9 and 4.10 suggest that there is little relationship between the amount of MSTIDs observed and the level of geomagnetic activity.

On the other hand, MSTIDs have long been associated with AGWs, and the Polar Vortex jet is a region known for high levels of AGW activity. The jet consists of high velocity winds at the equatorward edge of the Polar Vortex, typically between about 55° – 70° latitude, a

region that is very close to the supposed auroral sources. Our analysis reveals that the Polar Vortex Index and the Continental MSTID Index are highly correlated and share two primary time scales. The first is a seasonal timescale, such that average MSTID activity is highest from November through January, and then decreases from February through the end of April. This seasonal time scale corresponds with a cool winter lower stratosphere and the annual, gradual lower stratospheric warming that starts at winter solstice and continues into spring. The second timescale is a multi-week timescale, which corresponds with episodic stratospheric warmings. For the polar vortex, this behavior is well known and understood. For MSTIDs, the seasonal behavior is also well known [e.g., *Bristow et al.*, 1996], but, to our knowledge, the collective episodic variations have not been previously reported.

The high correlation of the MSTID Index with the Polar Vortex Index suggests a number of possible mechanisms. One is that the vortex jet is a direct generator of the source AGWs, such as described by *Gerrard et al.* [2002]. On the other hand, the observed one to two week delay of the MSTID response to the Polar Vortex Index is puzzling. The relationship becomes more clear when MSTID observations are directly compared to stratospheric zonal winds, which show a decrease in the amount of MSTIDs as winds turn from eastward to westward. This suggests a scenario in which a preexisting lower-altitude AGW spectrum may be subjected to critical-level filtering that controls the amount of AGWs that reach the F-region ionosphere and couple to MSTIDs [*Lindzen*, 1981; *de Wit et al.*, 2014]. A filtering scenario would mean that although the middle atmospheric processes are controlling the amount of MSTIDs in the F-region ionosphere, AGW energy could still come from a number of different sources, possibly including the aurora.

4.5 Summary and Conclusions

We have surveyed observations from four high latitude and six mid latitude SuperDARN radars in the North American sector from November through May of 2012 to 2015. The MSTIDs observed have horizontal wavelengths between ~ 150 to 650 km and horizontal phase velocities between ~ 75 to 325 m s⁻¹. In local fall and winter seasons the majority of MSTIDs propagated equatorward, with bearings ranging from $\sim 125^\circ$ to 225° geographic azimuth. No clear correlation with space weather activity as parameterized by *AE* and Sym-H could be identified. Rather, MSTID observations were found to have a strong correlation with polar vortex dynamics on two timescales. First, a seasonal timescale follows the annual development and decay of the polar vortex. Second, a shorter 2–4 week timescale again corresponds to synoptic polar vortex variability, including stratospheric warmings. Additionally, statistical analysis shows MSTIDs are more likely during periods of strong polar vortex. Direct comparison of the MSTID observations with stratospheric zonal winds suggests a wind filtering mechanism may be responsible for the strong correlation, but the exact nature of this mechanism is beyond the scope of this paper. Collectively, these observations suggest that polar atmospheric processes, rather than space weather activity, are primarily responsible for controlling the occurrence of high and mid latitude winter daytime MSTIDs.

4.6 Acknowledgments

The Virginia Tech authors acknowledge the support of the NSF under grants AGS-1341918 and AGS-0838219. ESM acknowledges support from NSF AGS-1341885. SuperDARN data and analysis software is accessible through <http://vt.superdarn.org>. The *AE* index was obtained from the World Data Center in Kyoto. OMNI data was accessed through the

NASA Space Physics Data Facility. ECMWF data was provided by the National Center for Atmospheric Research Research Data Archive. We acknowledge the use of the Free Open Source Software projects used in this analysis: Ubuntu Linux, python, IPython, matplotlib, NumPy, SciPy, scikit-learn, and others. NAF thanks A. Kriz for helpful discussions.

	Code	Name	Geog. Lat. [°]	Geog. Long. [°]	Boresite [°]	PI Institution
High Latitude	GBR	Goose Bay	53.32	-60.46	65.0	Virginia Tech
	KAP	Kapuskasing	49.39	-82.32	12.0	Virginia Tech
	SAS	Saskatoon	52.16	-106.53	23.1	University of Saskatchewan
	PGR	Prince George	53.98	-122.59	-5.0	University of Saskatchewan
Middle Latitude	WAL	Wallops Island	37.93	-75.47	35.9	Johns Hopkins University APL
	BKS	Blackstone	37.10	-77.95	-40.0	Virginia Tech
	FHE	Fort Hays East	38.86	-99.39	45.0	Virginia Tech
	FHW	Fort Hays West	38.86	-99.39	-25.0	Virginia Tech
	CVW	Christmas Valley West	43.27	-120.36	54.0	Dartmouth College
	CVW	Christmas Valley East	43.27	-120.36	-20.0	Dartmouth College

Table 4.1: Details of SuperDARN radars used in MSTID study.

	High Latitude ($n = 304$)		Mid Latitude ($n = 1325$)	
	μ	σ	μ	σ
T [min]	30	155	33	170
λ_h [km]	333	134	397	142
v [m s ⁻¹]	181	84	201	82
Azm	174°	42°	168°	45°

Table 4.2: Mean μ and standard deviation σ of period, horizontal wavelength, horizontal phase velocity, and propagation azimuth for SuperDARN MSTID observations from 2012 through 2015. This table summarizes Figures 4.6 and 4.7.

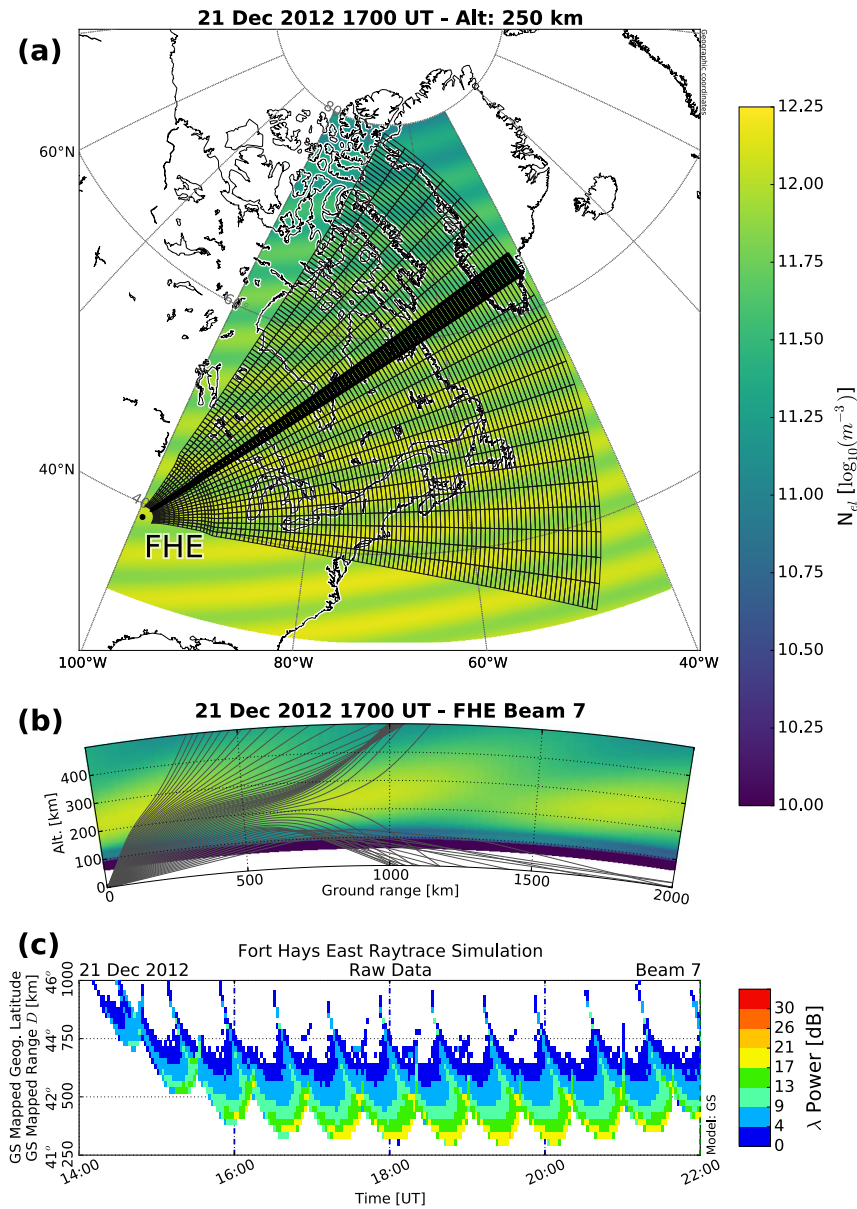


Figure 4.1: Raytrace simulation illustrating how SuperDARN HF radars observe MSTIDs. (a) Fort Hays East (FHE) radar field-of-view superimposed on a 250 km altitude cut of a perturbed IRI. FHE Beam 7 is outlined in bold. (b) Vertical profile of 14.5 MHz raytrace along FHE Beam 7. Background colors represent perturbed IRI electron densities. The areas where rays reach the ground are potential sources of backscatter. (c) Simulated FHE Beam 7 radar data, color-coded by radar backscatter power strength. Periodic, slanted traces with negative slopes are the signatures of MSTIDs moving toward the radar.

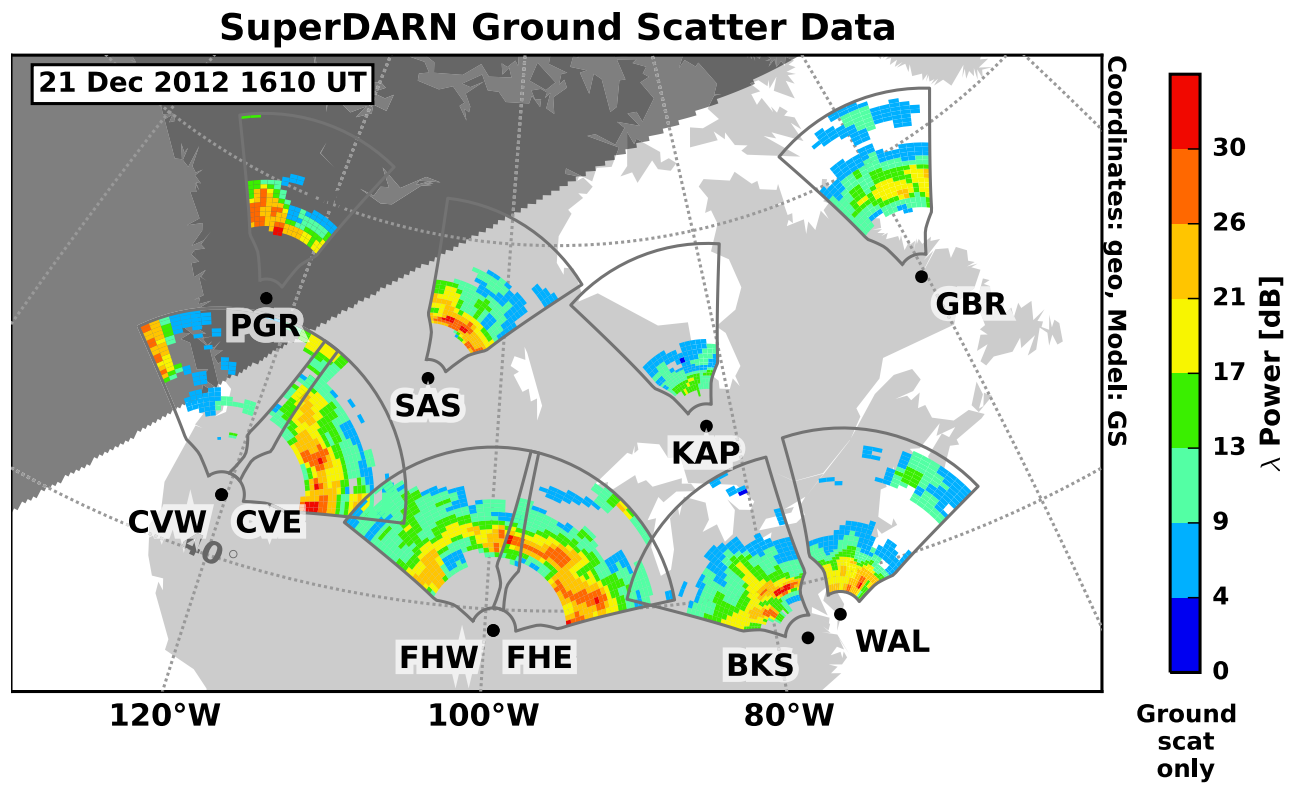


Figure 4.2: Ground scatter measurements during a MSTID-active period on 21 Dec 2012 obtained by the North American SuperDARN radars selected for this study. Radar field-of-views and data are plotted using a ground scatter mapping transformation.

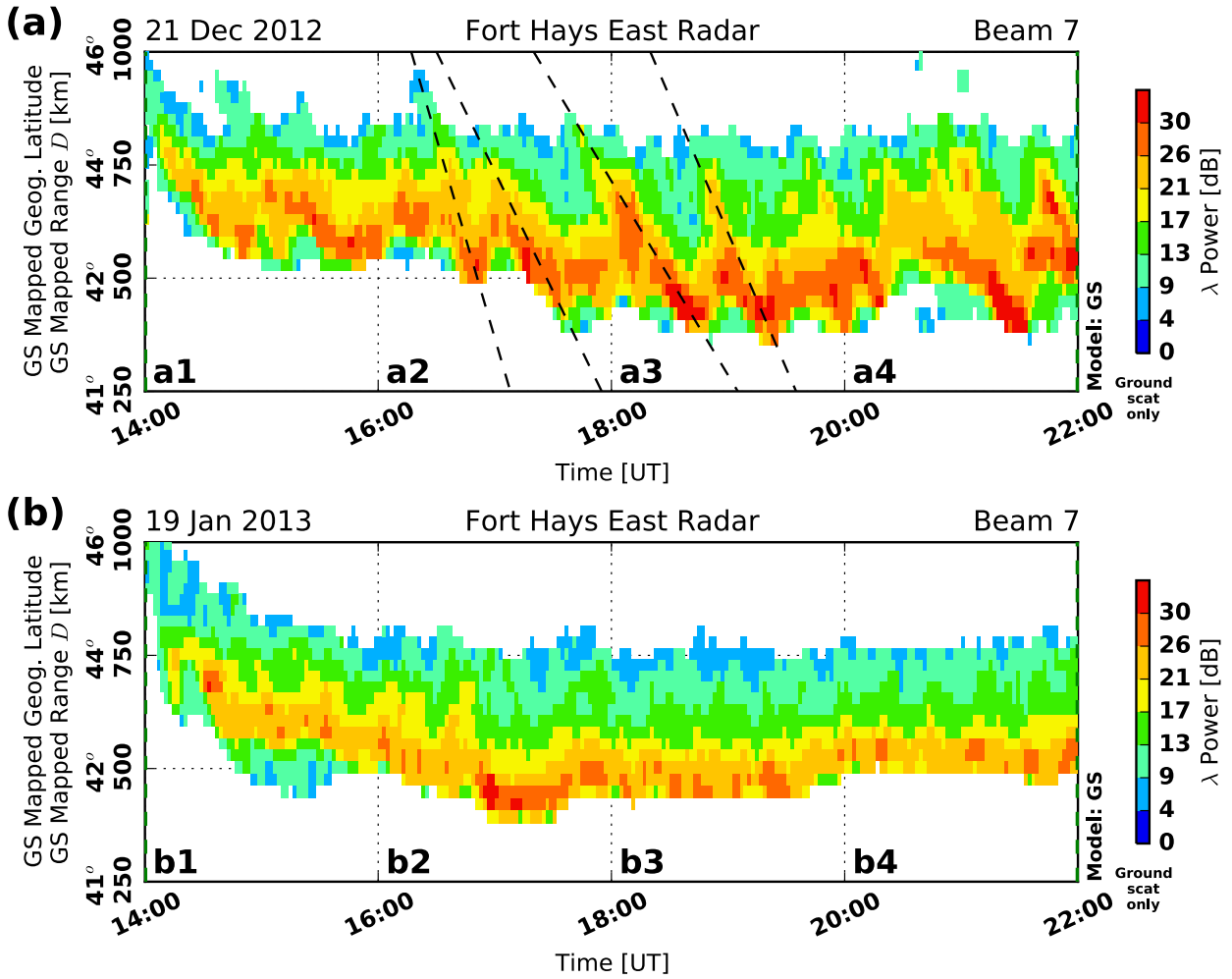


Figure 4.3: Range-Time-Intensity (RTI) plots from FHE Beam 7 for (a) a MSTID-active day, and (b) a MSTID-quiet day. Inclined dashed lines draw attention to selected MSTID signatures. Format is the same as that used in Figure 4.1c.

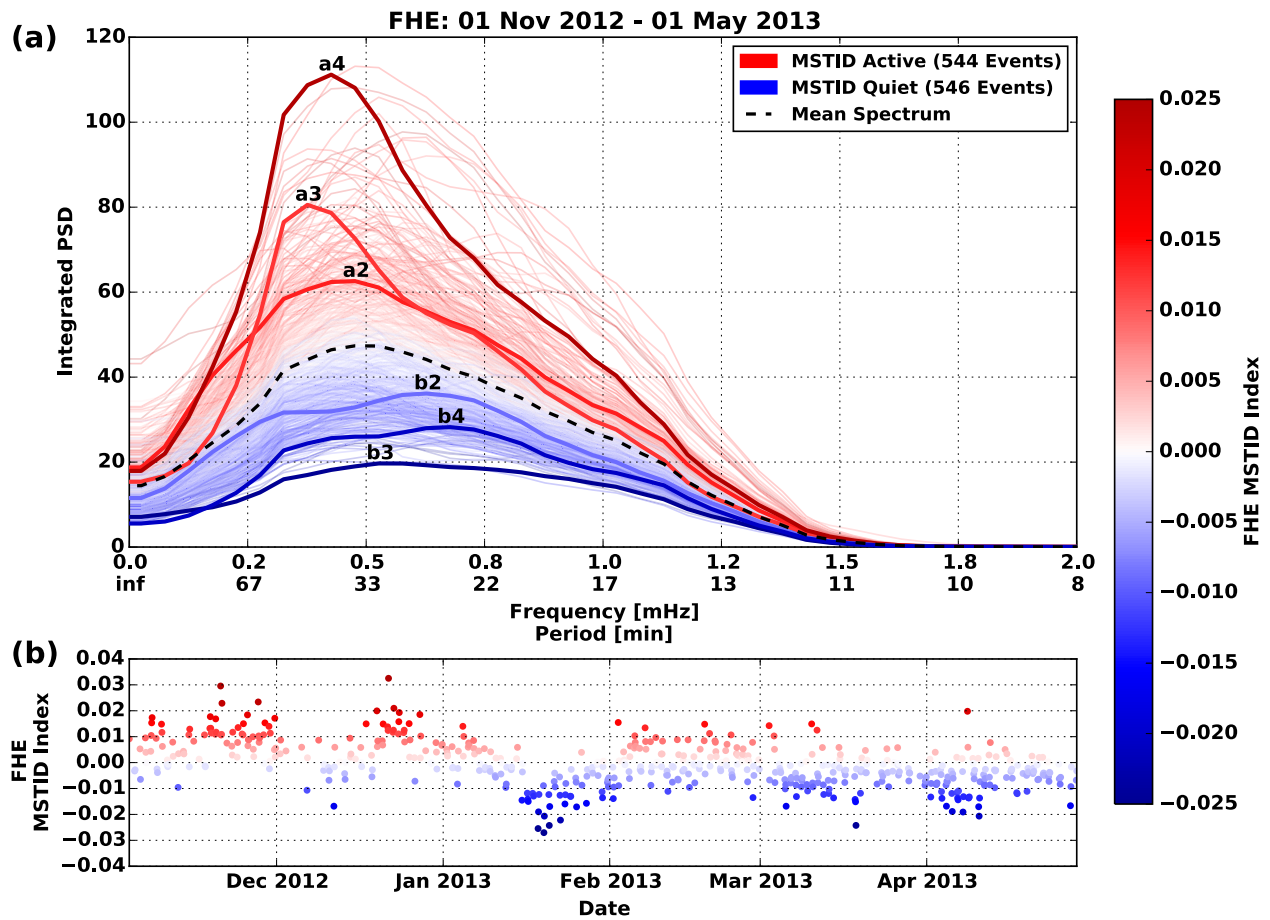


Figure 4.4: (a) Spectral curves for the FHE 2012-2013 observational season. Each trace represents the MSTID-band power spectral density (PSD) within a 2 hr sampling window. Bold traces marked a2-a4 and b2-b4 correspond with the sampling windows presented in Figure 4.3. Color represents both SuperDARN MSTID Index and classification as MSTID-active (reds) and MSTID-quiet (blues) periods. The black dashed trace shows the seasonal mean. (b) Time series of the FHE MSTID Index values from panel (a).

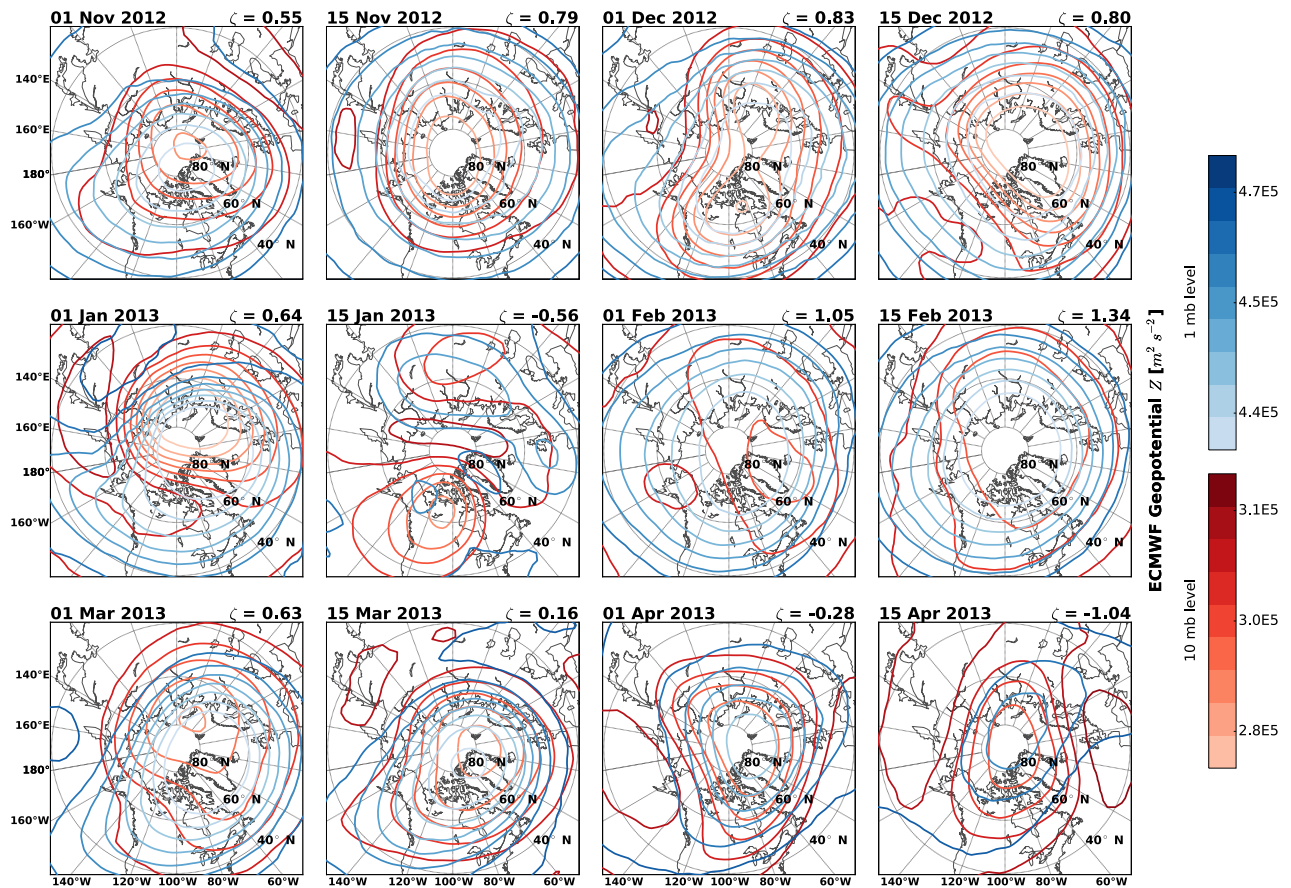


Figure 4.5: The strength of the polar vortex measured by the ECMWF Geopotential data at the 1 and 10 mb levels. The Polar Vortex Index ζ for each map is printed in the upper right hand corner (see text for details). Large positive values indicate a strong polar vortex.

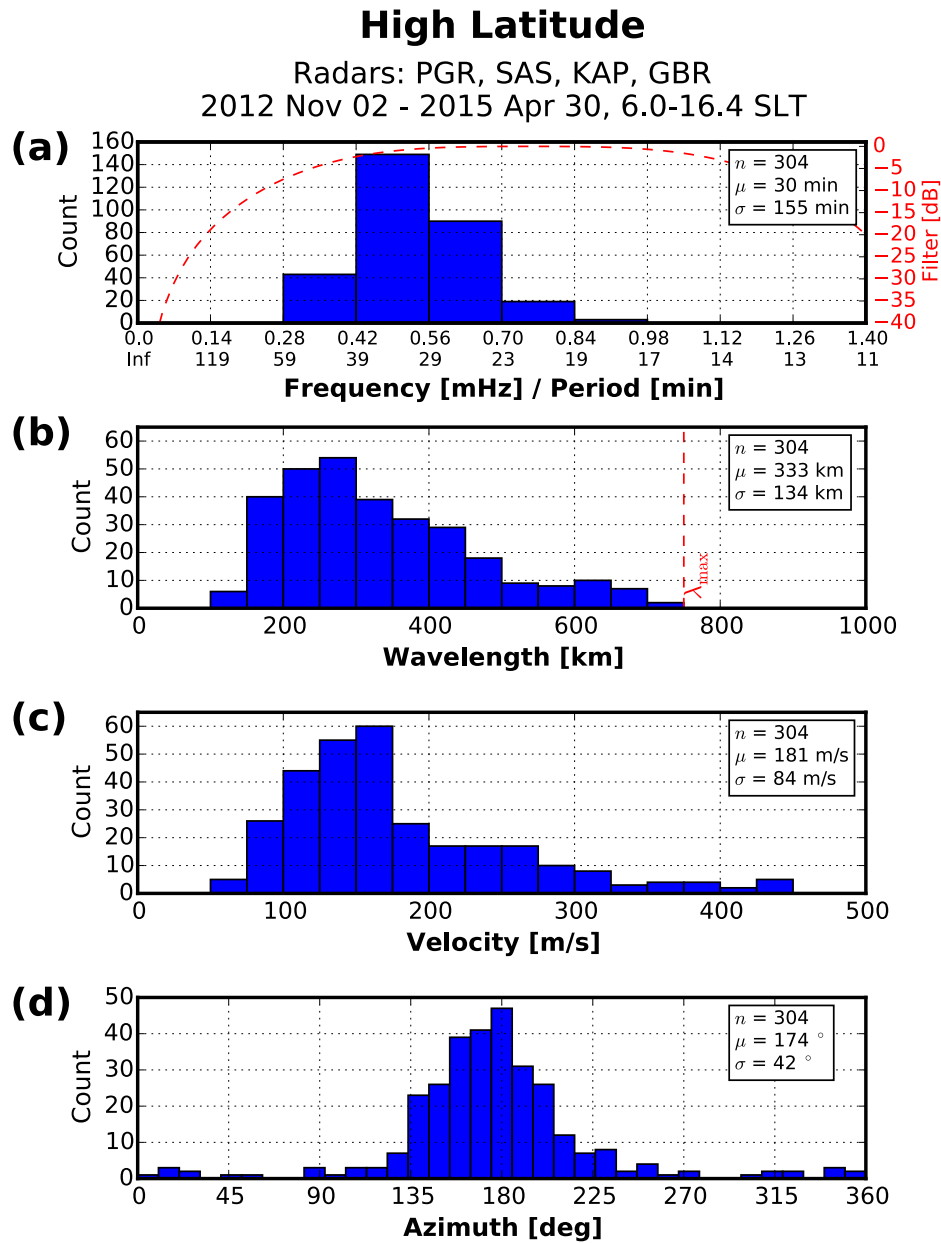


Figure 4.6: Distributions of daytime MSTID parameters for high latitude radars. Each histogram count represents the strongest wave detected in a MSTID-active sampling window. The following parameters are estimated: (a) frequency/period, (b) horizontal wavelength, (c) horizontal phase velocity, and (d) propagation azimuth relative to geographic North. The dashed line in (a) shows the transfer function of the filter applied to the data during processing. The dashed line in (b) indicates the maximum value of horizontal wavelengths allowed in this study.

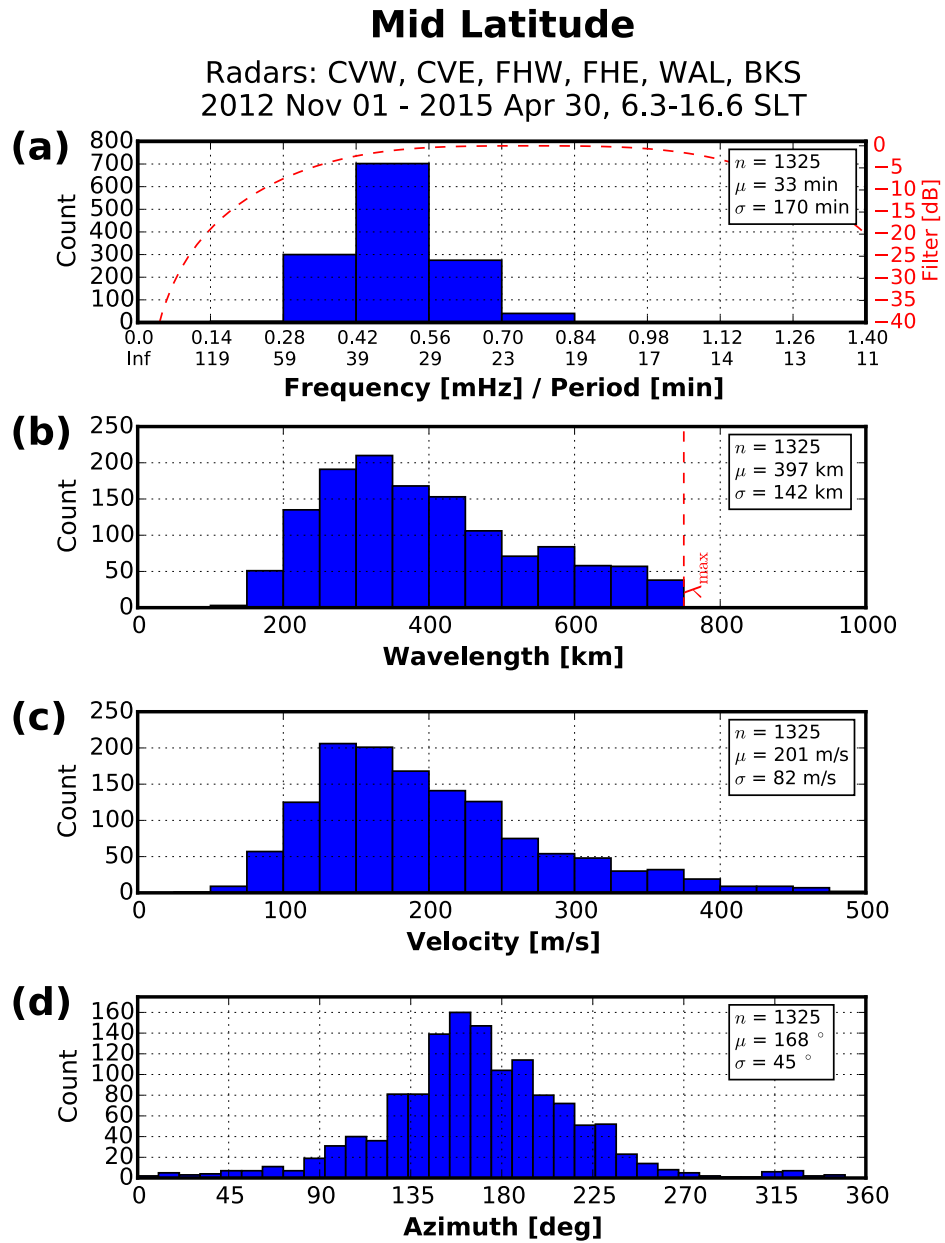


Figure 4.7: MSTID parameter distributions for mid latitude radars (same format as Figure 4.6).

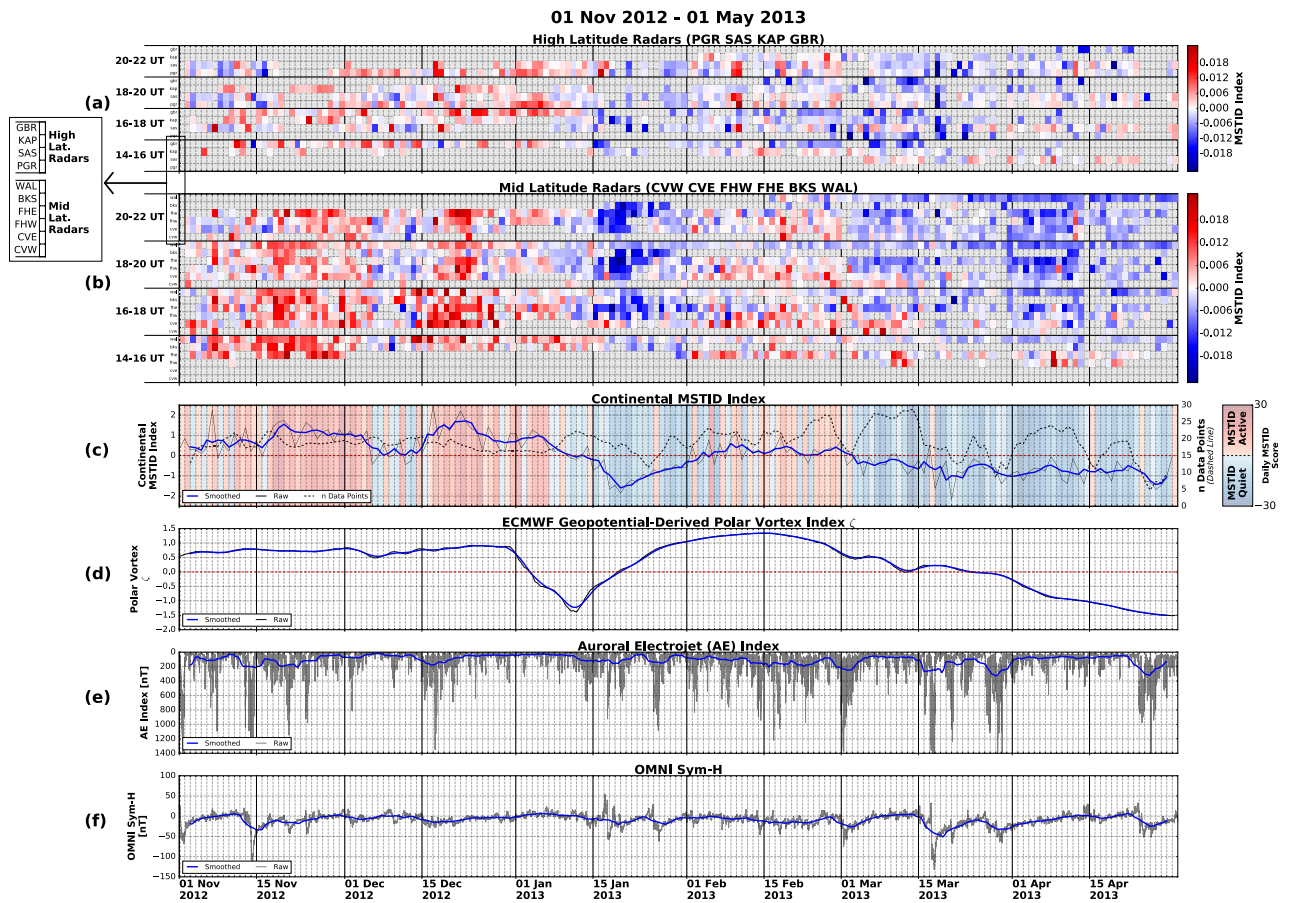


Figure 4.8: Time series of SuperDARN MSTID, polar vortex, and geomagnetic activity for the 2012–2013 observational season. (a) MSTID Index for each of the high latitude radars, with reds showing MSTID-active periods, and blues showing MSTID-quiet periods. (b) Same as (a) for midlatitude radars. (c) Continental MSTID Index (gray and blue traces) and daily number of good sampling windows (dotted line). Background color indicates daily MSTID score and classification, with MSTID-active days in reds and MSTID-quiet days in blues. (d) Polar Vortex Index. (e) Negative *AE* Index. (f) Sym-H Index. In Panels (c)–(f), gray traces show raw data, while blue traces show a 4-day rolling mean smoothing.

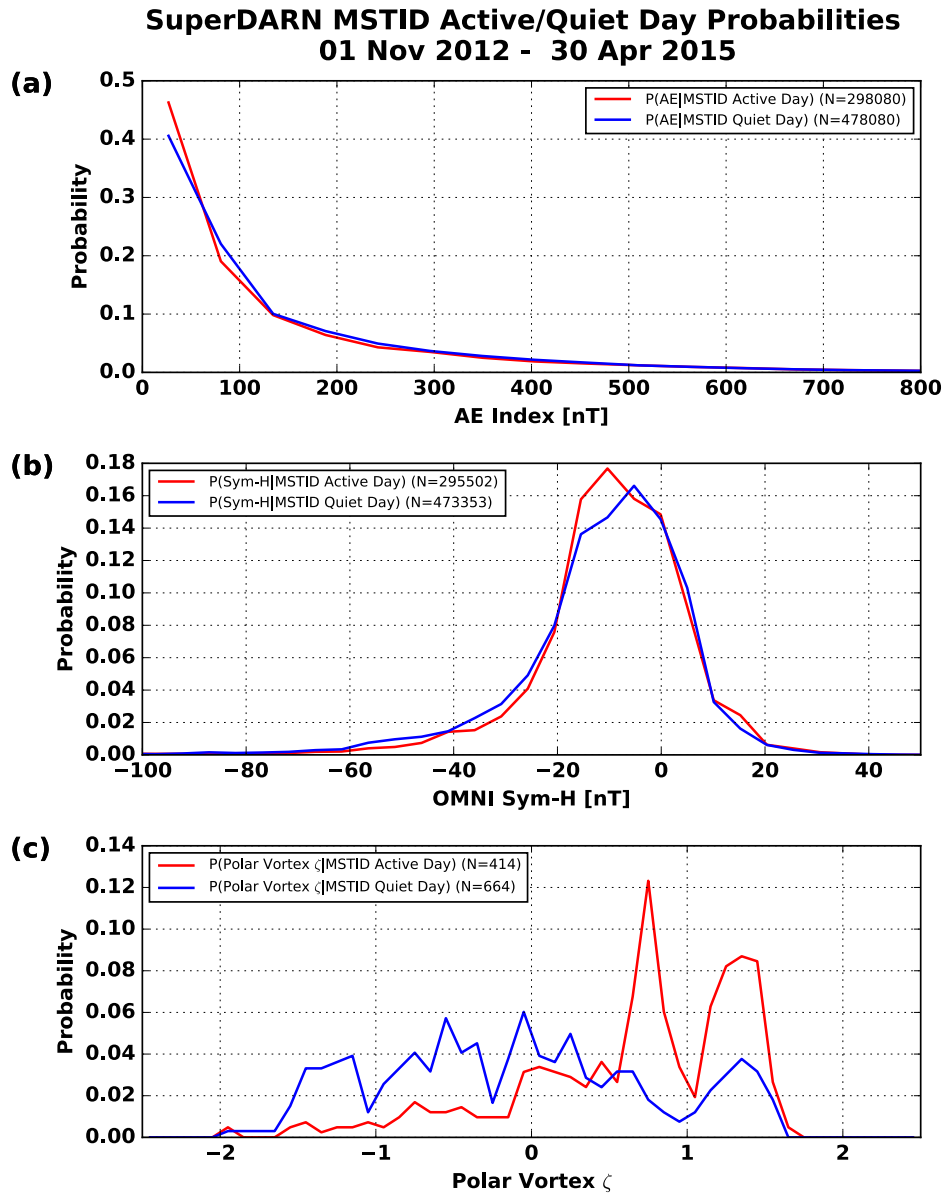


Figure 4.9: Estimated probability density functions for MSTID-active days and MSTID-quiet days as a function of (a) the *AE* index, (b) the Sym-H index, and (c) the Polar Vortex Index.

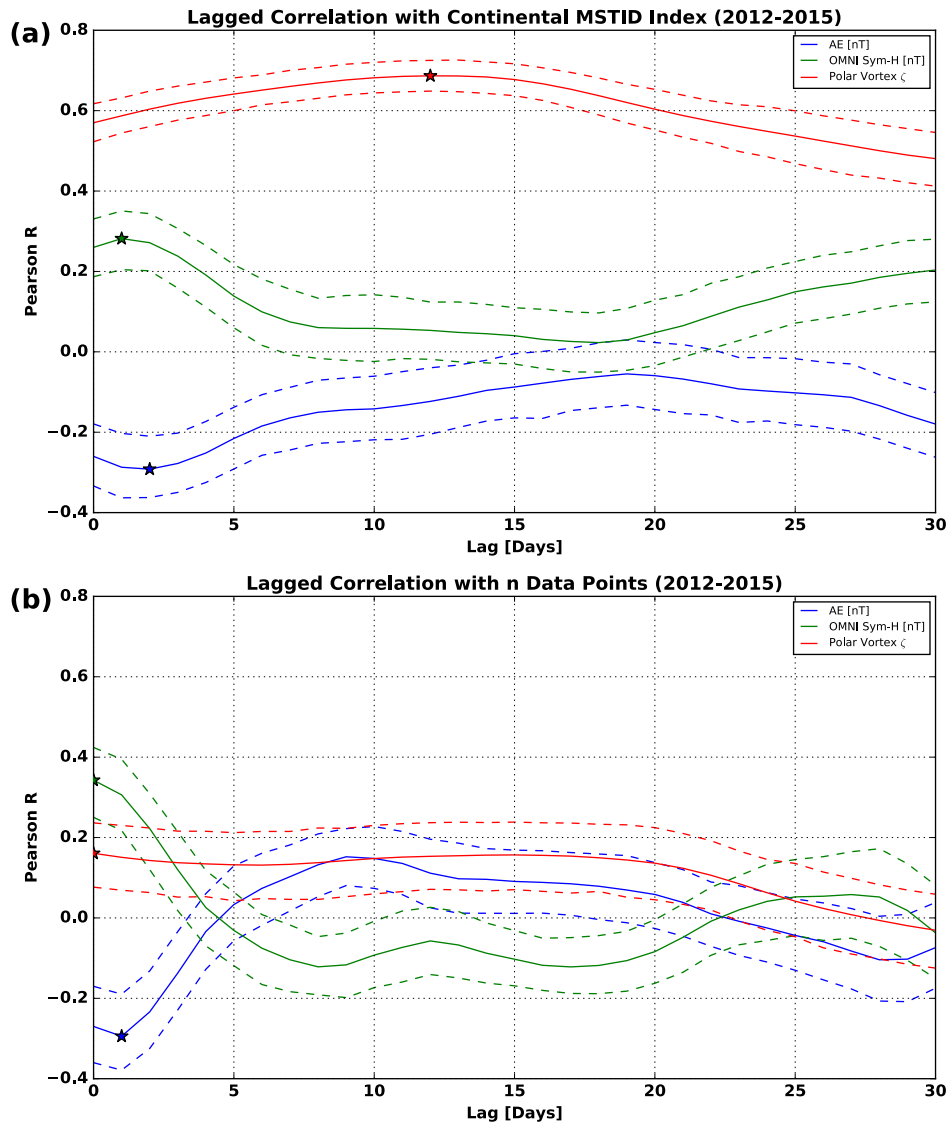


Figure 4.10: Lagged correlation analysis of candidate MSTID driving parameters with (a) the Continental MSTID Index and (b) the n Data Points quality parameter. Stars indicate the point of maximum correlation magnitude for each parameter. Dashed lines indicate 95% confidence intervals. Positive lag values indicate the number of days by which the MSTID index lags the candidate driver.

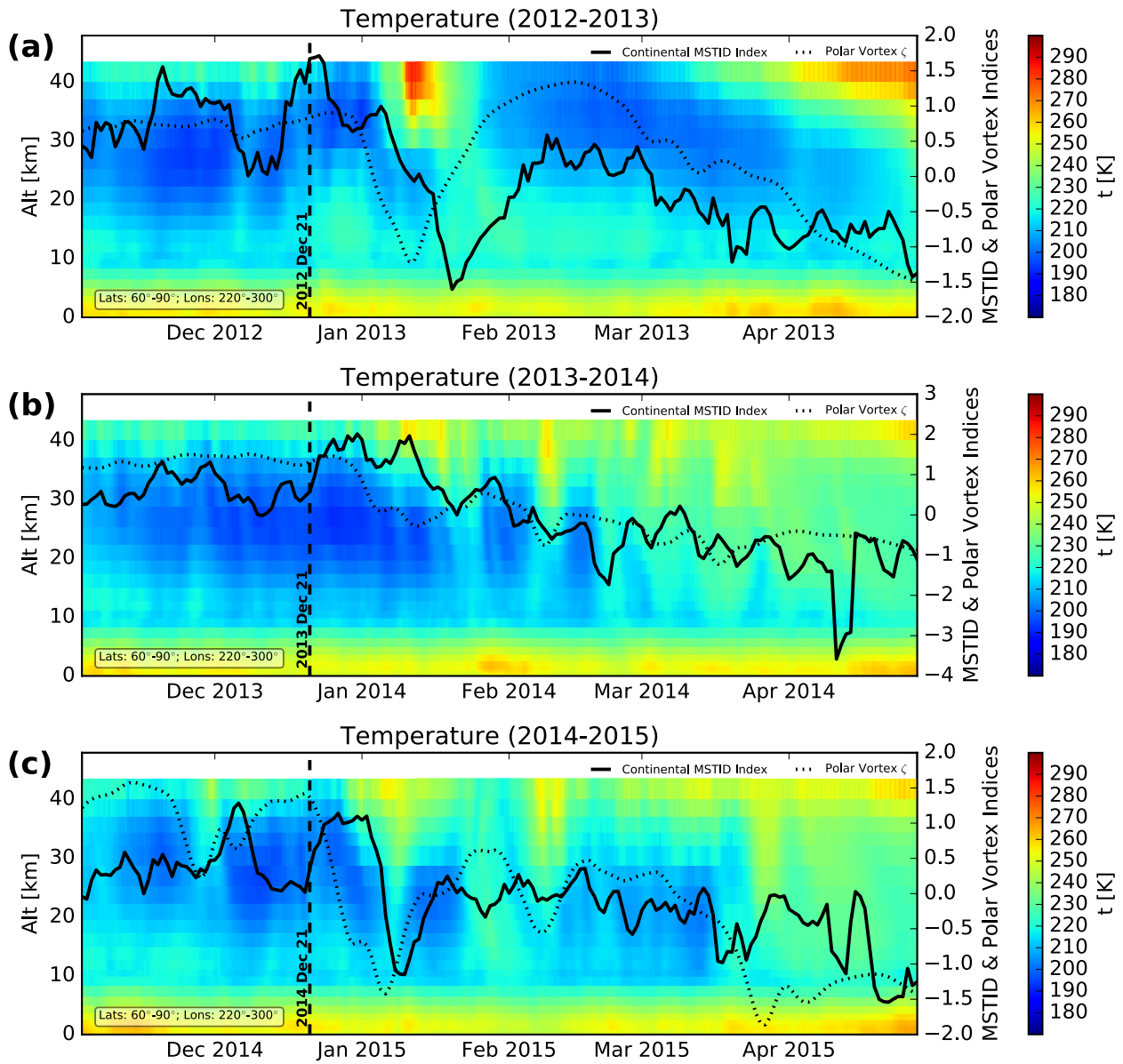


Figure 4.11: Time series of ECMWF TOGA zonal mean temperatures averaged for latitudes poleward of 60° N for each MSTID observational season from 2012–2015. The Continental MSTID Index (bold, black trace) and Polar Vortex Index (dotted trace) are superposed. A vertical, dashed line indicates winter solstice.

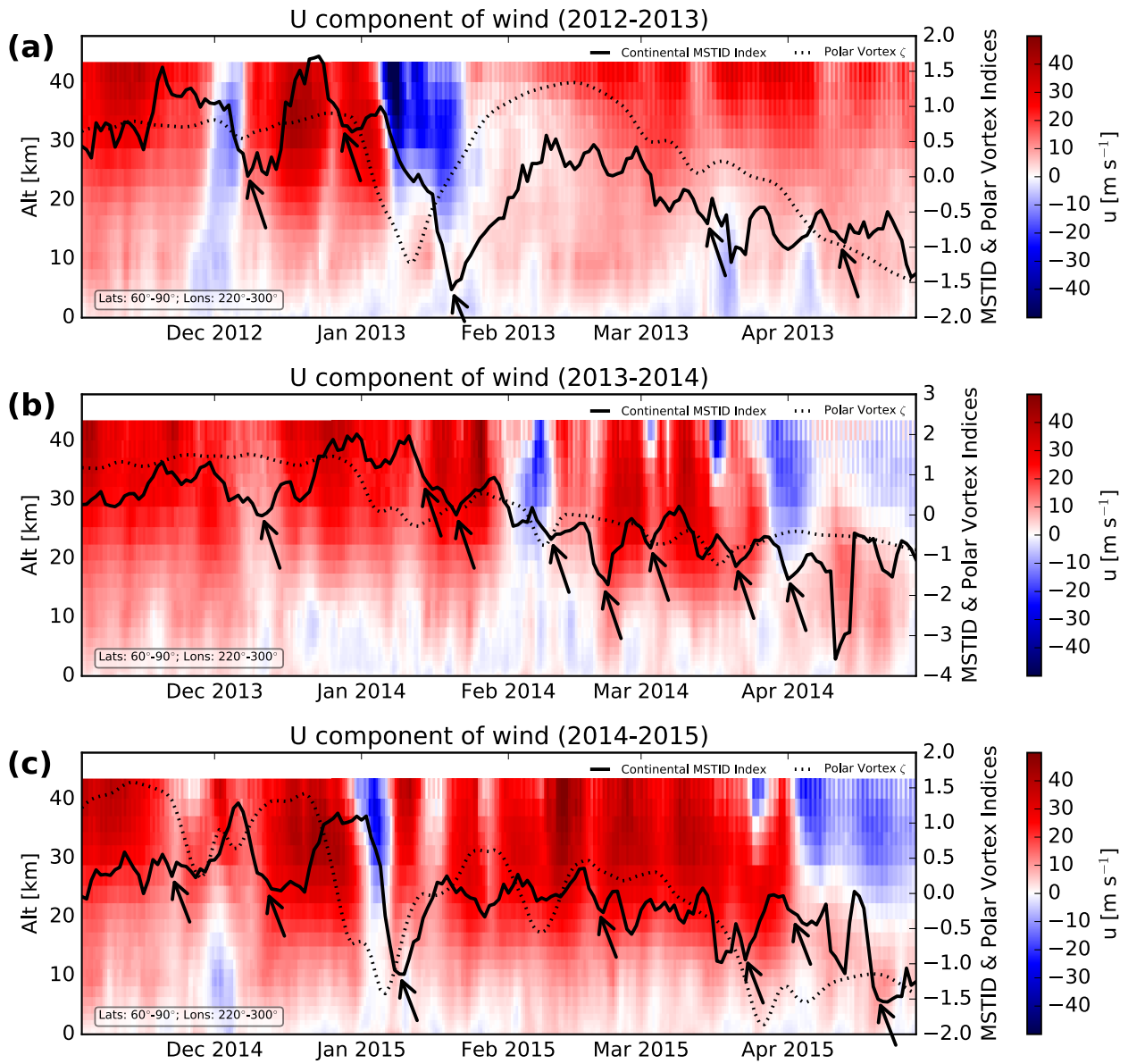


Figure 4.12: Same as Figure 4.11, but showing ECMWF TOGA zonal mean zonal winds. Reds indicate eastward winds; blues indicate westward winds. Black arrows point to select events where the stratospheric winds become less eastward and the Continental MSTID Index decreases.

Supplemental Figures

These supplemental figures are the 2013-2014 and 2014-2015 counterparts to Figure 8 in the main paper.

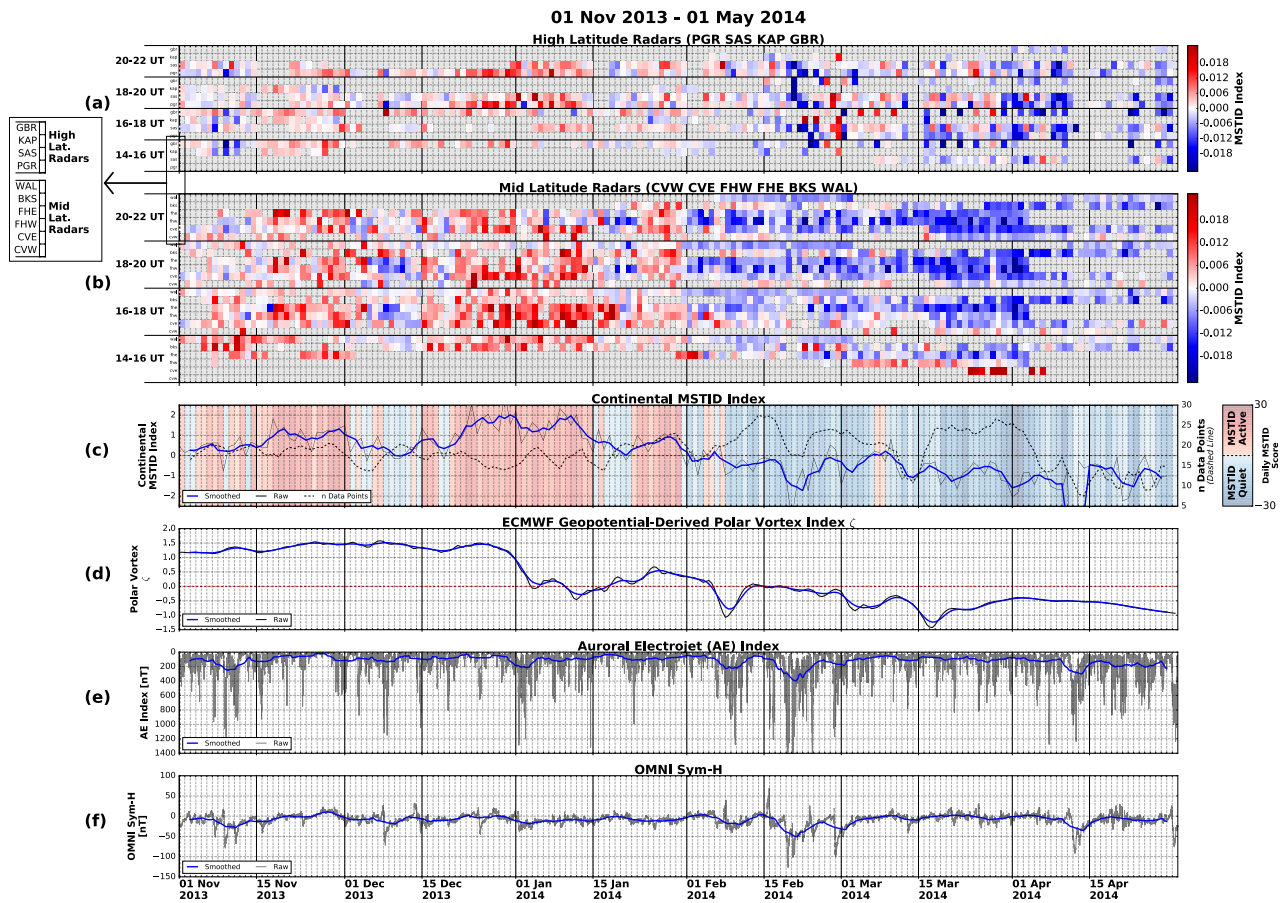


Figure 4.13: Time series of SuperDARN MSTID, polar vortex, and geomagnetic activity for the 2013–2014 observational season. (a) MSTID Index for each of the high latitude radars, with reds showing MSTID-active periods, and blues showing MSTID-quiet periods. (b) Same as (a) for midlatitude radars. (c) Continental MSTID Index (gray and blue traces) and daily number of good sampling windows (dotted line). Background color indicates daily MSTID score and classification, with MSTID-active days in reds and MSTID-quiet days in blues. (d) Polar Vortex Index. (e) Negative *AE* Index. (f) Sym-H Index. In Panels (c)–(f), gray traces show raw data, while blue traces show a 4-day rolling mean smoothing.

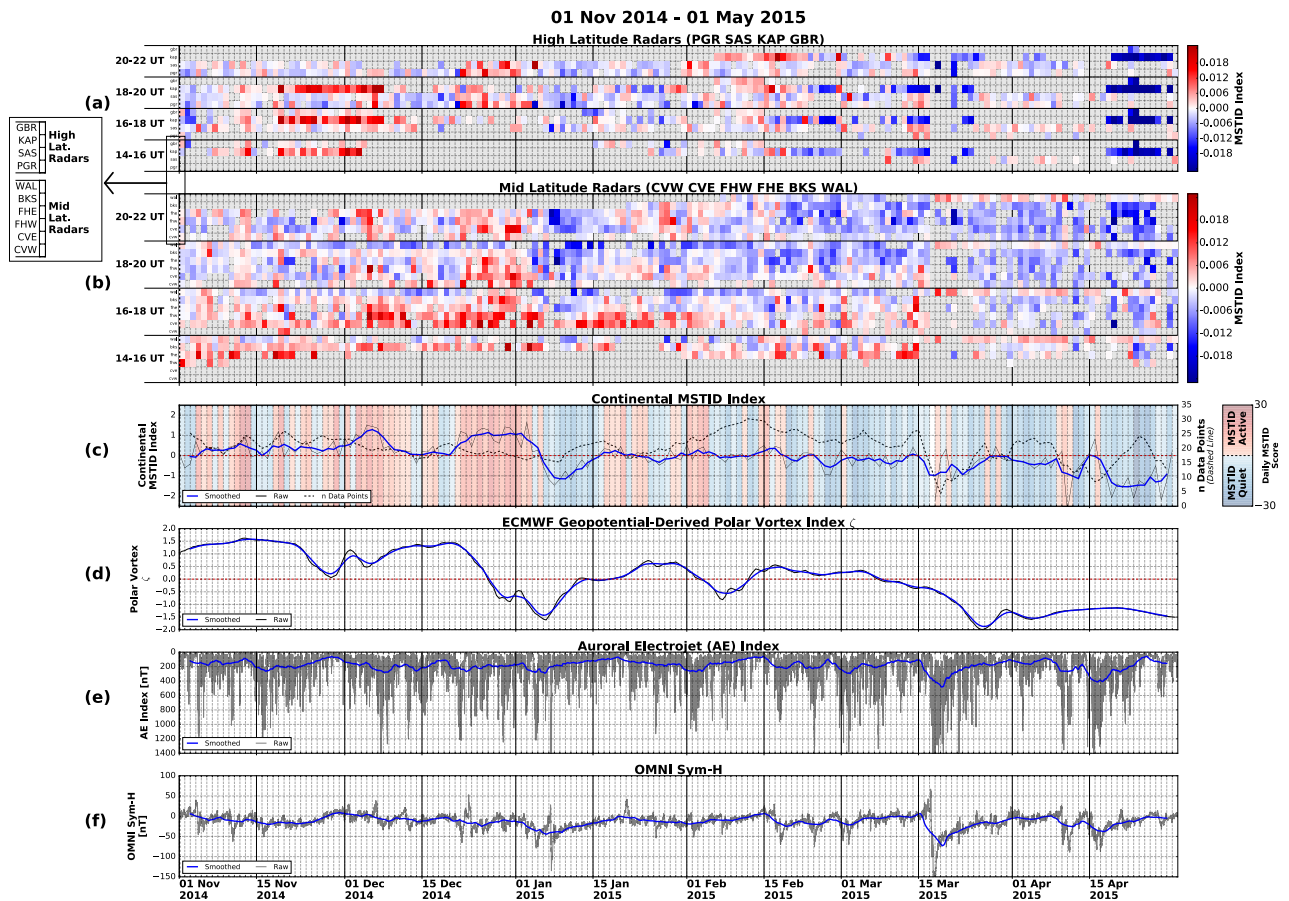


Figure 4.14: Time series of SuperDARN MSTID, polar vortex, and geomagnetic activity for the 2014–2015 observational season. (a) MSTID Index for each of the high latitude radars, with reds showing MSTID-active periods, and blues showing MSTID-quiet periods. (b) Same as (a) for midlatitude radars. (c) Continental MSTID Index (gray and blue traces) and daily number of good sampling windows (dotted line). Background color indicates daily MSTID score and classification, with MSTID-active days in reds and MSTID-quiet days in blues. (d) Polar Vortex Index. (e) Negative AE Index. (f) Sym-H Index. In Panels (c)–(f), gray traces show raw data, while blue traces show a 4-day rolling mean smoothing.

Chapter 5

Ionospheric Sounding Using Real-Time Amateur Radio Reporting Networks

N. A. Frissell¹, E. S. Miller², S. R. Kaeppler³, F. Ceglia⁴, D. Pascoe⁴, N. Sinanis^{4,5}, P. Smith⁴, R. Williams⁴, and A. Shvokoplyas⁶

¹Bradley Department of Electrical and Computer Engineering, Virginia Tech, Blacksburg, Virginia, USA.

²The Johns Hopkins University Applied Physics Laboratory, Laurel, Maryland, USA.

³SRI International, Menlo Park, CA, USA.

⁴Reverse Beacon Network, A Multi-National Cooperative Project.

⁵International Telecommunication Union, Geneva, Switzerland.

⁶Afreet Software, Inc., Richmond Hill, ON, Canada.

Published as:

Frissell, N. A., E. S. Miller, S. R. Kaeppler, F. Ceglia, D. Pascoe, N. Sinanis, P. Smith, R. Williams, and A. Shvokoplyas (2014), Ionospheric Sounding Using Real-Time Amateur Radio Reporting Networks, *Space Weather*, 12, 651656, doi:10.1002/2014SW001132.

Abstract

Amateur radio reporting networks, such as the Reverse Beacon Network (RBN), PSKReporter, and the Weak Signal Propagation Network, are powerful tools for remote sensing the ionosphere. These voluntarily constructed and operated networks provide real-time and archival data that could be used for space weather operations, forecasting, and research. The potential exists for the study of both global and localized effects. The capability of one such network to detect space weather disturbances is demonstrated by examining the impacts on RBN-observed HF propagation paths of an X2.9 class solar flare detected by the GOES 15 satellite. Prior to the solar flare, the RBN observed strong HF propagation conditions between multiple continents, primarily Europe, North America, and South America. Immediately following the GOES 15 detection of the solar flare, the number of reported global RBN propagation paths dropped to less than 35% that of prior observations. After the flare, the RBN showed the gradual recovery of HF propagation conditions.

5.1 Introduction

Space weather and its ionospheric effects can significantly impact many important modern technological systems, including high frequency communication networks, Global Navigation Satellite Systems (GNSS, e.g., the Global Positioning System/GPS), over-the-horizon (OTH) radars, and power distribution grids. Often, these impacts adversely affect the systems listed above, and therefore substantial efforts have been made to measure, characterize, and model the ionosphere. These characterizations and models are then used to mitigate the adverse effects of space weather dynamics. Spatially and temporally dense global ionospheric measurements are critically important for real-time operations, forecasting, and basic space weather and scientific research [Schunk *et al.*, 2014].

A variety of instrument networks currently provides data for ionospheric characterization, including networks of ionosondes [Reinisch *et al.*, 2005], GPS Total Electron Content (TEC) receivers [Rideout and Coster, 2006], satellite-based GPS occultation receivers [Coster and Komjathy, 2008], incoherent scatter radars [Eccles *et al.*, 2011], and high frequency radars [Chisham *et al.*, 2007]. However, the ionosphere is global in size, complex and structured at local spatial scales, and highly dynamic. Although the aforementioned instrument networks are extensive, the ionospheric system remains undersampled. A new source of measurements would be a welcome addition to the current ensemble of ionospheric monitoring networks.

Recently, radio amateurs have voluntarily built networks that monitor transionospheric radio links in real time and report these observations back to central servers. Amateur radio operators, also known as ham radio operators, are radio hobbyists who are licensed to conduct two-way communications on amateur radio frequencies for non-commercial purposes. The amateur radio bands are distributed across the entire radio spectrum, including those bands that support long-distance propagation and are directly impacted by ionospheric conditions.

Table 5.1 lists the most active of these amateur frequencies, which are spread across the MF (medium frequency, 300 kHz - 3 MHz), HF (high frequency, 3 - 30 MHz), and VHF (very high frequency, 30 - 300 MHz) bands.

Radio amateurs routinely use these frequencies to attempt two-way communications with distant locations in an activity known as “DXing.” Activity is increased during “contest” periods, in which operators engage in a time-limited competition to exchange a prescribed minimum amount of information with as many fellow amateurs in as many places as possible. These activities, among others, provide a geographically diverse source of signals across the radio spectrum. These links may be viewed as ionospheric “soundings,” and give valuable information when reported back to a central database and properly analyzed. In this article, we describe some amateur radio reporting networks that are currently operational and provide an example of an X-class solar flare impacting the signals monitored by these networks.

5.2 Amateur Radio Reporting Network Architecture

Multiple amateur radio reporting networks currently exist, each with its own characteristics and strengths. Table 5.2 gives the names, Internet addresses, and summary notes for a selection of popular networks. The oldest network, the DX Cluster, relies on manual reports provided by operators listening to radios. WSPRNet, the Weak Signal Propagation Reporting Network, is a digital mode specifically designed for ionospheric propagation monitoring [Taylor and Walker, 2010]. Both PSKReporter and the Reverse Beacon Network (RBN) use passive receivers to automatically identify signals. PSKReporter monitors numerous digital communication modes, including Phase Shift Keying 31 Hz (PSK31) and radioteletype (RTTY), while the RBN primarily focuses on Morse code (a.k.a. Continuous Wave/CW) signals. The RBN and PSKReporter are advantageous in that the receiving stations are fully

automatic and may be legally operated by users without amateur radio licenses.

Figure 5.1 shows a block diagram of the hardware for a typical RBN or PSKReporter type receiving station, including the antenna, receiver, and computer. An ideal station would be able to receive signals omnidirectionally and simultaneously with equal response across all bands of interest (typically 1.8 - 54 MHz). Recent advances in software defined radio (SDR) have made this nearly possible through direct digital sampling and software decoding of large portions of the radio frequency (RF) spectrum. Antennas and SDR receivers that meet the required specifications are available commercially. Once the RF spectrum has been sampled by the SDR and sent to the computer, further processing must be done in order to identify the signals of interest.

The RBN relies on a multi-band, multi-channel Morse code decoding program (CW Skimmer, developed by co-author Alex Shovkoplyas) to decode all observed Morse code transmissions in parallel and report data back to the RBN servers. Figure 5.2 is a screenshot of the CW Skimmer program that shows the decoding of a 3 kHz segment of the 40 m amateur radio band. The left-hand portion of the screenshot shows a waterfall display, which is a short-time Fourier transform that plots spectral power versus time. Current signals appear at the right edge of the waterfall and move to the left with time. Visual representations of the Morse code signals detected can be observed in the waterfall. CW Skimmer uses a Bayesian statistics-based algorithm for decoding each signal. The amateur radio call sign associated with each signal is displayed in the right-hand column of the window, and the latitude and longitude of each station may be determined via a call sign lookup in an appropriate database. For the purpose of showing detail, Figure 5.2 shows only 3 kHz of spectrum. This is the standard audio passband of a typical analog amateur radio receiver. However, the most capable software-defined radio receivers and computers (as described above) would process all HF spectrum of interest simultaneously.

5.3 Case Study: Ionospheric Impacts of the 13 May 2013 Solar Flare

We demonstrate the capabilities of these amateur radio networks to observe the ionospheric effects of a space weather event by showing the impact of an X-class solar flare observed by the Geostationary Operational Environmental Satellite (GOES) 15 spacecraft on observations made by the Reverse Beacon Network (RBN). All data analysis and visualization of RBN and GOES data was completed with the help of free, open-source software tools such as matplotlib [Hunter, 2007], IPython [Pérez and Granger, 2007], pandas [McKinney, 2010], and others [e.g. Millman and Aivazis, 2011]. Figure 5.3 shows both Reverse Beacon Network and GOES 15 data from 13 May 2013. Panels (a-d) show maps of observations made by the RBN beginning at 1505 UT with 15 min integration periods and a 30 min cadence. Observations are color-coded by frequency band, with blues and greens indicating lower frequencies (1.8-14 MHz) and yellows and reds indicating higher frequencies (14-28 MHz). Black dots indicate RBN receiving stations, which are only shown if a particular receiving station detects at least one transmitting station during a given integration period. The RBN identifies each station by call sign, which is geolocated via a lookup in the QRZ.com database (<http://www.qrz.com>). RBN observations without valid database locations are omitted from the maps and subsequent analysis. The number of plotted propagation paths, transmitting stations, and receiving stations identified during each integration period is printed in the lower left hand corner of each map. Shading indicates the location of the solar terminator. The geolocated RBN data presented in Figures 5.3a - 5.3d is available as online supporting information data set ds01.

Panel (e) of Figure 5.3 shows GOES 15 X-ray Sensor (XRS) [Chamberlin *et al.*, 2009] measurements for the 0.05-0.4 nm (green trace) and the 0.1-0.8 nm (red trace) soft X-ray bands for 13 May 2013 1300-1900 UT. The GOES 15 satellite is in geostationary orbit at

135° W longitude, and therefore able to observe X-ray flux incident on the daylight region of the RBN maps shown. A blue dot at 1605 UT on the red trace indicates the peak of a sharp increase in X-ray flux indicative of an X2.9 class solar flare. The peak of this flare is observed coincident with the starting time of the Panel (c) RBN map and corresponds to a dramatic decrease in HF propagation conditions observed by the RBN. Panels (a) and (b) show a significant number (over 1100) of HF paths between Europe, North America, South America, and Africa on frequencies from 7 to 28 MHz. Immediately after the peak of the flare, Panel (c) shows less than 35% of the propagation paths of the preceding map. Almost all 7 and 28 MHz activity disappears, along with all links to South America, Africa, and most links between Europe and the United States. Panel (d), which begins 30 min after the flare peak, starts to show some recovery as a few paths from Europe to the Western United States, South America, and Africa reappear, along with some 7 and 28 MHz activity.

5.4 Discussion

The 13 May 2013 1605 UT solar flare event provides a strong example of the types of monitoring and observations that can be made with the Reverse Beacon Network (RBN). It is also important to discuss factors that may bias the data. One factor possibly apparent from studying the Figure 5.3 maps is the spatial distribution of transmitters and receivers. Certain geographic regions, such as North America and Europe, tend to have a large number of amateur stations due to both economic and political conditions in those regions. Human behavior also affects the number of signals present at any given time, as transmissions generally require operators to be awake and available during leisure hours. Also, operators will automatically adjust their transmissions to bands that appear to have the best propagation conditions, which can lead to a lack of sampling on frequencies with poor propagation. Amateur networks

are also not subject to rigorous station design, which leads to uncertainty of gain, loss, and directivity factors at any given station. Finally, networks that rely on databases for geolocation are subject to incorrect location reporting when amateurs decide to operate from portable stations or fail to update their location when moving.

Although these biases exist, effects of these issues may be mitigated. For instance, the station distribution problem is partially addressed by a large number of radio amateurs who are motivated to operate from remote locations. Both the spatial problem and the human behavior problem is further addressed by the existence of the Northern California DX Foundation (NCDXF) beacon network, a globally distributed set of autonomous Morse code beacons operating on the amateur bands from 14 to 28 MHz [*Troster and Fabry, 1997*]. These beacons are built to known specifications and transmit on a published schedule from known locations, as indicated by the blue stars on Figures 5.3a - 5.3d. It is possible to further improve the data through the installation of additional receivers by interested parties such as researchers, as well as improve the capabilities of the skimming software used for automatic observations. Software could be created with capabilities to automatically observe more types of transmissions, including voice communications. With current SDR capabilities, it is also possible to make observations of non-amateur signals via software upgrades to current systems. Good use could then be made of transmitters with known characteristics, such as standards stations and commercial broadcast stations. Finally, careful analysis using all data available, not just that from a single network, will greatly enhance the value of the observations.

5.5 Summary

In this article, we demonstrated the ability of one amateur radio reporting network, the Reverse Beacon Network (RBN), to detect space weather disturbances by examining the impacts on HF propagation of an X2.9 class solar flare detected by the GOES 15 satellite. Prior to the solar flare, the RBN observed strong HF propagation conditions between multiple continents, primarily Europe, North America, and South America. Immediately following the GOES 15 detection of the solar flare, the number of reported global RBN propagation paths dropped to less than 35% that of prior observations. After the flare, the RBN showed the gradual recovery of HF propagation conditions.

Amateur radio reporting networks, such as the RBN, PSKReporter, and WSPRNet are powerful tools for remote sensing the ionosphere. These voluntarily constructed and operated networks provide real-time and archival data that could be used for space weather operations, forecasting, and research. We recognize that the observations made by these networks essentially constitute an untapped “big data” resource in the fields of space weather and space science, one that merits further exploration. The potential exists for the study of both global and localized effects.

5.6 Acknowledgments

The RBN data shown in Figure 5.3 is available as supporting information data set ds01. The GOES data shown in Figure 5.3 is provided by the Space Weather Prediction Center, Boulder, CO, National Oceanic and Atmospheric Administration (NOAA), US Dept. of Commerce and is available at <http://satdat.ngdc.noaa.gov>. We acknowledge the use of the free, open source software projects used in this analysis: Ubuntu Linux, python, matplotlib, pandas,

NumPy, SciPy, IPython, python-hamtools, and others.

Approx. Wavelength [m]	Frequency [MHz]
160	1.800 - 2.000
80	3.500 - 4.000
40	7.000 - 7.300
30	10.100 - 10.150
20	14.000 - 14.350
17	18.068 - 18.168
15	21.000 - 21.450
12	24.890 - 24.990
10	28.000 - 29.700
6	50.000 - 54.000
2	144.000 - 148.000

Table 5.1: Amateur radio bands typically monitored for propagation conditions. Frequency limits listed here are valid in the United States; exact frequency limits will vary based on country.

Reverse Beacon Network http://www.reversebeacon.net/	Passive receiving stations automatically listen primarily for Morse code transmissions.
WSPRNet http://wsprnet.org/	Weak Signal Propagation Reporting Network. This is an active mode specifically designed for evaluating ionospheric communication links. Member stations typically transmit and receive.
PSKReporter http://pskreporter.info/	Passive receiving stations automatically listen for digital amateur radio transmissions, including Phase Shift Keying 31 Hz (PSK31), radioteletype (RTTY), and many others.
DX Cluster e.g. http://www.dxwatch.com/	Network where radio operators manually report on stations they have contacted and heard. This is the oldest digital amateur reporting network; it remains active today.

Table 5.2: Selected real-time amateur radio reporting networks.

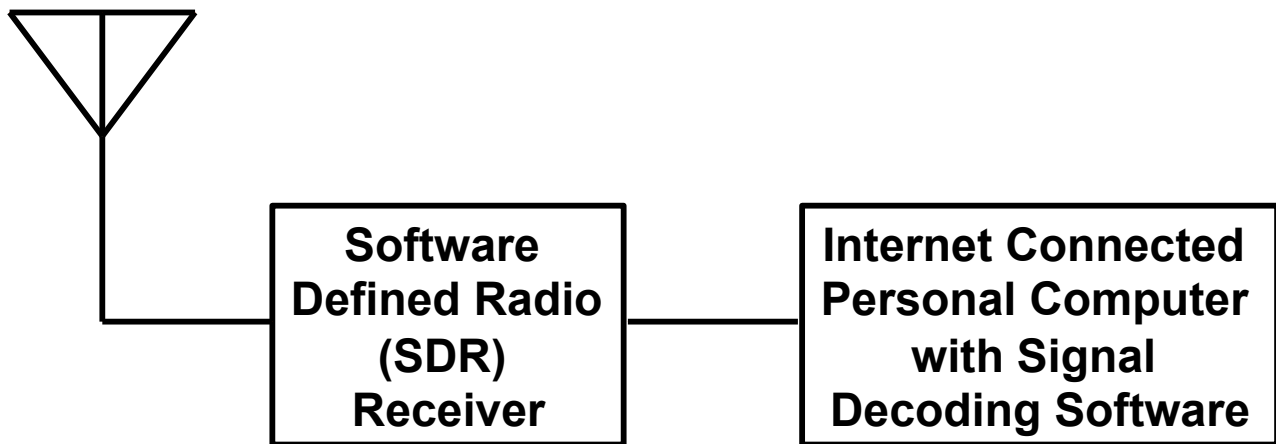


Figure 5.1: Block diagram for a typical automatic amateur reporting network receiving station, including the antenna, receiver, and computer. An ideal station would be able to receive signals omnidirectionally and simultaneously with equal response across all bands of interest (typically 1.8 - 54 MHz). Antennas and SDR receivers that meet the required specifications are available commercially.

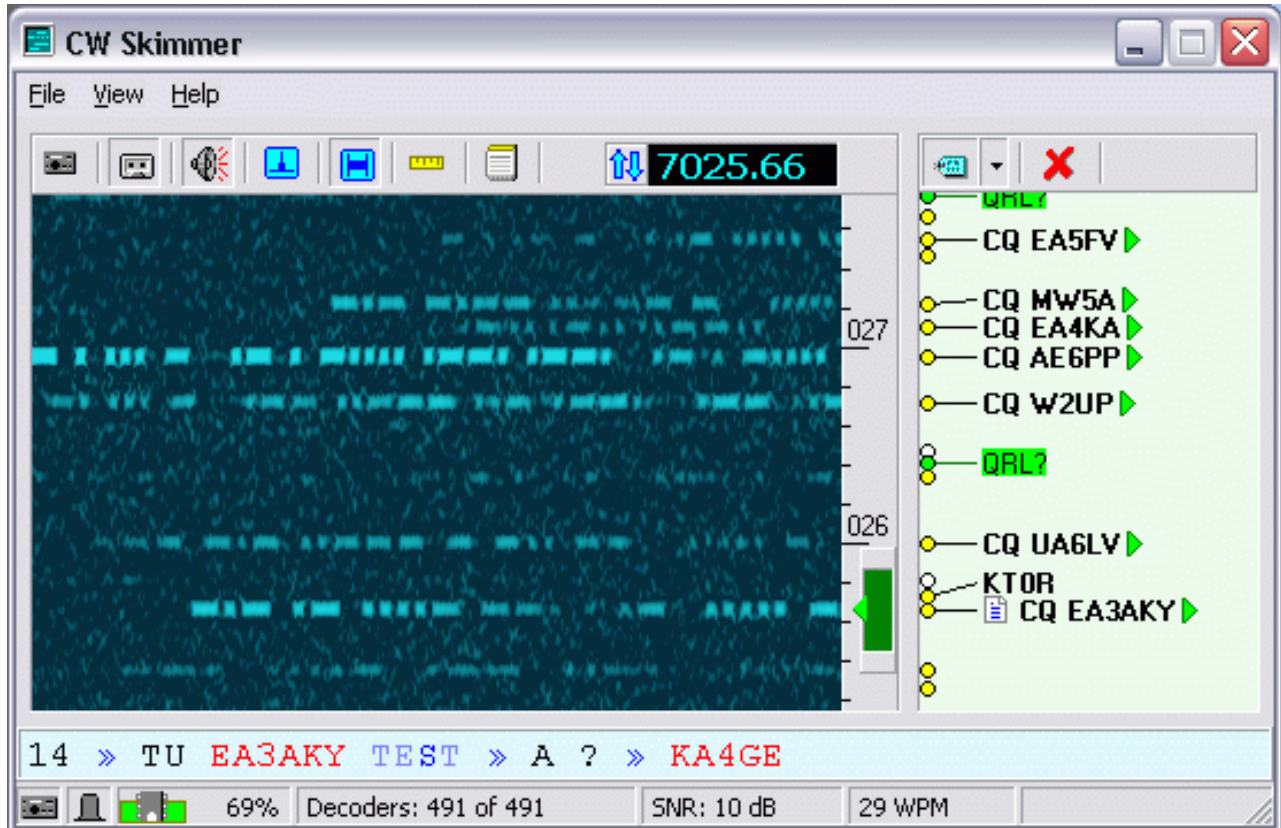


Figure 5.2: A screenshot of the CW Skimmer program used by the Reverse Beacon Network shown decoding a 3 kHz segment of the 40 m amateur radio band. The left-hand portion of the screenshot shows a waterfall display, which is a short-time Fourier transform that plots spectral power versus time. Visual representations of the Morse code signals can be observed in the waterfall. The right-hand column of the screenshot shows a list of radio call signs detected by the CW Skimmer Morse code decoding algorithm.

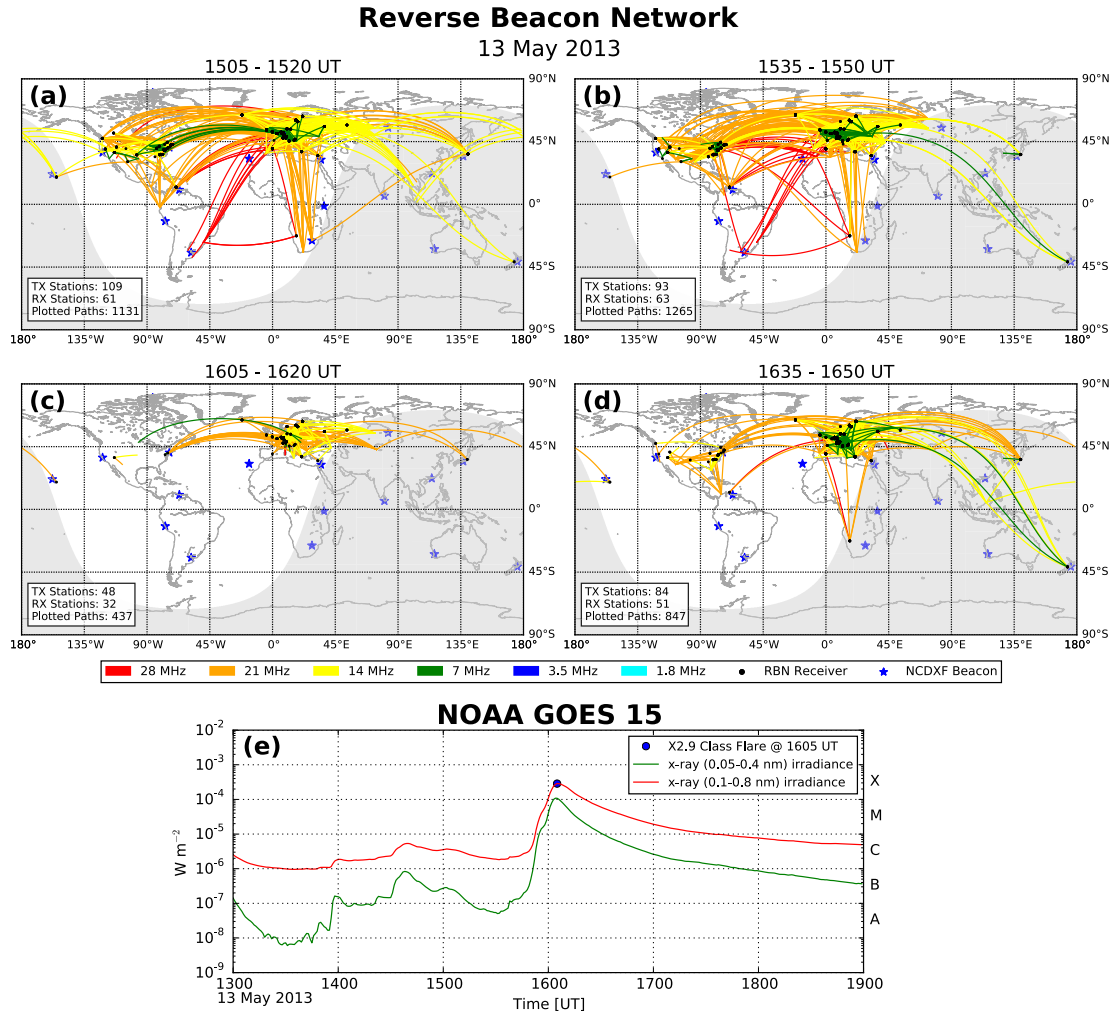


Figure 5.3: (a - d) Reverse Beacon Network (RBN) high frequency propagation path observations from 13 May 2013 beginning at 1505 UT with 15 min integration periods and a 30 min cadence. Paths are color-coded by frequency band. Black dots indicate RBN receiving stations, while blue stars indicate Northern California DX Foundation (NCDXF) beacons. The number of unique transmitting (TX) and receiving (RX) stations within each 15 min period is given in the lower-left corner of each map. Shading indicates the solar terminator. (e) GOES 15 X-ray sensor measurements for the 0.05-0.4 nm (green trace) and the 0.1-0.8 nm (red trace) soft X-ray bands for 13 May 2013 1300-1900 UT. A blue dot at 1605 UT on the red trace indicates the peak of an X2.9 class solar flare and corresponds to a dramatic decrease in RBN activity.

Chapter 6

Summary and Future Work

6.1 Summary

This dissertation has set out to observe, characterize, and understand two distinct types of ionospheric disturbances and their underlying causes. Chapter 2 studied observations of midlatitude substorm Pi2 pulsations, while Chapters 3 and 4 examined traveling ionospheric disturbances associated with neutral atmospheric gravity waves. Finally, Chapter 5 presented a novel approach to the study of space science and space weather using crowd-sourced observations. The research questions and findings associated with each of these studies are summarized below.

Chapter 2: Magnetospheric Pi2 ULF Pulsations

1. What is the source of energy and mechanism of generation of Pi2 pulsations observed in the midlatitude nightside ionosphere?

Chapter 2 presented the first radar observations in the vicinity of the plasmopause of pulsed ionospheric flows generated by bursty bulk flows (BBFs). About a minute following the

observation of two fast, earthward moving plasma flows in the magnetotail, the Blackstone SuperDARN radar and a network of ground magnetometers measured disturbances in the ionosphere and on the ground that were determined to be magnetospheric Pi2 ULF pulsations. Comparison of the waveforms of the first two pulses observed by the radar and magnetometers with those of the plasma flows observed by the spacecraft revealed similarities that suggested a common source. A cross-phase analysis of the magnetometer measurements placed the radar measurements in the vicinity of the plasmopause. Detailed examination of the radar data showed evidence of magnetic field line compression, suggesting that the Pi2s were directly generated by compressions of inner magnetosphere by the observed BBFs.

Previously, *Kepko and Kivelson* [1999] and *Kepko et al.* [2001] had hypothesized that compressional energy from BBFs could directly drive Pi2 pulsations observed by low/mid latitude nightside magnetometers. However, they were unable to conclusively show that this was the case, and there was still speculation that such pulsations could be interpreted as shear Alfvén waves instead of a compressional pulsation. Chapter 2 has provided clear evidence that BBFs can directly drive pulsations observed in the plasmasphere through direct compression of the inner magnetosphere.

Chapters 3 and 4: Medium Scale Traveling Ionospheric Disturbances

1. How often do midlatitude daytime AGW-MSTIDs occur as a function of month and local time?
2. What are the distributions of daytime AGW-MSTID characteristics (period, horizontal wavelength, velocity, and direction) in the high latitude and midlatitude regions?
3. How are daytime AGW-MSTIDs in the high latitudes and midlatitudes related?
4. What is the relationship of daytime AGW-MSTIDs in the high latitudes and midlatitudes

to geomagnetic activity and polar atmospheric dynamics?

5. What are the sources of the daytime AGW-MSTIDs observed in the high latitude and midlatitude regions?

Chapter 3 presented a statistical study of midlatitude daytime medium scale traveling ionospheric disturbances (MSTIDs) associated with atmospheric gravity waves (AGWs) observed using the Blackstone SuperDARN radar. This study found that the majority of MSTID activity was observed in the late fall through early spring. Two MSTID populations were found, a larger population heading southeast, and a smaller population heading northwest. A local time dependence was observed such that the larger southeastward population decreased in number as the day progressed until a late afternoon increase, while the smaller northwestward population appeared only in the afternoon. A comparison with model thermospheric wind velocities suggested that neutral wind filtering may be responsible for this local time dependence. Although a weak correlation with the auroral electrojet (AE) index was found, this study did not find strong evidence pointing to any particular MSTID source.

Chapter 4 expanded the search for MSTID sources by including observations from multiple SuperDARN radars distributed across the North American continent. Four high latitude and six midlatitude radars were used. It was found that the climatology of MSTIDs in both the midlatitude and high latitude regions have similar characteristics. This includes horizontal velocities between ~ 75 to 325 m s^{-1} , horizontal wavelengths that range from ~ 150 to 650 km , and a dominantly equatorward propagation direction of $\sim 125^\circ$ to 225° geographic azimuth. No significant northward population was observed. MSTID activity peaked in the fall and winter, and declined in the spring and summer. Based on observations, it was suggested that the climatological midlatitude and high latitude MSTID populations share a common source. These results are generally consistent with MSTID climatologies reported throughout the

literature.

The dominant equatorward propagation direction, along with theoretical work, has led many authors to suggest that AGWs generated by space weather and auroral activity were the primary source of the observed MSTIDs. However, this hypothesis leads to a number of inconsistencies. Specifically, observational studies typically report that MSTID activity correlates poorly with indices of space weather and auroral activity. An alternative hypothesis is that processes internal to the lower and middle atmosphere generate the AGWs that create the MSTIDs; however, there have been no reports of a polar atmospheric system capable of generating the required climatological population of observed fall and winter equatorward propagating MSTIDs.

This situation changed with Chapter 4, which used SuperDARN radars to discover that MSTID activity levels not only have a seasonal peak in the late fall and early winter, but also exhibit a multi-week timescale that is collectively observed across the North American continent. This information, in conjunction with the dominantly observed equatorward MSTID propagation direction, led to the finding that MSTID activity levels are highly correlated with indices representative of polar vortex activity. It was again shown that MSTID activity levels are poorly correlated with indices representative of space weather and auroral activity.

Closer examination of both radar MSTID observations and neutral atmospheric data suggests that systematic changes in stratospheric neutral wind direction are predominantly responsible for the amount of MSTID activity observed in the F region ionosphere. This is likely to be due to a mechanism in the middle atmosphere which filters and modulates upward-propagating AGWs generated in the lower atmosphere [*Lindzen, 1981; Whiteway et al., 1997; Gerrard et al., 2002; de Wit et al., 2014*]. Although we have provided strong evidence that F region MSTID observations are predominantly controlled by polar atmospheric dynamics, other

phenomena may also contribute to the F region MSTID population.

Chapter 5: Ionospheric Sounding Using Amateur Radio Networks

1. Can crowd-sourced observations of amateur radio transmissions be used to detect ionospheric disturbances?

Chapter 5 presented a study showing the impact of an X2.9 class solar flare on terrestrial radio communications. Prior to the solar flare, an automated network of amateur radio receivers (Reverse Beacon Network, RBN) observed numerous HF propagation paths between multiple continents, primarily North America, Europe, and South America. Upon detection of the flare by the GOES 15 spacecraft, the number of reported global RBN propagation paths dropped to less than 35% that of prior observations. Gradual recovery of HF propagation was observed following the impact of the solar flare.

Although the gross effect of solar flares on HF propagation is well known, the systematic use of amateur radio signals of opportunity for the study of space science and space weather is novel. Recent advances in information technology and radio, such as the wide-spread availability of high powered computing resources, the Internet, and software defined radio, have made this study possible. Additionally, this study represents a significant milestone for citizen science, as all of the data was generated and collected by volunteer members of the international amateur radio community. Chapter 5 has shown that there is significant potential in the further development of these networks and techniques.

6.2 Future Work

While each of the studies in this dissertation have answered some questions, they have also opened pathways to new research. Selected ideas for further research pertaining to each of the topics addressed by this dissertation are discussed below.

Magnetospheric Pi2 ULF Pulsations

Chapter 2 used SuperDARN radar observations of Pi2 pulsations near the plasmopause to show that bursty bulk flows (BBFs) in the magnetotail could compress the inner magnetosphere and directly generate ground Pi2 signatures. However, this work focused only on the first two pulsations observed in the SuperDARN radar and ground magnetometer data, even though the Pi2 wavetrain continued on with more pulsations. These additional pulsations are unlikely to be caused by the direct compression of the inner magnetosphere, as only two BBFs were observed by the THEMIS spacecraft. Additionally, it was noted that Pi2 pulsations were simultaneously sensed by ground magnetometers not only on the nightside, but also on the dayside and at low latitudes. None of these additional pulsations received more than a cursory mention in this study.

These unexplored observations present a number of open questions and lines for further research. For instance, what mode does the direct response BBF Pi2 couple with after the first two compressional pulses? How does this Pi2 energy propagate seemingly simultaneously from the nightside impact region to the dayside? What is the spatial extent of the ionospheric Pi2 perturbation? Can SuperDARN radars also observe dayside pulsations in the same manner as the ground magnetometers? Additionally, it would be useful to research questions regarding the geoeffectiveness of BBFs compressing the inner magnetosphere. At this time, little effort has been made to know what the inner magnetospheric response is as a function

of BBF strength, direction, and duration.

Medium Scale Traveling Ionospheric Disturbances

The most important finding of Chapters 3 and 4 is that the amount of medium scale traveling ionospheric disturbances (MSTIDs) observed in the F region ionosphere by SuperDARN radars is controlled by polar atmospheric processes, seemingly organized by polar vortex dynamics. However, these studies omit many details of this relationship. In fact, the generating mechanism of the underlying AGWs and how they propagate to both the mid and high latitude ionosphere remains unclear. These are complicated questions that will likely require additional observations and numerical modeling to answer.

Many questions can be asked in order to guide future research. For instance, how does polar vortex morphology, such as changes in vortex shape or position, affect the amount of observed MSTIDs and their propagation direction? Can localized effects be observed? What are the spatial and temporal scales of polar atmospheric variations required to affect changes in the amount of MSTID production? How quickly does the ionosphere respond to changes in polar atmospheric dynamics? How far equatorward can these effects be observed? How are southern hemisphere MSTID dependencies on antarctic atmospheric dynamics similar to or different from northern hemisphere MSTID dependencies on arctic polar dynamics? The answers to these questions will be useful for better understanding the relationships between the upper and lower atmosphere, as well as between different latitudinal regimes.

Finally, as MSTIDs have a practical impact on radio communications, navigation, and measurement systems, it is useful to find methods for predicting MSTID activity levels and characteristics. Chapter 4 demonstrated that certain polar vortex signatures lead changes in MSTID activity levels by time scales of approximately two weeks. With additional work, this

knowledge could potentially be developed into a useful forecast product.

Ionospheric Sounding Using Amateur Radio Networks

Chapter 5 introduced the use of amateur radio receiving networks as a tool for the study of space science and weather by presenting an example of the ionospheric effects of an X2.9 class solar flare on HF communication links. However, much can be done to improve the scientific usefulness of the observations made by these networks. For instance, can geophysical parameters, such as ionospheric layer peak densities, be derived from HF link data? Can HF link data be used as an assimilation parameter to ionospheric models, such as a constraint to the International Reference Ionosphere? How well can HF link data be used to characterize the spatial and temporal ionospheric effects of events such as solar flares or solar eclipses? Can HF link data be a valuable complement to other established ionospheric observation networks, such as SuperDARN or GPS-TEC?

The answers to the above questions can be pursued using HF link observations as currently provided by networks such as the Reverse Beacon Network (RBN). However, because networks such as the RBN have been specifically designed for amateur radio use, the scientific usefulness of HF link data in its present form is somewhat limited. However, most RBN (and similar) receiving stations are in fact wideband HF software defined radio receivers that are capable of collecting significantly more information than is currently recorded. Therefore, it would be useful to research methods of deriving geophysical parameters from wideband observations of raw HF spectra. Software containing these new algorithms could potentially be distributed to the volunteers running the automated receiving stations, thereby significantly improving the scientific capabilities of the network.

Bibliography

- Afraimovich, E. L., O. N. Boitman, E. I. Zhovty, A. D. Kalikhman, and T. G. Pirog (1999), Dynamics and anisotropy of traveling ionospheric disturbances as deduced from transionospheric sounding data, *Radio Science*, *34*(2), 477–487, doi:10.1029/1998RS900004.
- Alexander, M. J., et al. (2010), Recent developments in gravity-wave effects in climate models and the global distribution of gravity-wave momentum flux from observations and models, *Quarterly Journal of the Royal Meteorological Society*, *136*(650), 1103–1124, doi:10.1002/qj.637.
- Angelopoulos, V. (2008), The THEMIS mission, *Space Sci. Rev.*, *141*, 5–34, doi:10.1007/s11214-008-9336-1.
- Angelopoulos, V., et al. (1994), Statistical characteristics of bursty bulk flow events, *J. Geophys. Res.*, *99*(A11), 21,257–21,280.
- Axford, W. I., and C. O. Hines (1961), A unifying theory of high-latitude geophysical phenomena and geomagnetic storms, *Canadian Journal of Physics*, *39*(10), 1433–1464, doi:10.1139/p61-172.
- Baker, D. N., T. I. Pulkkinen, V. Angelopoulos, W. Baumjohann, and R. L. McPherron

- (1996), Neutral line model of substorms: Past results and present view, *J. Geophys. Res.*, *101*(A6), 12,975–13,010.
- Baker, J. B. H., R. A. Greenwald, J. M. Ruohoniemi, K. Oksavik, J. W. Gjerloev, L. J. Paxton, and M. R. Hairston (2007), Observations of ionospheric convection from the Wallops SuperDARN radar at middle latitudes, *J. Geophys. Res.*, *112*(A1), doi:10.1029/2006JA011982.
- Baker, K. B., and S. Wing (1989), A new magnetic coordinate system for conjugate studies at high latitudes, *J. Geophys. Res.*, *94*(A7), 9139–9143.
- Baumjohann, W., and K.-H. Glassmeier (1984), The transient response mechanism and Pi2 pulsations at substorm onset - review and outlook, *Planet. Space Sci.*, *32*(11), 1361–1370.
- Baumjohann, W., M. Hesse, S. Kokubun, T. Mukai, T. Nagai, and A. A. Petrukovich (1999), Substorm dipolarization and recovery, *Journal of Geophysical Research: Space Physics*, *104*(A11), 24,995–25,000, doi:10.1029/1999JA900282.
- Belian, R. D., D. N. Baker, E. W. Hones, P. R. Higbie, S. J. Bame, and J. R. Asbridge (1981), Timing of energetic proton enhancements relative to magnetospheric substorm activity and its implication for substorm theories, *Journal of Geophysical Research: Space Physics*, *86*(A3), 1415–1421, doi:10.1029/JA086iA03p01415.
- Bilitza, D., L.-A. McKinnell, B. Reinisch, and T. Fuller-Rowell (2011), The international reference ionosphere today and in the future, *85*(12), 909–920, doi:10.1007/s00190-010-0427-x.
- Birn, J., M. Hesse, G. Haerendel, W. Baumjohann, and K. Shiokawa (1999), Flow braking and the substorm current wedge, *J. Geophys. Res.*, *104*(A9), 19,895–19,903, doi:10.1029/1999JA900173.

- Blanchard, G. T., S. Sundeen, and K. B. Baker (2009), Probabilistic identification of high-frequency radar backscatter from the ground and ionosphere based on spectral characteristics, *Radio Sci.*, *44*(5), RS5012, doi:10.1029/2009RS004141.
- Bristow, W. A., and R. A. Greenwald (1996), Multiradar observations of medium-scale acoustic gravity waves using the Super Dual Auroral Radar Network, *J. Geophys. Res.*, *101*(A11), 24,499–24,511, doi:10.1029/96JA01494.
- Bristow, W. A., R. A. Greenwald, and J. C. Samson (1994), Identification of high-latitude acoustic gravity wave sources using the Goose Bay HF radar, *J. Geophys. Res.*, *99*(A1), 319–331, doi:10.1029/93JA01470.
- Bristow, W. A., R. A. Greenwald, and J. P. Villain (1996), On the seasonal dependence of medium-scale atmospheric gravity waves in the upper atmosphere at high latitudes, *J. Geophys. Res.*, *101*(A7), 15,685–15,699, doi:10.1029/96JA01010.
- Brown, L. B., A. J. Gerrard, J. W. Meriwether, and J. J. Makela (2004), All-sky imaging observations of mesospheric fronts in OI 557.7 nm and broadband OH airglow emissions: Analysis of frontal structure, atmospheric background conditions, and potential sourcing mechanisms, *Journal of Geophysical Research: Atmospheres*, *109*(D19), doi:10.1029/2003JD004223.
- Chamberlin, P. C., T. N. Woods, F. G. Eparvier, and A. R. Jones (2009), Next generation X-ray sensor (XRS) for the NOAA GOES-R satellite series, in *Solar Physics and Space Weather Instrumentation III*, vol. 7438, San Diego, CA, doi:10.1117/12.826807.
- Chimonas, G., and C. O. Hines (1970), Atmospheric gravity waves launched by auroral currents, *Planetary and Space Science*, *18*(4), 565–582, doi:10.1016/0032-0633(70)90132-7.
- Chisham, G., et al. (2007), A decade of the Super Dual Auroral Radar Network (SuperDARN):

- scientific achievements, new techniques, and future directions, *Surveys in Geophys.*, pp. 28:33–109, doi:10.1007/s10712-007-9017-8.
- Chisham, G., M. P. Freeman, G. A. Abel, W. A. Bristow, A. Marchaudon, J. M. Ruohoniemi, and G. J. Sofko (2009), Spatial distribution of average vorticity in the high-latitude ionosphere and its variation with interplanetary magnetic field direction and season, *J. Geophys. Res.*, *114*(A9), doi:10.1029/2009JA014263.
- Clausen, L. B. N., T. K. Yeoman, R. Behlke, and E. A. Lucek (2008), Multi-instrument observations of a large scale Pc4 pulsation, *Ann. Geophys.*, *26*(1), 185–199, doi:10.5194/angeo-26-185-2008.
- Coleman, C. J. (1998), A ray tracing formulation and its application to some problems in over-the-horizon radar, *Radio Science*, *33*(4), 1187–1197, doi:10.1029/98RS01523.
- Collins, C., D. H. Jelly, and A. G. Matthews (1961), High-frequency radio-wave black-outs at medium and high latitudes during a solar cycle, *Canadian Journal of Physics*, *39*(1), 35–52, doi:10.1139/p61-004.
- Coster, A., and A. Komjathy (2008), Space weather and the Global Positioning System, *Space Weather*, *6*(6), doi:10.1029/2008SW000400.
- Davies, K. (1990), *Ionospheric Radio*, Peter Peregrinus Ltd., London, England.
- Davis, T. N., and M. Sugiura (1966), Auroral electrojet activity index *AE* and its universal time variations, *J. Geophys. Res.*, *71*(3), 785–801, doi:10.1029/JZ071i003p00785.
- de Larquier, S., J. M. Ruohoniemi, J. B. H. Baker, N. Ravindran Varrier, and M. Lester (2011), First observations of the midlatitude evening anomaly using Super Dual Auroral Radar Network (SuperDARN) radars, *Journal of Geophysical Research: Space Physics*, *116*(A10), doi:10.1029/2011JA016787.

- de Larquier, S., P. Ponomarenko, A. J. Ribeiro, J. M. Ruohoniemi, J. B. H. Baker, K. T. Sterne, and M. Lester (2013), On the spatial distribution of decameter-scale subauroral ionospheric irregularities observed by SuperDARN radars, *Journal of Geophysical Research: Space Physics*, *118*(8), 5244–5254, doi:10.1002/jgra.50475.
- de Wit, R. J., R. E. Hibbins, P. J. Espy, Y. J. Orsolini, V. Limpasuvan, and D. E. Kinnison (2014), Observations of gravity wave forcing of the mesopause region during the January 2013 major Sudden Stratospheric Warming, *Geophysical Research Letters*, *41*(13), 4745–4752, doi:10.1002/2014GL060501.
- Drob, D. P., et al. (2008), An empirical model of the Earth's horizontal wind fields: HWM07, *Journal of Geophysical Research: Space Physics*, *113*(A12), doi:10.1029/2008JA013668.
- Dubyagin, S., N. Ganushkina, M. Kubyshkina, and M. Liemohn (2014), Contribution from different current systems to SYM and ASY midlatitude indices, *Journal of Geophysical Research: Space Physics*, *119*(9), 7243–7263, doi:10.1002/2014JA020122.
- Dungey, J. W. (1961), Interplanetary magnetic field and the auroral zones, *Phys. Rev. Lett.*, *6*, 47–48, doi:10.1103/PhysRevLett.6.47.
- Earle, G. D., A. M. Musumba, and S. L. Vadas (2008), Satellite-based measurements of gravity wave-induced midlatitude plasma density perturbations, *Journal of Geophysical Research: Space Physics*, *113*(A3), n/a–n/a, doi:10.1029/2007JA012766.
- Eccles, V., H. Vo, J. Thompson, S. Gonzalez, and J. J. Sojka (2011), Database of electron density profiles from Arecibo Radar Observatory for the assessment of ionospheric models, *Space Weather*, *9*(1), doi:10.1029/2010SW000591.
- Ern, M., P. Preusse, M. J. Alexander, and C. D. Warner (2004), Absolute values of gravity wave

- momentum flux derived from satellite data, *Journal of Geophysical Research: Atmospheres*, 109(D20), doi:10.1029/2004JD004752.
- European Centre for Medium-Range Weather Forecasts (1990), *ECMWF TOGA 2.5 degree Global Surface and Upper Air Analyses*, <http://rda.ucar.edu/datasets/ds111.2/>, Research Data Archive at the National Center for Atmospheric Research, Computational and Information Systems Laboratory, Boulder, CO. Accessed: 5 June 2015.
- Evans, D. S., and M. S. Greer (2006), *Polar Orbiting Environmental Satellite Space Environment Monitor - 2 - Instrument Descriptions and Archive Data Documentation*, NOAA Space Environment Center, Boulder, Colorado, 2nd ed.
- Evans, J. V., J. M. Holt, and R. H. Wand (1983), A differential-Doppler study of traveling ionospheric disturbances from Millstone Hill, *Radio Science*, 18(3), 435–451, doi:10.1029/RS018i003p00435.
- Francis, S. H. (1974), A theory of medium-scale traveling ionospheric disturbances, *J. Geophys. Res.*, 79(34), 5245–5260, doi:10.1029/JA079i034p05245.
- Frissell, N. A., et al. (2011), First radar observations in the vicinity of the plasmopause of pulsed ionospheric flows generated by bursty bulk flows, *Geophys. Res. Lett.*, 38(1), doi:10.1029/2010GL045857.
- Frissell, N. A., E. S. Miller, S. R. Kaeppler, F. Ceglia, D. Pascoe, N. Sinanis, P. Smith, R. Williams, and A. Shovkoplyas (2014a), Ionospheric sounding using real-time amateur radio reporting networks, *Space Weather*, doi:10.1002/2014SW001132.
- Frissell, N. A., J. Baker, J. M. Ruohoniemi, A. J. Gerrard, E. S. Miller, J. P. Marini, M. L. West, and W. A. Bristow (2014b), Climatology of medium-scale traveling ionospheric

- disturbances observed by the midlatitude Blackstone SuperDARN radar, *Journal of Geophysical Research: Space Physics*, doi:10.1002/2014JA019870.
- Fritts, D. C., and M. J. Alexander (2003), Gravity wave dynamics and effects in the middle atmosphere, *Reviews of Geophysics*, *41*(1), doi:10.1029/2001RG000106.
- Fujita, S., H. Nakata, M. Itonaga, A. Yoshikawa, and T. Mizuta (2002), A numerical simulation of the Pi2 pulsations associated with the substorm current wedge, *J. Geophys. Res.*, *107*(A3), doi:10.1029/2001JA900137.
- Georges, T. M. (1968), Hf doppler studies of traveling ionospheric disturbances, *Journal of Atmospheric and Terrestrial Physics*, *30*(5), 735–746, doi:10.1016/S0021-9169(68)80029-7.
- Gerrard, A. J., T. J. Kane, J. P. Thayer, T. J. Duck, J. A. Whiteway, and J. Fiedler (2002), Synoptic scale study of the arctic polar vortex's influence on the middle atmosphere, 1, observations, *Journal of Geophysical Research: Atmospheres*, *107*(D16), ACL 1–1–ACL 1–15, doi:10.1029/2001JD000681.
- Gerrard, A. J., T. J. Kane, S. D. Eckermann, and J. P. Thayer (2004), Gravity waves and mesospheric clouds in the summer middle atmosphere: A comparison of lidar measurements and ray modeling of gravity waves over Sondrestrom, Greenland, *Journal of Geophysical Research: Atmospheres*, *109*(D10), doi:10.1029/2002JD002783.
- Gerrard, A. J., Y. Bhattacharya, and J. P. Thayer (2011), Observations of in-situ generated gravity waves during a stratospheric temperature enhancement (STE) event, *Atmospheric Chemistry and Physics*, *11*(22), 11,913–11,917, doi:10.5194/acp-11-11913-2011.
- Gjerloev, J. W., R. A. Greenwald, C. L. Waters, K. Takahashi, D. Sibeck, K. Oksavik, R. Barnes, J. Baker, and J. M. Ruohoniemi (2007), Observations of Pi2 pulsations by the

- Wallops HF radar in association with substorm expansion, *Geophys. Res. Lett.*, *34*(L20103), doi:10.1029/2007GL030492.
- Goncharenko, L., J. L. Chau, P. Condor, A. Coster, and L. Benkevitch (2013), Ionospheric effects of sudden stratospheric warming during moderate-to-high solar activity: Case study of January 2013, *Geophysical Research Letters*, *40*(19), 4982–4986, doi:10.1002/grl.50980.
- Greenwald, R., et al. (1995), DARN/SuperDARN: A global view of the dynamics of high-latitude convection, *Space Sci. Rev.*, pp. 71:761–796.
- Greenwald, R. A., K. Oksavik, R. Barnes, J. M. Ruohoniemi, J. Baker, and E. R. Talaat (2008), First radar measurements of ionospheric electric fields at sub-second temporal resolution, *Geophys. Res. Lett.*, *35*(3), doi:10.1029/2007GL032164.
- Grocott, A., K. Hosokawa, T. Ishida, M. Lester, S. E. Milan, M. P. Freeman, N. Sato, and A. S. Yukimatu (2013), Characteristics of medium-scale traveling ionospheric disturbances observed near the Antarctic Peninsula by HF radar, *Journal of Geophysical Research: Space Physics*, doi:10.1002/jgra.50515.
- Hernández-Pajares, M., J. M. Juan, J. Sanz, and A. Aragón-Àngel (2012), Propagation of medium scale traveling ionospheric disturbances at different latitudes and solar cycle conditions, *Radio Science*, *47*(6), doi:10.1029/2011RS004951, rS0K05.
- Hines, C. O. (1960), Internal atmospheric gravity waves at ionospheric heights, *Canadian Journal of Physics*, *38*(11), 1441–1481, doi:10.1139/p60-150.
- Hitchman, M. H., J. C. Gille, C. D. Rodgers, and G. Brasseur (1989), The separated polar winter stratopause: A gravity wave driven climatological feature, *Journal of the Atmospheric Sciences*, *46*(3), 410–422, doi:10.1175/1520-0469(1989)046<0410:TSPWSA>2.0.CO;2.

- Hocke, K., and K. Schlegel (1996), A review of atmospheric gravity waves and traveling ionospheric disturbances: 1982-1995, *Ann. Geophys.*, *14*(9), 917–940, doi:10.1007/s00585-996-0917-6.
- Holzworth, R. H., and C. Meng (1975), Mathematical representation of the auroral oval, *Geophys. Res. Lett.*, *2*(9), 377–380.
- Hooke, W. H. (1970), Ionospheric response to an isotropic spectrum of internal gravity waves, *Planetary and Space Science*, *18*(12), 1793 – 1797, doi:10.1016/0032-0633(70)90012-7.
- Hundhausen, A. J. (1995), *Introduction to Space Physics*, chap. The Sun and Its Magnetohydrodynamics, Cambridge University Press.
- Hunsucker, R. D. (1982), Atmospheric gravity waves generated in the high-latitude ionosphere: A review, *Reviews of Geophysics*, *20*(2), 293–315, doi:10.1029/RG020i002p00293.
- Hunsucker, R. D., and L. H. Tveten (1967), Large traveling-ionospheric-disturbances observed at midlatitudes utilizing the high resolution h.f. backscatter technique, *Journal of Atmospheric and Terrestrial Physics*, *29*(8), 909–916, doi:10.1016/0021-9169(67)90240-1.
- Hunter, J. D. (2007), Matplotlib: A 2d graphics environment, *Computing In Science & Engineering*, *9*(3), 90–95, doi:10.1109/MCSE.2007.55.
- Iijima, T., and T. Nagata (1972), Signatures for substorm development of the growth phase and expansion phase, *Planetary and Space Science*, *20*(7), 1095–1112, doi:10.1016/0032-0633(72)90219-X.
- Ishida, T., K. Hosokawa, T. Shibata, S. Suzuki, N. Nishitani, and T. Ogawa (2008), SuperDARN observations of daytime MSTIDs in the auroral and mid-latitudes: Possibility of long-distance propagation, *Geophysical Research Letters*, *35*(13), doi:10.1029/2008GL034623.

- Iyemori, T. (1990), Storm-time magnetospheric currents inferred from mid-latitude geomagnetic field variations, *Journal of Geomagnetism and Geoelectricity*, *42*(11), 1249–1265, doi:10.5636/jgg.42.1249.
- Jacobs, J. A., Y. Kato, S. Matsushita, and V. A. Troitskaya (1964), Classification of geomagnetic micropulsations, *J. Geophys. Res.*, *69*(1), 180–181.
- Johnson, C. Y. (1969), Ion and neutral composition of the ionosphere, *Annals of the IQSY*, *5*, 197–213.
- Kanzawa, H. (1989), Warm stratopause in the antarctic winter, *Journal of the Atmospheric Sciences*, *46*(3), 435–438, doi:10.1175/1520-0469(1989)046<0435:WSITAW>2.0.CO;2.
- Keiling, A., and K. Takahashi (2011), Review of pi2 models, *Space Science Reviews*, *161*(1), 63–148, doi:10.1007/s11214-011-9818-4.
- Kelley, M. C. (2011), On the origin of mesoscale TIDs at midlatitudes, *Annales Geophysicae*, *29*(2), 361–366, doi:10.5194/angeo-29-361-2011.
- Kepko, L., and M. Kivelson (1999), Generation of Pi2 pulsations by bursty bulk flows, *J. Geophys. Res.*, *104*, 25,021–25,034, doi:10.1029/1999JA900361.
- Kepko, L., M. G. Kivelson, and K. Yumoto (2001), Flow bursts, braking, and Pi2 pulsations, *Journal of Geophysical Research: Space Physics*, *106*(A2), 1903–1915, doi:10.1029/2000JA000158.
- Kepko, L., et al. (2014), Substorm current wedge revisited, *Space Science Reviews*, *190*(1), 1–46, doi:10.1007/s11214-014-0124-9.
- King, J., and N. Papitashvili (2006), *One Minute and Five Minute Solar Wind Data Sets at the Earth's Bow Shock Nose*, NASA Goddard Space Flight Center/Space Physics Data Facility, Greenbelt, Maryland.

- Kivelson, M. G. (1995), *Introduction to Space Physics*, chap. Pulsations and Magnetohydrodynamic Waves, Cambridge University Press.
- Kotake, N., Y. Otsuka, T. Ogawa, T. Tsugawa, and A. Saito (2007), Statistical study of medium-scale traveling ionospheric disturbances observed with the GPS networks in Southern California, *Earth Planets Space*, *59*(2), 95–102.
- Lindzen, R. S. (1981), Turbulence and stress owing to gravity wave and tidal breakdown, *Journal of Geophysical Research: Oceans*, *86*(C10), 9707–9714, doi:10.1029/JC086iC10p09707.
- Liu, J., et al. (2009), THEMIS observation of a substorm event on 04:35, 22 February 2008, *Ann. Geophys.*, *27*, 1831–1841, doi:10.5194/angeo-27-1831-2009.
- Luhmann, J. G. (1995), *Introduction to Space Physics*, chap. Ionospheres, Cambridge University Press.
- Lui, A. T. Y. (1996), Current disruption in the earth’s magnetosphere: Observations and models, *J. Geophys. Res.*, *101*(A6), 13,967–13,088.
- Mallinckrodt, A. J., and C. W. Carlson (1978), Relations between transverse electric fields and field-aligned currents, *Journal of Geophysical Research: Space Physics*, *83*(A4), 1426–1432, doi:10.1029/JA083iA04p01426.
- McFadden, J., C. Carlson, D. Larson, M. Ludlam, R. Abiad, B. Elliott, P. Turin, M. Marckwordt, and V. Angelopoulos (2008), The THEMIS ESA plasma instrument and in-flight calibration, *Space Sci. Rev.*, *141*(1), 277–302.
- McIlwain, C. E. (1961), Coordinates for mapping the distribution of magnetically trapped particles, *Journal of Geophysical Research*, *66*(11), 3681–3691, doi:10.1029/JZ066i011p03681.

- McKinney, W. (2010), Data structures for statistical computing in python, in *Proceedings of the 9th Python in Science Conference*, edited by S. van der Walt and J. Millman, pp. 51 – 56.
- McPherron, R. L., C. T. Russell, and M. P. Aubry (1973), Satellite studies of magnetospheric substorms on August 15, 1968: 9. Phenomenological model for substorms, *Journal of Geophysical Research*, *78*(16), 3131–3149, doi:10.1029/JA078i016p03131.
- Mende, S., S. Harris, H. Frey, V. Angelopoulos, C. T. Russell, E. Donovan, B. Jackel, M. Greffen, and L. Peticolas (2008), The THEMIS array of ground-based observatories for the study of auroral substorms, *Space Sci. Rev.*, *141*(1), 357–387.
- Meriwether, J. W., and A. J. Gerrard (2004), Mesosphere inversion layers and stratosphere temperature enhancements, *Reviews of Geophysics*, *42*(3), doi:10.1029/2003RG000133, rG3003.
- Miller, E. S., H. Kil, J. J. Makela, R. A. Heelis, E. R. Talaat, and A. Gross (2014), Topside signature of medium-scale traveling ionospheric disturbances, *Ann. Geophys.*, *32*(8), 959–965, doi:10.5194/angeo-32-959-2014.
- Millman, K. J., and M. Aivazis (2011), Python for scientists and engineers, *Computing in Science & Engineering*, *13*(2), 9–12, doi:10.1109/MCSE.2011.36.
- Munro, G. H. (1948), Short-period changes in the F region of the ionosphere, *Nature*, *162*(4127), 886–887, doi:10.1038/162886a0.
- Newell, P. T., and C.-I. Meng (1988), The cusp and the cleft/boundary layer: Low-altitude identification and statistical local time variation, *Journal of Geophysical Research: Space Physics*, *93*(A12), 14,549–14,556, doi:10.1029/JA093iA12p14549.

- Nishioka, M., T. Tsugawa, M. Kubota, and M. Ishii (2013), Concentric waves and short-period oscillations observed in the ionosphere after the 2013 Moore EF5 tornado, *Geophysical Research Letters*, *40*(21), 5581–5586, doi:10.1002/2013GL057963.
- Nosé, M. (2010), Excitation mechanism of low-latitude Pi2 pulsations: Cavity mode resonance or BBF-driven process?, *J. Geophys. Res.*, *115*(A7), doi:10.1029/2009JA015205.
- Ogawa, T., K. Igarashi, K. Aikyo, and H. Maeno (1987), NNSS satellite observations of medium-scale traveling ionospheric disturbances at southern high-latitudes, *Journal of Geomagnetism and Geoelectricity*, *39*, 709–721.
- Ogawa, T., N. Nishitani, Y. Otsuka, K. Shiokawa, T. Tsugawa, and K. Hosokawa (2009), Medium-scale traveling ionospheric disturbances observed with the SuperDARN Hokkaido radar, all-sky imager, and GPS network and their relation to concurrent sporadic E irregularities, *Journal of Geophysical Research: Space Physics*, *114*(A3), doi:10.1029/2008JA013893.
- Oinats, A. V., N. Nishitani, P. Ponomarenko, O. I. Berngardt, and K. G. Ratovsky (2016), Statistical characteristics of medium-scale traveling ionospheric disturbances revealed from the Hokkaido East and Ekaterinburg HF radar data, *Earth, Planets and Space*, *68*(1), 1–13, doi:10.1186/s40623-016-0390-8.
- Olson, J. V. (1999), Pi2 pulsations and substorm onsets: A review, *J. Geophys. Res.*, *104*.
- Parks, G. K., and J. R. Winckler (1968), Acceleration of energetic electrons observed at the synchronous altitude during magnetospheric substorms, *Journal of Geophysical Research*, *73*(17), 5786–5791, doi:10.1029/JA073i017p05786.
- Pedatella, N. M., and H. Liu (2013), The influence of atmospheric tide and planetary wave

- variability during sudden stratosphere warmings on the low latitude ionosphere, *Journal of Geophysical Research: Space Physics*, *118*(8), 5333–5347, doi:10.1002/jgra.50492.
- Pekrides, H., A. D. M. Walker, and P. R. Sutcliffe (1997), Global modeling of pi 2 pulsations, *J. Geophys. Res.*, *102*(A7), 14,343–14,354.
- Pérez, F., and B. E. Granger (2007), IPython: a system for interactive scientific computing, *Computing in Science and Engineering*, *9*(3), 21–29, doi:10.1109/MCSE.2007.53.
- Perkins, F. (1973), Spread F and ionospheric currents, *Journal of Geophysical Research*, *78*(1), 218–226, doi:10.1029/JA078i001p00218.
- Picone, J. M., A. E. Hedin, D. P. Drob, and A. C. Aikin (2002), NRLMSISE-00 empirical model of the atmosphere: Statistical comparisons and scientific issues, *Journal of Geophysical Research: Space Physics*, *107*(A12), SIA 15–1–SIA 15–16, doi:10.1029/2002JA009430.
- Priest, E. R. (1995), *Introduction to Space Physics*, chap. The Sun and Its Magnetohydrodynamics, Cambridge University Press.
- Reinisch, B. W., X. Huang, I. A. Galkin, V. Paznukhov, and A. Kozlov (2005), Recent advances in real-time analysis of ionograms and ionospheric drift measurements with digisondes, *Journal of Atmospheric and Solar-Terrestrial Physics*, *67*(12), 1054–1062, doi:10.1016/j.jastp.2005.01.009.
- Ribeiro, A. J., J. M. Ruohoniemi, J. B. H. Baker, L. B. N. Clausen, R. A. Greenwald, and M. Lester (2012), A survey of plasma irregularities as seen by the midlatitude Blackstone SuperDARN radar, *J. Geophys. Res.*, *117*(A2), A02,311, doi:10.1029/2011JA017207.
- Rideout, W., and A. Coster (2006), Automated GPS processing for global total electron content data, *10*(3), 219–228, doi:10.1007/s10291-006-0029-5.

- Saito, T. (1969), Geomagnetic pulsations, *Space Science Reviews*, *10*(3), 319–412.
- Saito, T., T. Sakurai, and Y. Koyama (1976), Mechanism of association between pi2 pulsation and magnetospheric substorm, *Journal of Atmospheric and Terrestrial Physics*, *38*(12), 1265–1277.
- Samson, J. C., R. A. Greenwald, J. M. Ruohoniemi, and K. B. Baker (1989), High-frequency radar observations of atmospheric gravity waves in the high-latitude ionosphere, *Geophys. Res. Lett.*, *16*(8), 875–878, doi:10.1029/GL016i008p00875.
- Samson, J. C., R. A. Greenwald, J. M. Ruohoniemi, A. Frey, and K. B. Baker (1990), Goose Bay radar observations of earth-reflected, atmospheric gravity waves in the high-latitude ionosphere, *J. Geophys. Res.*, *95*(A6), 7693–7709, doi:10.1029/JA095iA06p07693.
- Schmidt, R. O. (1986), Multiple emitter location and signal parameter estimation, *Antennas and Propagation, IEEE Transactions on*, *34*(3), 276–280, doi:10.1109/TAP.1986.1143830.
- Schoeberl, M. R., L. R. Lait, P. A. Newman, and J. E. Rosenfield (1992), The structure of the polar vortex, *Journal of Geophysical Research: Atmospheres*, *97*(D8), 7859–7882, doi:10.1029/91JD02168.
- Schunk, R. W., et al. (2014), Ensemble modeling with data assimilation models: A new strategy for space weather specifications, forecasts, and science, *Space Weather*, *12*(3), 123–126, doi:10.1002/2014SW001050.
- Sergeev, V. A., R. C. Elphic, F. S. Mozer, A. Saint-Marc, and J. A. Sauvaud (1992), A two-satellite study of nightside flux transfer events in the plasma sheet, *Planet. Space Sci.*, *40*(11), 1551 – 1572, doi:10.1016/0032-0633(92)90052-P.
- Sutcliffe, P. R., and K. Yumoto (1989), Dayside Pi2 pulsations at low latitudes, *Geophys. Res. Lett.*, *16*(8), 887–890.

- Takahashi, K., S.-i. Ohtani, W. J. Hughes, and R. R. Anderson (2001), CRRES observation of Pi2 pulsations: Wave mode inside and outside the plasmasphere, *J. Geophys. Res.*, *106*, doi:10.1029/2001JA000017.
- Taylor, J., and B. Walker (2010), WSPRing around the world, *QST*, *94*(11), 30–32.
- Troster, J. G., and R. S. Fabry (1997), The NCDXF/IARU international beacon project, *QST*, *81*(9), 47–48.
- Tsugawa, T., A. Saito, Y. Otsuka, M. Nishioka, T. Maruyama, H. Kato, T. Nagatsuma, and K. T. Murata (2011), Ionospheric disturbances detected by GPS total electron content observation after the 2011 off the Pacific coast of Tohoku Earthquake, *Earth Planets Space*, *63*(7), 875–879.
- Tsyganenko, N. A. (1996), Effects of the solar wind conditions on the global magnetospheric configuration as deduced from data-based field models, *Tech. Rep. Publication ESA SP-389*, European Space Agency.
- Vadas, S. L. (2007), Horizontal and vertical propagation and dissipation of gravity waves in the thermosphere from lower atmospheric and thermospheric sources, *Journal of Geophysical Research: Space Physics*, *112*(A6), doi:10.1029/2006JA011845.
- Vadas, S. L., and G. Crowley (2010), Sources of the traveling ionospheric disturbances observed by the ionospheric TIDDBIT sounder near Wallops Island on 30 October 2007, *Journal of Geophysical Research: Space Physics*, *115*(A7), doi:10.1029/2009JA015053.
- Vadas, S. L., and H.-l. Liu (2009), Generation of large-scale gravity waves and neutral winds in the thermosphere from the dissipation of convectively generated gravity waves, *Journal of Geophysical Research: Space Physics*, *114*(A10), doi:10.1029/2009JA014108.

- Waldock, J. A., and T. B. Jones (1986), HF Doppler observations of medium-scale travelling ionospheric disturbances at mid-latitudes, *Journal of Atmospheric and Terrestrial Physics*, *48*(3), 245–260, doi:10.1016/0021-9169(86)90099-1.
- Waldock, J. A., and T. B. Jones (1987), Source regions of medium scale travelling ionospheric disturbances observed at mid-latitudes, *Journal of Atmospheric and Terrestrial Physics*, *49*(2), 105–114, doi:10.1016/0021-9169(87)90044-4.
- Waters, C. L., F. W. Menk, and B. J. Fraser (1991), The resonance structure of low latitude Pc3 geomagnetic pulsations, *Geophys. Res. Lett.*, *18*(12), 2293–2296.
- Whiteway, J. A., T. J. Duck, D. P. Donovan, J. C. Bird, S. R. Pal, and A. I. Carswell (1997), Measurements of gravity wave activity within and around the Arctic stratospheric vortex, *Geophysical Research Letters*, *24*(11), 1387–1390, doi:10.1029/97GL01322.
- Wu, D. L., and J. W. Waters (1996), Satellite observations of atmospheric variances: A possible indication of gravity waves, *Geophysical Research Letters*, *23*(24), 3631–3634, doi:10.1029/96GL02907.
- Yeh, K. C., and C. H. Liu (1974), Acoustic-gravity waves in the upper atmosphere, *Reviews of Geophysics*, *12*(2), 193–216, doi:10.1029/RG012i002p00193.
- Yumoto, K., and C. P. M. N. Group (2001), Characteristics of Pi2 magnetic pulsations observed at the CPMN stations: A review of the STEP results, *Earth Planets Space*, *53*, 981–992.
- Yumoto, K., K. Takahashi, T. Saito, F. W. Menk, B. J. Fraser, T. A. Potermra, and L. J. Zanetti (1989), Some aspects of the relation between Pi 1-2 magnetic pulsations observed at L = 1.3-2.1 on the ground and substorm-associated magnetic field variations in the

nearearth magnetotail observed by AMPTE CCE, *J. Geophys. Res.*, *94*(A4), 3611–3618, doi:10.1029/JA094iA04p03611.

Zhu, X., and M. G. Kivelson (1989), Global mode ULF pulsations in a magnetosphere with a nonmonotonic Alfvén velocity profile, *J. Geophys. Res.*, *A2*(94), 1479–1485.